



HAL
open science

Modélisation de la croissance de matériaux polycristallins par la méthode du champ de phase.

Jesper Mellenthin

► **To cite this version:**

Jesper Mellenthin. Modélisation de la croissance de matériaux polycristallins par la méthode du champ de phase.. Physique [physics]. Ecole Polytechnique X, 2007. Français. NNT : . pastel-00003136

HAL Id: pastel-00003136

<https://pastel.hal.science/pastel-00003136>

Submitted on 27 Jul 2010

HAL is a multi-disciplinary open access archive for the deposit and dissemination of scientific research documents, whether they are published or not. The documents may come from teaching and research institutions in France or abroad, or from public or private research centers.

L'archive ouverte pluridisciplinaire **HAL**, est destinée au dépôt et à la diffusion de documents scientifiques de niveau recherche, publiés ou non, émanant des établissements d'enseignement et de recherche français ou étrangers, des laboratoires publics ou privés.

Thèse présentée pour obtenir le grade de

DOCTEUR DE L'ÉCOLE POLYTECHNIQUE

Spécialité: *Physique*

par

Jesper MELLENTHIN

Sujet

Phase-Field Modeling of Polycrystalline Solidification

(Modélisation de la solidification de matériaux
polycristallins par la méthode du champ de phase)

Soutenue le 26 septembre 2007 devant le jury composé de:

Alphonse FINEL	Président
László GRÁNÁSY	Rapporteur
Jean-Marc DEBIERRE	Rapporteur
Alain KARMA	Examineur
Lev TRUSKINOVSKY	Examineur
Gabriel FAIVRE	Examineur
Mathis PLAPP	Directeur de thèse

Abstract

The phase-field method has become in recent years the method of choice to model microstructural pattern formation during solidification. For monocrystals, quantitative agreement with experiments and analytical solutions has been obtained. The modeling of polycrystals, which consist of many grains of the same thermodynamic phase, but different orientations of the crystalline lattice, is far less advanced. Two types of models have been proposed: multi-phase-field models use a separate phase field for each grain, and orientation-field models use a small number of fields, but have non-analytical terms in their free energy functional.

This work examines various aspects of phase-field modeling of polycrystals and is divided in three parts. In the first, a new possibility of describing the local orientation is explored, using a tensorial order parameter which represents automatically the local symmetry of the system. This approach is tested by developing a phase-field model for the nematic-isotropic phase transition in liquid crystals. The model is applied to simulate the directional “solidification” of a liquid crystal. The effect of the coupling between nematic orientation and the interface shape is investigated. The simulation results for the stability of a planar interface agree well with a generalized stability analysis, which takes into account a new anchoring condition at the interface: the nematic orientation at the interface is the result of the interplay between bulk deformation and interface anisotropy. The shape and stability of well-developed cells is also influenced by this effect. Numerically, the use of a tensorial order parameter simplifies the treatment of the symmetries in the system significantly, while the equations of motions become considerably more complicated.

In the second part, grain boundaries are investigated on a smaller length scale, using a phase field crystal model, where elastic properties and dislocations appear naturally. With this model, the local order in interfaces is examined and the stability of liquid films between two solid grains is studied below the melting point. This situation can be described by an interaction potential between the two solid-liquid interfaces, which is extracted numerically. The results are compared with a phenomenological model which is found to hold for high-angle grain boundaries, where the dislocations overlap. For low-angle grain boundaries, premelting around dislocation as well as a symmetry breaking (dislocations form pairs) is observed. As a result, the interaction potential becomes nonmonotonous, and consists of a long-range attraction and a short-range repulsion.

In the third part, a new phase-field model is developed using an angle variable to describe the crystalline orientation. Contrary to the already existing models, the free energy is constructed without a term proportional to the modulus of the gradient of the orientation field. Instead, the standard squared gradient is used, but it is coupled to the phase field with a singular coupling function. Various benchmark simulations are carried out to test the model. It is found that it presents several artifacts such as spurious grain rotation and interface motion; however, these effects are extremely small, such that the model yields satisfactory results unless the undercooling is very small. Finally, the observed problems are analyzed and ways of obtaining a better description of the dynamics of the angle field are discussed.

Acknowledgments

It is a pleasure to thank the many people who made this thesis possible.

First of all, I am grateful to my thesis advisor, Professor Mathis Plapp, for his support. With his perfectionist view and his great efforts to explain things clearly and simply, he gave me important guidance. Also, he was always available for my questions and for fruitful discussions on the project.

I feel privileged to have been able to work with Professor Alain Karma, my tutor during my research period at Northeastern University in Boston. It was an inspiring time at his laboratory, not least due to the enthusiasm and highly motivating spirit of him and the team.

A special thanks also goes to the examiners and the jury of my thesis, Alphonse Finel, László Gránásy, Jean-Marc Debierre, Lev Truskinovsky and, last but not least, Gabriel Faivre. I appreciate their time, effort and helpful suggestions.

I am indebted to the *École Polytechnique* and the CNRS for providing me the financial resources for my research and scientific exchange in an international surrounding.

The Laboratoire de Physique de la Matière Condensée (PMC) offered me the ideal environment for my research. My former colleagues from the PMC supported me in my research work. I want to thank all of them, but especially Hervé Henry, for all their help, support, interest and valuable hints. In an atmosphere, where every team member was open for a vital exchange of ideas and know-how, I experienced science at its best: teamwork aimed at advancements.

I want to thank Dr. Stefanie Russ, university tutor and supervisor of my Diploma thesis at the Justus-Liebig University. Her continuous advice and cooperation were very encouraging and nurtured my curiosity for physics.

Especially I am obliged to my friends and colleagues Jan Scholz, Hagen Kaprykowsky and Umut Salman for assisting me with numerical and technical questions and for offering me a different perspective on my work.

My special appreciation goes to my family and friends for their encouragement and understanding.

Finally, I want to thank my fiancée Ulrike Michels, who accompanied my way during these three years, regardless of the distance between our domiciles. With loving generosity, she supported me wherever she could and was of great help in difficult times.

Contents

1	Introduction	1
1.1	Tensor-field description for local orientation	3
1.2	Gaining further insights into grain boundaries	4
1.3	Alternative model for polycrystals	5
2	Physical Background	7
2.1	Introduction to polycrystals	8
2.1.1	Two-dimensional lattices	8
2.1.2	Interfaces and surfaces	10
2.2	Pattern formation in solidification processes	18
2.2.1	Solidification of a pure substance	19
2.2.2	Solidification of alloys	21
2.2.3	Directional solidification	23
2.2.4	Mullins-Sekerka instability	25
2.3	Phase-field model	27
2.3.1	Phase-field model for solid-liquid phase transition	28
2.3.2	Multi-phase-field models	31
2.3.3	Phase-field models with orientation field	34
3	Phase-Field Model for Liquid Crystals	37
3.1	Physics of liquid crystals	39
3.1.1	Order parameter	40
3.1.2	Angle and absolute value representation	42
3.1.3	Liquid crystal free energy	44
3.2	Phase-field model	47
3.2.1	Chemical potential	47
3.2.2	Tensor components	48
3.3	Physical parameters	53
3.3.1	Equilibrium solution and interface thickness	54
3.3.2	Surface energy	54
3.3.3	Capillary length and kinetic coefficient	55
3.4	Sharp interface limit	56
3.4.1	Planar interface	57
3.4.2	Perturbation of the planar interface	58
3.4.3	Laplace equation	60
3.4.4	Dispersion relation	62
3.5	Numerical results	65
3.5.1	Physical lengths and model parameters	65

3.5.2	Dispersion relation	66
3.5.3	Cell structure depending on the orientation	67
3.5.4	Conclusion and outlook	70
4	Grain Boundary Structure in the PFC Model	73
4.1	Phase field crystal model	74
4.1.1	Free energy and equation of motion	75
4.1.2	Phase diagram	76
4.1.3	Grain boundary energy	77
4.2	Implementation	81
4.2.1	Integration of the equation of motion	81
4.2.2	Boundary conditions	84
4.3	Numerical results	85
4.3.1	Order in the grain boundary	86
4.3.2	Grain boundaries	88
4.3.3	Grain boundary wetting	96
4.4	Summary and conclusion	101
5	Phase-Field Model for Polycrystals	103
5.1	Phase-field model	104
5.1.1	Free energy	104
5.1.2	Anisotropy	109
5.1.3	Equations of motion	110
5.1.4	Model parameters	111
5.2	Numerical results	111
5.2.1	Stability of the obtained grain boundaries	112
5.2.2	Rotational mobility	115
5.2.3	Anisotropic solid-liquid interface in 1d	117
5.2.4	Anisotropic solid-solid interface in 1d	120
5.2.5	Importance of the artificial growth	122
5.2.6	Formation of polycrystals	124
5.3	Conclusion and outlook	129
6	Summary, Conclusion and Discussion	131
6.1	Tensor description for orientation field	132
6.2	Grain boundaries on a smaller length scale	133
6.3	New phase-field model for polycrystals	135
6.4	Outlook	136
	Résumé en français (summary in french)	139

Chapter 1

Introduction

A wide variety of materials is heterogeneous on macroscopic length scales and consists of grains with different compositions, crystalline structures and/or orientations. The macroscopic material properties such as elasticity or stress resistance depend strongly on the size and distribution of the individual grains and a lot of research has been conducted to improve the understanding of the microstructural evolution.

A well-developed method to simulate the evolution of complex structures numerically is the phase-field model. In theoretical descriptions of solidification processes, as introduced in section 2.2, interfaces between different phases are often described as sharp lines or surfaces in two or three dimension, respectively. Even when physical interfaces are not discrete but possess a certain interface width, this description is reasonable. Usually, the examined structures are orders of magnitude larger than the interface width, which is of the order of several atomic layers. In the sharp interface formulation, the equations of motion can be developed together with boundary conditions, which have to be fulfilled at the interfaces. In many cases, the interface can move according to some interface conditions — one is dealing with a so-called moving boundary problem. Mathematically, it is in general very difficult to solve the equations of motion with the boundary condition for arbitrary interface shapes. To solve the equations of motion numerically, the interface has to be discretized. Since the interface itself is moving with time, it can happen that two neighboring grid points at the interface start moving apart so that new grid points have to be added to ensure a good resolution. Similarly, at different places, the grid can become unnecessarily fine and grid points have to be removed. This process of redefining the interface grid numerically is very time consuming, especially in three dimensions

This problem can be avoided by using the so-called phase-field model. Instead of tracking the discrete interfaces between different phases explicitly, a diffuse interface is assumed. Generally, a phase-field variable is assigned to each phase in the entire system, indicating whether this specific phase is present at this point or not. For the solidification of a single phase, only one phase-field variable is necessary. The solid phase is given by the region where the phase-field variable is equal to one. Accordingly, the liquid phase is indicated by a phase-field variable of either minus one or zero, depending on the model used. In an interface, the phase-field variable varies continuously from one value to the other over a certain interface width. The interface position can then be obtained by the contour line where the phase-field variable has an intermediate value.

For the time-evolution of this phase-field, an equation of motion has to be developed which reduces to the sharp interface equations when the interface width goes to zero. Unfortunately, the phase-field model becomes very inefficient when the physical interface width is used, since it is orders of magnitude smaller than the systems envisaged in the simulations. Instead, formalisms have been developed to allow the artificial increase of the interface width to numerically more convenient length scales without changing the underlying physics. This allows to address problems of micrometer length scales, even in three dimensions. Further details about phase-field models for solidification of pure substances are given in section 2.3.1.

Considering the success of the phase-field model, it is only natural to extend it to the solidification of polycrystals. In this work, solids are assumed to consist of grains of the same chemical composition and lattice structure, but which possess different crystalline orientations. A possible mechanism of creat-

ing such a solid is by starting from an undercooled melt, where at several points grains with different crystalline orientation nucleate and start to grow. As they approach each other, they start to interact and grain boundaries are formed.

For this problem, two different kinds of phase-field models have been developed so far. In the so-called multi-phase-field model, a different phase-field variable is defined for each grain with a different orientation. An example of this method is presented in section 2.3.2. Multi-phase-field models have been applied very successfully to a wide range of problems. The numerical problems of treating thousands of different grains have been overcome. Even if it is hardly possible to store thousands of fields for large systems, it is found that only a limited amount of phase-field variables have a non-vanishing value at the same space-point. It is therefore sufficient to store only a few fields simultaneously. Similarly, the equations of motion have to be solved only where the specific phase is actually present. But the model still has some shortcomings: It is impossible to describe effects such as grain rotations and it is difficult to simulate the nucleation of grains with random orientation.

Both deficits are related to the fact that the numerical description of the grains is very far from the physical or microscopical point of view. Different grains are not really of different thermodynamic phases but the same phase where only the orientations differ. This orientation can be described more naturally with an orientation field, which defines the misorientation of the lattice with respect to some reference coordinate system.

An alternative approach was introduced by Kobayashi and coworkers and is presented in section 2.3.3. Instead of using an extra phase-field variable for each misorientation, only one phase-field variable is used to indicate whether this space point is solid or liquid. In addition, its value is decreased in the grain boundaries, indicating a lower crystalline order. To introduce the lattice orientation, a second variable is used, which gives the orientation of the crystal with respect to the coordinate system.

In this work, an alternative way of describing the orientation field is proposed and tested. The crystalline orientation can be described very naturally by a tensorial order parameter. Depending on the rank of the tensor, certain rotations leave the tensor unchanged. This avoids the special treatment of the angle differences, where in the model so far all the symmetric configurations have to be considered when calculating the angle gradients.

1.1 Tensor-field description for local orientation

When describing the crystalline orientation in two dimensions with a scalar orientation field as introduced in section 2.3.3, the local symmetries of the system have to be treated manually. In the case of a four-fold symmetry of a simple cubic lattice, the orientations $\theta = \theta \pm \frac{\pi}{2} = \theta \pm \pi = \dots = \theta \pm n\frac{\pi}{2}$ with integer numbers n are equivalent. The orientation difference between a grain of orientation $\theta = 0$ and $\theta = 3\pi/4$ is hence not $3\pi/4$ but only $\pi/4$ — the maximal misorientation possible. This problem becomes even more complex in three dimensions.

Numerically, one can restrict the orientation angles to an interval of $-\pi/N < \theta \leq \pi/N$ for systems with N -fold symmetry. One has then to take into account all the symmetrically identical configurations when calculating angle differences.

Alternatively, the orientation field can be expressed in terms of tensors.

Tensors are generalizations of scalars and vectors. A rank n tensor has n indices which run over the number of dimensions in the space used. A vector can be seen as a rank one tensor, a scalar as a rank zero tensor. In general, one has to distinguish between upper (contravariant) and lower (covariant) indices, but they are equivalent in three-dimensional Euclidean space. Only these so-called Cartesian tensors are used in this work and the indices are written as subscripts to the variable. As sum variables, i, j, k, l are used, which then run over the dimensions of space x, y and z . Usually, for better clarity, the sums are given explicitly, else the Einstein sum convention is used and the sum is carried out over all indices appearing twice or more often.

A tensor of rank n is invariant under a rotation of $\frac{2\pi}{n}$, a property which will be used in this work. Seeing a vector as a rank one tensor, one can easily understand that rotating a vector by 360° results in the same vector again. Similar, a rank two tensor is invariant under a rotation of 180° , a rank four tensor under a rotation of 90° and so on.

For the phase-field simulations of polycrystals, a cubic crystal structure is assumed, corresponding to a rotational invariance of 90° and therefore to a rank four tensor. For reasons of simplicity, the formalism of expressing an orientation in terms of tensors is investigated for liquid crystals in chapter 3. Liquid crystals are invariant under a rotation of 180° and can hence be described by rank two tensors.

Using a tensorial order parameter, a new phase-field model for the nematic-isotropic phase transition in liquid crystals is developed. It contains the coupling of the nematic orientation to the interface and is used to study the stability of a planar interface in a directional solidification setup. The numerical results are compared with a generalized linear stability analysis, containing a new anchoring condition based on an interplay between bulk deformation and interface energy.

1.2 Gaining further insights into grain boundaries

To gain further insights into grain boundaries, a model which was developed by Elder and coworkers is presented in chapter 4. It is capable of dealing with smaller lengths scales than the phase-field method envisaged in this work. This so-called phase field crystal model allows to simulate crystalline growth with a rather similar numerical method as the phase-field model, but leads to a periodic structure which can be associated with a solid and a uniform structure which can be associated with a liquid.

The phase field crystal model incorporates elastic effects implicitly and leads to geometric deformations at a grain boundary. The grain boundary structure can be investigated since dislocations and defects appear naturally. Therefore, this approach is a useful tool to examine possible descriptions of grain boundaries in models on a larger length scale, such as the phase-field model.

In this work, the phase field crystal model is used to perform simulations of grain boundaries of different misorientations. A special interest is focused on a possible measurement of the crystalline order in the grain boundary, which can be associated with a phase-field parameter. Also, the formation of grain bound-

aries is investigated, gaining further insight into the grain boundary properties.

1.3 Alternative model for polycrystalline solidification

With this knowledge about grain boundaries, an alternative to the already existing phase-field models with orientation field is developed in chapter 5. A common problem of these models is the existence of localized grain boundaries. It is not possible to include a potential term in the free energy which depends explicitly on the angle variable, since there are no preferred orientations. One can only include gradients of the angle field. In the existing models so far, a term proportional to the modulus of the angle gradient has to be included in the free energy, which introduces singularities in the equations of motion and is hard to motivate from a physical point of view. In this work, a different free energy is developed, which contains as lowest order gradient term the standard squared gradient, which is, however, coupled with a singular coupling function to the phase field ϕ . The exact form of this coupling function is crucial to the model.

For reasons of simplicity, the model is presented in terms of a scalar orientation field and with the four-fold symmetry of a single cubic lattice. In addition, it has been tested in the tensorial description using 180° symmetries.

The model is tested in great detail, concentrating on the stability of grain boundaries. To show the validity of the model, the equilibrium shape is obtained numerically and compared to the Wulff shape in two dimensions.

During the detailed study of this model with orientation variable, despite a general good performance, some fundamental problems are discovered which are mostly rooted in the nature of the model structure. In the equations of motion, the orientation field variable is treated formally as a nonconserved order parameter. Microscopically, grain boundaries can be seen as a line of dislocations, as shown in chapter 4. In the picture of dislocations, a change of orientation is connected with a change in the dislocation density, which is a conserved quantity. In chapter 6, it is discussed how the idea of dislocations or elastic deformations could lead to a new formulation of the equation of motion for an orientation variable.

Chapter 2

Physical Background

This chapter introduces shortly the physics and the models used in this work. In section 2.1, some basic information about the physics of polycrystals is given, concentrating on grain boundaries and on what is important for this work. In section 2.2, three different solidification processes are explained in the so-called sharp interface description. Finally, an introduction to the phase-field model is presented in section 2.3.

2.1 Introduction to polycrystals

To understand the problem treated in this work, it is useful to start with some basic crystalline properties. Generally, a crystal is characterized by its positional order. The perfect crystal is described by a small group of atoms, which is repeated, forming a simple pattern, endlessly through the entire macroscopic body [1]. This approach makes it possible to address problems of huge numbers of atoms with underlying equations which are generally impossible to solve analytically by concentrating on the principles of symmetries.

Even if real materials are hardly ever made of perfect crystals, the description based on the underlying symmetries is very powerful and still works in structures being very different from perfect lattices. Still, lattice imperfections and defects are very important for most naturally occurring substances and technologically important materials.

In the following, the principles of perfect lattices are introduced, followed by a short description of possible defects and grain boundaries.

2.1.1 Two-dimensional lattices

In this work, two-dimensional systems are investigated and therefore the focus is placed on two-dimensional lattices. In addition, they are easier to picture and to understand. The underlying principles can then be generalized to three dimensions. Three-dimensional lattices are explained in nearly every textbook about solid state physics, see for example the one by Kittel [2].

Bravais lattice

The basic principle of a perfect lattice is the infinite repetition of points. One can then define a translation from one point to another, so that the neighborhood remains the same. A lattice obeying this definition is called Bravais lattice and can, in two dimensions, be described as

$$\vec{R} = n_1 \vec{a}_1 + n_2 \vec{a}_2, \quad (2.1)$$

where n_1 and n_2 are integers and \vec{a}_1 and \vec{a}_2 are linearly independent vectors, called primitive vectors. The primitive vectors are not unique and are usually chosen to be as simple as possible or to have some convincing symmetry properties.

In two dimensions, there are five Bravais lattices, as shown in figure 2.1. The square lattice is symmetric under rotations of 90° and under reflection about the x - and y -axes. If the square lattice is deformed along one axis, one obtains the rectangular lattice, which is invariant under rotations of 180° only. In chapter 4, a hexagonal or triangular lattice is investigated, which is invariant under

a rotation of 120° and under reflections about both axes. Deforming the hexagonal lattice in one direction destroys the rotational symmetry and leads to the centered rectangular lattice. A lattice with only inversion symmetry ($\vec{r} \rightarrow -\vec{r}$) is the oblique lattice, which can be constructed from arbitrary \vec{a}_i without any special symmetry.

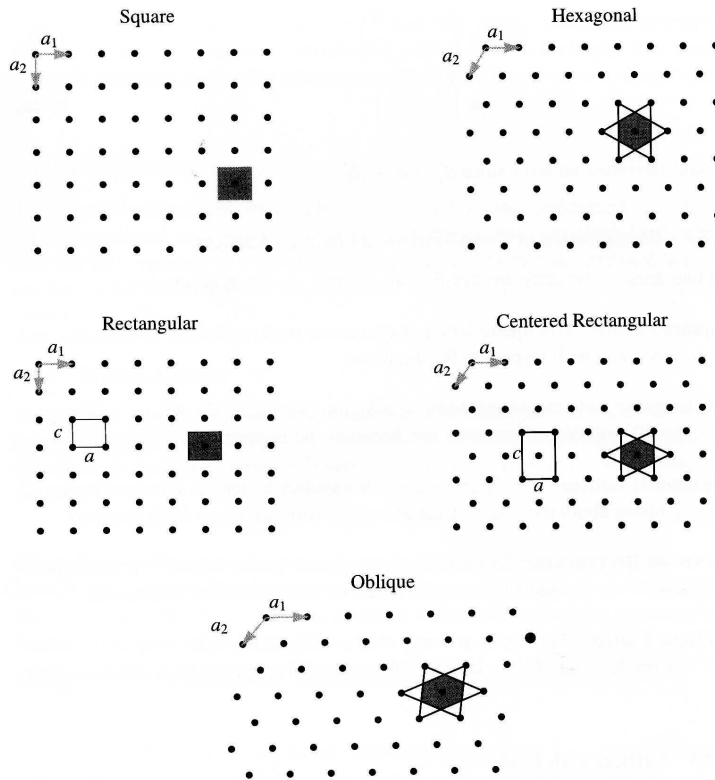


Figure 2.1: The Bravais lattices possible in two dimensions. Also shown possible basis vectors \vec{a}_i and the Wigner-Seitz cell in gray. From [1].

Lattices with bases

Replacing the identical particles at the lattice sites of a Bravais lattice by an identical assembly of particles, a so-called basis, one obtains a more general lattice description, which can be used to describe most lattices in nature. The symmetry properties of such a lattice, however, can be reduced depending on the symmetries of the particular basis. An example of a lattice with a basis is the honeycomb lattice, where at each lattice site of the hexagonal lattice a pair of particles is placed.

Primitive cells and Wigner-Seitz cell

Since the lattices are created by repeating identical units over the entire crystal, already a small region of the system contains the full information of the crystal. The smallest unit containing all the information is called primitive cell and is, similar to the basis vectors, not uniquely defined. All primitive cells, however, are of the same area since they contain exactly one particle for the Bravais lattice or, more generally, the particles of the basis. The volume of the primitive cell is the inverse of the density of the crystal.

Among all the possible choices for the primitive cell, there is one standard way of constructing it, leading to the so-called Wigner-Seitz cell. It contains all the symmetries of the crystal and is constructed by associating to each lattice point all the space which is closer to it than to any other lattice point. The Wigner-Seitz cells of the different two-dimensional lattices are shown in figure 2.1.

Further reading

For further information about three-dimensional lattices, the lattice description in the reciprocal space, experimental methods of obtaining the lattice structure as well as the different atomic binding types it is referred to textbooks about solid state physics, for example the one by Charles Kittel [2]. There, one also learns about lattice vibrations and the thermal properties of crystals, which are not explicitly treated in this work.

2.1.2 Interfaces and surfaces

Comparing the number of atoms located at an interface with the number of bulk atoms, one might be tempted to see surface physics as unimportant. But even if the number of surface atoms relative to those in the bulk is negligible for macroscopic bodies, surfaces play a very important part in many aspects of solid state physics. They build the entrance for all the substances entering or leaving the bulk and often very interesting material properties depend on internal surfaces or thin layers of different components.

The simplest way of obtaining a surface is when the perfect crystalline structure comes to an end, being surrounded by empty space. In this work, the main focus lies in solid-liquid and solid-solid interfaces, where the crystal is surrounded by a liquid or by a second solid with a different crystalline orientation. Close to the interface, the atoms of the crystal hardly ever remain on their originally perfect lattice site. Usually, the crystal is deformed at the grain boundary, leading to an increase or decrease of the volume per atom and therefore to a change of the local density of the material at the interface. It is also possible that the formation of an additional phase in the interface is preferable, for example a solid-solid grain boundary might be covered by a thin liquid film. This effect is called grain boundary wetting or premelting and is investigated in chapter 4 with a phase field crystal model.

In the following, a short description of solid-liquid and solid-solid interfaces are given, with an emphasis on the aspects important for this work.

Solid-liquid interface

So far, it is most generally assumed that the local order breaks down when going from solid to liquid. In a work by Bernal [3], the structure of the liquid phase is investigated in greater details. The basic assumptions are that the liquid is a homogeneous, coherent and essentially irregular assembly of atoms or molecules. This assembly does not contain any holes large enough to fit in another atom or molecule. Therefore, the potential determining the liquid form must be given by the repulsive force between the atoms and can be modeled by a hard-sphere model.

In a model experiment [3], about 1000 ball-bearings are heaped randomly into a container and fixed with black paint. The resulting structure is analyzed for symmetries, the number of neighbors, average distances and much more. It is found that one of the most characteristic differences between a liquid and a solid is the variation of coordination. While a regular close-packed arrangement in a crystalline solid has twelve nearest neighbors, the liquids dense random packing has five to eleven neighbors, with an average of six.

Experimentally, one can use X-ray diffraction to investigate the atomic structure of the liquid [4]. For a solid at 0K, the radial density distribution is strongly peaked at the distance of the nearest neighbors, the next-nearest neighbors and so forth, with a peak height corresponding to the number of respective neighbors. At larger temperature but still below melting, the density function is still of the same form but is smeared out, representing the probability of finding an atom at the corresponding distance. In the liquid, when the temperature is larger than the melting temperature, the atoms are still rather limited in their motion, similar to what can be seen in the model with the ball-bearings. The probability of finding an atom at approximately the neighboring distance is relatively high, the atoms still prefer to surround as many nearest-neighbors as possible to maximize bonding, in average between nine and eleven. The next-nearest neighbors are still grouped around the nearest neighbors, but with increasing distance the order decays, contrary to the situation in the solid. One can summarize that at the melting temperature, the long-range order breaks down even if some local short-range order remains.

When one investigates solid-liquid interfaces, a similar effect can be seen. In figure 2.2, a schematic representation of the density of atom centers is shown as function of the distance to the solid-liquid interface. While the density function is ordered but smeared out in the solid, it decays with decreasing amplitude into the liquid. The order is hence extended into the liquid phase.

More generally, the density wave depends on the lattice structure of the solid. Depending on the direction with respect to the crystalline axes, the density decays with different decay lengths into the liquid. This dependence on the crystalline structure reflects the anisotropy of the system and leads to the anisotropy in macroscopic quantities such as the surface energy, which is presented later in this section.

To describe the crystal respecting its lattice structure, one can use a Ginzburg-Landau theory, where order parameters are introduced which correspond to the amplitudes of the density waves in direction of the principal reciprocal lattice vectors [5,6]. In a good approximation, especially for metallic systems, these amplitudes can be assumed to be proportional to each other, so that it is sufficient to use a single order parameter. Due to this approximation, however, one

loses all the information about the anisotropy of the system. The picture of having one decaying amplitude motivates the idea of having a diffuse interfaces in the phase-field model, which is presented in section 2.3. The dashed envelope shown in figure 2.2 is a possible physical interpretation of the phase field.

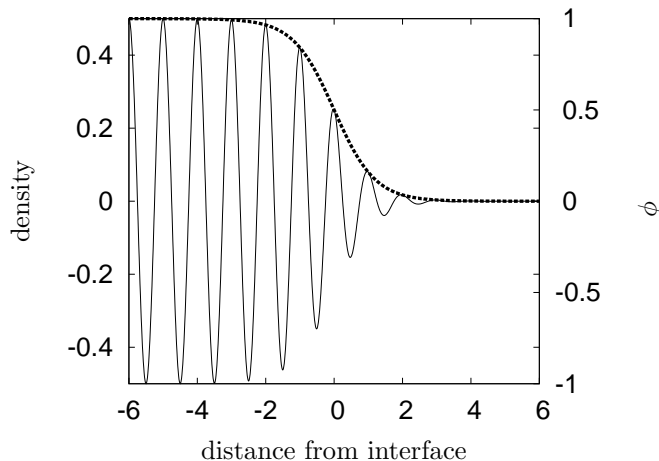


Figure 2.2: Schematic representation of the density of atom centers as function of the distance to the solid-liquid interface. The periodic structure decays over a length of a few atomic layers into the liquid. As envelope, a possible physical interpretation of the phase field ϕ is shown with a heavy dashed line, varying from one to zero.

Solid-liquid interface energy

Associated with the solid-liquid interface is an energy. Experimentally, the solid-liquid interface energy can be determined as shown by Turnbull and Cech [7, 8]. In their experiment, small liquid metal droplets and their solidification is observed. In small volumes (e.g. a few tens of micrometers in diameter), the impurity concentration can be assumed to be constant and since solidification usually starts at impurities, a homogeneous solidification can be expected. Measuring the maximal undercooling and using homogeneous nucleation theory, rather accurate estimates of the solid-liquid interface energy can be obtained. Relating the solid-liquid interface energy with the enthalpy of melting H_m , it is found that $\gamma_{SL} \simeq (0.32 - 0.45)\Delta H_m$, where the value of 0.32 is found for semi-metallic elements and 0.45 for metals [4].

More generally, the empiric relation by Turnbull [8], which relates the surface tension with the latent heat L and the number density of the solid phase ρ , is given by

$$\gamma = C_T L \rho^{2/3}.$$

The so-called Turnbull coefficient C_T is found to be approximately 0.45 for metals and 0.32 for many nonmetals. More recently, larger undercoolings have been achieved, the largest ones by Perepezko [9], and Turnbull coefficients of up to 0.6 have been found for some FCC and HCP structures. The Turnbull relation

has been confirmed by many experiments and simulations. For a summary and a review of proposed modifications, it is referred to Jones [10] or Granasy and Tegze [11]. Nowadays, the main interest is focused on the anisotropy in the surface tension, as described in the next subsection.

Anisotropy in the liquid-solid surface energy

In general, the surface energy depends on the direction of the surface with respect to the crystal lattice. The interface shape itself depends therefore on the anisotropy. The so-called Wulff construction [12] can be applied to construct the equilibrium shape knowing the surface anisotropy.

To do so, the surface tension is plotted in the following way. The magnitude of the surface energy $\gamma(\vec{n})$ is plotted as length of a vector \vec{r} , whose directions corresponds to the surface normal \vec{n} . The vector \vec{r} is then given as $\vec{r} = \gamma(\vec{n})\vec{n}$. An example is shown in figure 2.3, showing the directions of minimal surface energy very clearly. Based on this so-called Wulff plot [4], the equilibrium shape can be constructed by the following steps. Firstly, a radius vector is drawn from the origin to intersect the Wulff plot. In two dimensions, a line normal to the radius vector is drawn passing through the point of intersection. Repeating this procedure for each point of the Wulff plot forms a figure, given by inner envelope of all the normals, corresponding to the equilibrium shape.

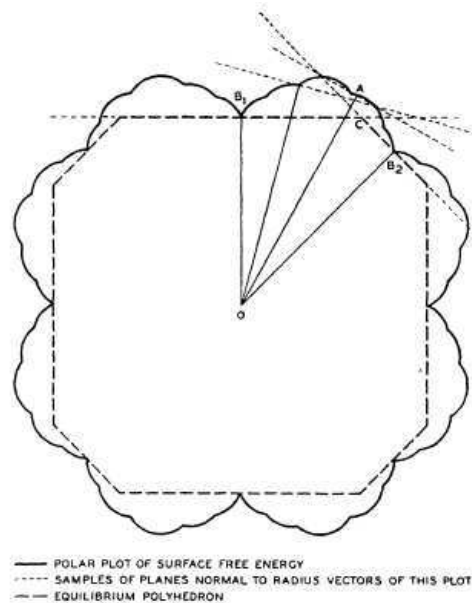


Figure 2.3: Wulff plot of a surface energy with corresponding Wulff construction to obtain the equilibrium shape. From [12].

Even if it is usually not possible to construct a unique surface anisotropy from the equilibrium shape, this method can be used to obtain information about the surface anisotropy from measurements or simulations of the interface shape. For recent experiments determining interface anisotropies of metal alloys

see for example the work by Napolitano and coworkers [13–15]. In figure 2.4, a snapshot of a molecular dynamics simulation is shown, where silicon is in equilibrium with its undercooled melt. In figure 2.5, a series of TEM images showing the shape of a lead particle is presented at different temperatures. In both cases, one can use the obtained shape to draw conclusions about the anisotropy of the surface energy. Without going into details, one can see that the symmetry of the crystalline lattice is represented in the surface shape and therefore in the anisotropy. This basic observation motivates the assumptions of the anisotropy used in the numerical simulations in this work.

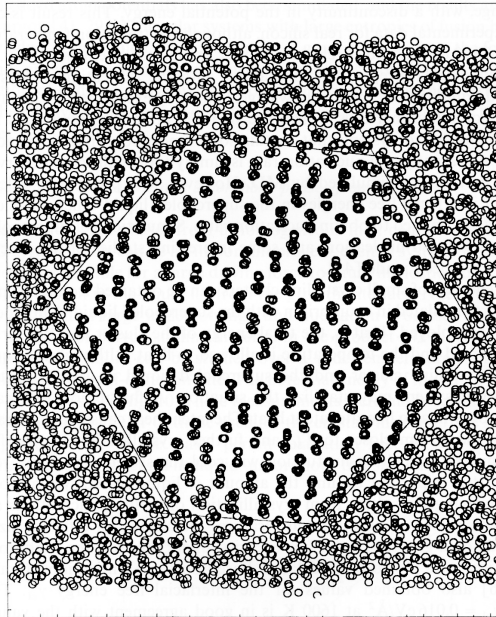


Figure 2.4: Molecular dynamics simulation of a d.c. silicon cluster in equilibrium with its undercooled melt. From the equilibrium shape, the surface energy and its anisotropy can be obtained. From [16].

Recently, molecular dynamics simulations have proven to be a very powerful tool to obtain surface energies and their anisotropies. Especially for metal alloys, the anisotropies are typically very weak (on the order of 1%), which makes them difficult to obtain. For a summary on how to obtain the anisotropies in atomistic simulations and how to include them in continuum simulations such as the phase-field model is referred to an article by Hoyt et al. [18].

Since the anisotropy seems to depend mainly on the crystalline structure rather than on the intermolecular forces, it is also possible to use continuum density wave descriptions to obtain the angle dependence of a solid-liquid interface [5, 6].

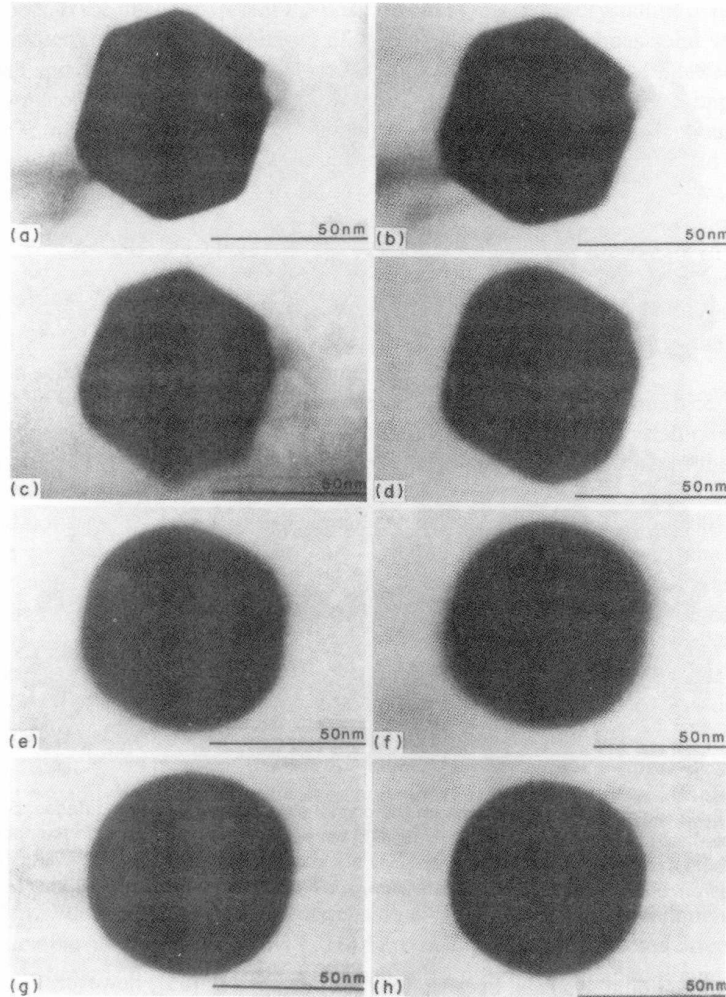


Figure 2.5: TEM images of a lead particle in a melt-spun aluminum-5 wt.% lead alloy for different temperatures: (a) room temperature, (b) 100° C, (c) 300° C, (d) 350° C, (e) 400° C, (f) 450° C, (g) 500° C, (h) 550° C. One can see how the shape changes. From the shape, the anisotropy in the solid-liquid interface energy can be obtained. From [17].

Solid-solid interface

Solid-solid interfaces are more complex than solid-liquid interfaces, since on both sides long-range atomic order exists. Still, the fundamental principles governing the interface shape remain basically the same and even the concept of obtaining the equilibrium shape by the Wulff construction remains valid. The understanding of the physical behavior of these interfaces is therefore quite intuitive. The interface seeks to minimize its energy, which can often be done by maximizing the atomic matching and therefore minimizing the broken bonds. Unfortunately, it is often challenging to describe the interfaces qualitatively and accurately. The solid-solid interface is accompanied by different types of defects, which possess an elastic strain field. Also the composition and the order can change dramatically at the interface [4].

There are two different main types of solid-solid interfaces. Those interfaces, where both solids are of the same phase and where the interface is caused solely by a difference in the orientation and/or a translation of the lattices are called homophase interfaces. If the composition and/or the Bravais lattice differs as well in the two separated crystals, the interface is called heterophase interface. Heterophase interfaces are further divided into three subclasses: Fully coherent interfaces, semi-coherent interfaces and incoherent interfaces. In fully coherent interfaces, the atomic planes and lines continue uninterrupted through the interface. In semi-coherent interfaces, the crystalline structure is interrupted by a periodic array of misfit dislocations in the interface. In incoherent interfaces, there is no correspondence between the atomic planes and lines in the two crystals.

To study solid-solid interfaces in crystalline materials, the concept of dislocations can be used. In a three-dimensional medium, a dislocation is a line with a tangent vector \vec{t} , which is defined by its Burgers vector \vec{b} and which is orientated. There are two particular cases of dislocations which can be obtained from a thought experiment called the “Volterra process”, compare figure 2.6. In this thought experiment, the bonds between the atoms are cut along an arbitrary plane, ending on a dislocation line, see figure 2.6 a). The two sides of the cut are given a rigid displacement \vec{b} and the created gap is filled with undeformed material. In a crystal, \vec{b} has to correspond to a period of the crystalline lattice. In figure 2.6 b), the crystal is deformed parallel to the interface and the faces are displaced. This deformation can be described by so-called screw dislocations but is not of interest to this work. In the case of the interfaces treated here, the lattices are deformed perpendicular to the interface, see figure 2.6 c), leading to so-called edge dislocations.

In figure 2.7 b), a simple example for the geometry of a grain boundary as treated in this work is shown in two dimensions. To account for the imposed deformation, crystalline planes end at the edge dislocations, which are indicated with the symbols \perp . In general, the bonds between the atoms can be cut along planes in arbitrary directions. To account for this kind of arbitrary deformation, planes in x - and y -direction have to end at x - and y -dislocations, indicated by \vdash s and \perp s, respectively. Similarly, there are negative dislocations which point in the opposite direction.

In general, the concept of dislocations is much more complex and dislocations can be partly of edge- and partly of screw-dislocation character at the same time.

In this work, attention is restricted to one of the simpler kinds of solid-

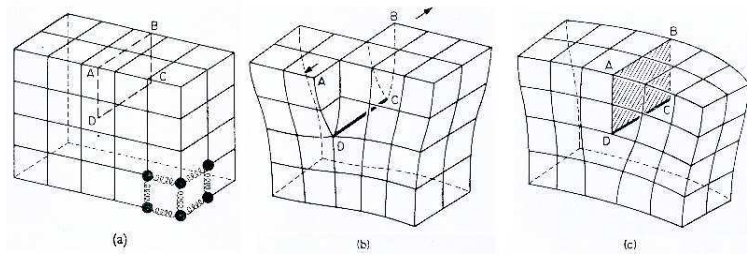


Figure 2.6: Example for possible plastic deformations of a simple cubic crystal. In a), the atomic bonds are cut along the plane ABCD. In b), the faces are displaced creating a so-called screw dislocation. In c), an extra half-plane is inserted, creating an edge dislocation. From [19].

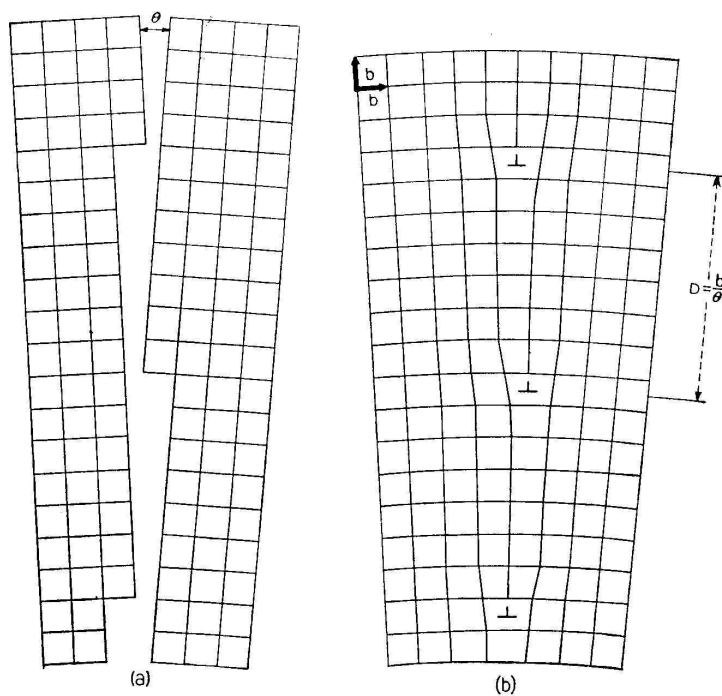


Figure 2.7: The symmetric-tilt grain boundary in a single cubic crystal is obtained by rotating two grains by an angle θ (a) and joining them again (b). Crystalline lines end at dislocations, whose distance D is inversely proportional to the misorientation θ . From [20].

solid grain boundaries. The so-called symmetric-tilt grain boundary belongs to the group of homophase interfaces. It can be described by edge dislocations as shown in figure 2.7, with the simplification that both grains on either side of the interface are tilted with respect to the interface by the same angle but in opposite direction. The description of a grain boundary as an array of dislocations has been proven to be valid for small misorientations but becomes difficult as the dislocations get closer and overlap.

Based on this picture of a line of dislocations, the energy for a low-angle grain boundary can be calculated, as shown by Read and Shockley [21]. In their derivation, the alignment of the interface is generalized, using both types of dislocations as introduced above. To obtain the grain boundary energy, firstly, the shear stress due to the line of dislocations is calculated, where the shear stress of one dislocation is taken as $\tau = x(x^2 - y^2)/(x^2 + y^2)^2$. The stress is given units of $G/[2\pi(1 - \sigma)]$ with rigidity modulus G and Poisson's ratio σ . The lengths x and y are given in units of the lattice constant a . For the case of having only y -dislocations, the shear stress can be written as $\tau = \text{Re} \left\{ \frac{\pi^2}{D^2} x \sin [\pi(y - ix)/D]^{-2} \right\}$, where the distance between the dislocations $D \approx a/\theta$.

Based on the stress field, the self- and interaction energies between the dislocations are calculated by integrating over the entire system, obtaining the the work done on the surface of discontinuity or slip plane. Again, for the case of having solely y -dislocations, there is only one self energy which be written as $-(1/2) [\ln(2\pi r_0/D) - 1]$, where r_0 is the radius of a small circle around the dislocation. The meaning of r_0 can be explained as follows. Since close to the dislocation Hooke's law breaks down, the dislocation energy really consists of two terms: a core energy E_{core} which has to be calculated on an atomistic basis plus the self energy $E_{\text{self}}(r_c)$ as given above, but starting from the core radius r_c (instead of r_0) from which on Hooke's law is valid. With the knowledge of the core energy, one can define the radius r_0 such that the self energy calculated with r_0 corresponds to the real energy, $E_{\text{self}}(r_0) = E_{\text{self}}(r_c) + E_{\text{core}}$. The radius r_0 then does not correspond exactly to the core radius, but is rather a mathematical construct which allows to define the dislocation energy without having the core energy explicitly in the equation.

The energy of the dislocations is then the work done on the slip plane divided by the distance of the slip planes, which is $D = a/\theta$ for the cases treated here. The grain boundary energy can then be written as

$$\gamma_{\text{GB}} = \frac{Ga}{4\pi(1 - \sigma)} \theta [A_0 - \ln \theta], \quad (2.2)$$

where $A_0 = 1 + \ln[a/(2\pi r_0)]$.

2.2 Pattern formation in solidification processes

The spontaneous formation of pattern in the nature has always been of great interest to science. A wide range of beautiful pattern emerge during the growth of crystals, where snowflakes are probably the most well-known example. Of course, pattern formation during solidification is not only of interest from the aesthetic point of view — the microstructure of materials is very important for

their macroscopic properties, motivating the scientific and technical interest in this subject [22]. It turns out that solidifying systems are conceptually simple examples of self-organizing systems. This makes it interesting to study them to understand the underlying mechanism, which then might allow to give insights in more complicated biological systems as well.

In this work, the solidification of different systems is investigated numerically. For all systems, the solidification is controlled purely by a single diffusion process. Other effects, such as convection, are assumed to be small and are ignored. Even if convection plays an important role in generic solidification processes, it is possible to create experiments where convective effects are negligible. This might be in thin samples or in microgravity.

It is also assumed that the molecular binding at the surface is sufficiently weak, therefore growth is rather fast and the interface is rough on molecular scale. On the macroscopic scale, the interface is, however, smoothly rounded. This is the case for most metals and alloys and also for some organic crystals.

The two main mechanism leading to the emergence of complex patterns are the capillary forces, which tend to minimize the surface area, contrary to the diffusion kinetics, where a large surface allows for faster dissipation. The morphological instability leading to the pattern formation process is the interplay between these two effects. The big, mainly unsolved part of the problem is how these complex shapes are selected by nature.

In this section, firstly the solidification of a pure system is explained. Here, the solidification is limited by the diffusion of heat in the system. Secondly, a liquid mixture is examined, where the solidification is mainly controlled by the chemical diffusion since the thermal diffusion occurs on much shorter time scales. The system can hence be seen as being in thermal equilibrium. In the third subsection, a common experimental setup is investigated. In the so-called directional solidification, an external temperature gradient is imposed, which allows to control the growth speed of the system.

2.2.1 Solidification of a pure substance

In this subsection, the solidification of a pure substance from its melt is examined. It is one of the simplest cases where spontaneous pattern formation can be observed. The reversed process, the melting, can be equally interesting and can be described analogously. The following description focuses for simplicity on the solidification process.

If convection in the liquid is neglected, the solidification of a pure substance is purely governed by the diffusion of heat. As the substance solidifies, latent heat is released and has to be conducted into the bulk or absorbed by the boundaries. Therefore, the rate of solidification is controlled by the heat flow in the system.

Whether the morphology of the interface is stable or unstable depends on the configuration. As an example, two setups are shown schematically in figure 2.8. In both cases, the boundary is held at some temperature T_W smaller than the melting temperature T_M . In (a), the solid starts to grow from the boundary into its liquid, which is at a temperature $T > T_M$. The solid is at a temperature below T_M , latent heat is released at the interface and transported through the bulk solid towards the boundary. During the solidification, the front S moves uniformly and smoothly towards the center with a speed which depends on

the flow of heat through the solid. The solidification is totally stable. In (b), the liquid is undercooled at $T < T_M$ and the solidification starts at a seed in the center of the system. The heat has now to be transported through the undercooled liquid towards the boundary. In this setup, the solidification is intrinsically unstable and the interface develops dendrites.

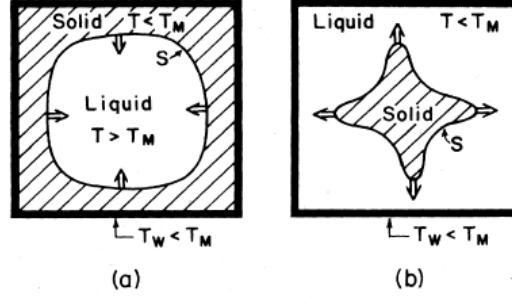


Figure 2.8: Different possibilities of solidification of a system with a boundary at a fixed temperature $T_W < T_M$, where T_M is the melting temperature. In (a), the solidification starts from the boundary and grows into the liquid at $T > T_M$ and is stable. In (b), the solidification starts at a seed in the center and the solid grows into the undercooled liquid. This case is intrinsically unstable. From [23].

The solidification is controlled by the diffusion of the temperature T , which can be written as

$$D'_T \nabla^2 T = \frac{\partial T}{\partial t} \quad (\text{solid}) \quad (2.3)$$

$$D_T \nabla^2 T = \frac{\partial T}{\partial t} \quad (\text{liquid}) \quad (2.4)$$

where different thermal diffusion constants in the solid (D'_T) and liquid phase (D_T) are used. Therefore, Eq. (2.3) is valid in the solid, while Eq. (2.4) is valid in the liquid phase.

At the interface, the total heat is conserved, so that the condition for a moving interface is given as [23]

$$Lv_n = \left[D'_T c'_p (\vec{\nabla} T)_{\text{solid}} - D_T c_p (\vec{\nabla} T)_{\text{liquid}} \right] \cdot \vec{n}, \quad (2.5)$$

where L is the latent heat. c'_p and c_p are the specific heats per unit volume in the solid and liquid phase, respectively. The normal interface velocity is given by v_n , \vec{n} is the interface normal pointing towards the liquid, and the gradients are taken at the indicated sides of the interface. The equation states that the rate at which the heat is created at the moving interface has to be equal to the rate at which it flows into the solid or the liquid. Differences in the densities of the solid and the liquid phase are neglected.

Still missing is a thermodynamic boundary condition at the interface. The simplest choice, corresponding to the Stefan problem as usually posed by the mathematicians, is to postulate that the temperature at the interface has to

be the melting temperature. This neglects, however, the physical effect of the surface energy γ_0 [23], which is the necessary stabilizing force for the pattern formation process. Including the surface energy, the interface condition can be written as

$$T(\text{interface}) = T_M \left[1 - \frac{\gamma_0 \kappa}{L} \right]. \quad (2.6)$$

This is a form of the Gibbs-Thomson relation, which predicts among many other things a reduction of the melting temperature for systems with a large curvature κ . The ratio surface energy over latent heat γ_0/L has the dimension of length, introducing the dimensional information needed to set the scale of the pattern.

In general, the surface energy is anisotropic and can be written as

$$\gamma(\Theta) = \gamma_0 a(\Theta). \quad (2.7)$$

Here, γ_0 is the mean value of the surface energy and the function $a(\Theta)$ defines its dependence on the interface normal \vec{n} , which can be expressed in terms of the angle Θ in two dimensions. With anisotropy in the surface energy, the interface conditions is given as

$$T(\text{interface}) = T_M \left[1 - \frac{\gamma + \gamma''}{L} \kappa \right], \quad (2.8)$$

and is called Gibbs-Thomson-Herring condition.

Still missing in this model is a term taking care of the interface kinetics. Since the interface is moving, it might be necessary to drive liquid molecules onto the surface [23]. This effect will be included in the phase-field model introduced in section 2.3 and usually also exhibits an anisotropy.

2.2.2 Solidification of alloys

Most metallurgical materials are not pure substances but alloys. In alloys, the diffusion of the chemical components controls the solidification. The thermal diffusion is much faster than the chemical diffusion, so that the system can be assumed to be at thermal equilibrium. The interface instabilities leading to the pattern formation are hence caused by the chemical diffusion. However, both situations can be described quite similarly.

A schematic phase diagram of a two component alloy is shown in figure 2.9. The solidification depends on the concentration of the solute c and on the local temperature T_0 , which is assumed to be constant over a large region of the system. The equilibrium concentrations in the solid and in the liquid are different, given by c'_{Eq} and c_{Eq} , respectively. The equilibrium concentration in the liquid is larger than the one in the solid, so that an advancing solidification front rejects solute molecules, similar to the way latent heat is rejected in the solidification of a pure substance. The transport of the excess solute now controls the solidification and governs the growth rate.

The analogy between the two cases can be best shown when expressing the equations of motion in terms of the chemical potential instead of the concentration. Assuming that the partial molar volumes are identically for all species, one can define μ as the chemical potential of the solute relative to the solvent and $\tilde{\mu} = \mu - \mu_{\text{Eq}}(T_0)$ as the difference between μ and its equilibrium value for the coexistence at the temperature T_0 .

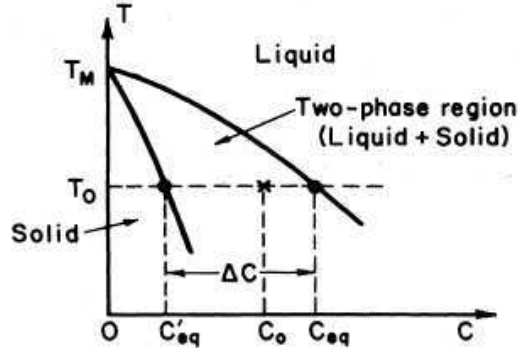


Figure 2.9: Schematic phase diagram of a two-phase solution. From [23].

If the system is close to equilibrium, the relative chemical potentials can be written as [23]

$$\begin{aligned}\tilde{\mu}(\text{solid}) &= \left. \left(\frac{\partial \mu}{\partial c} \right)' \right|_{c=c'_{\text{Eq}}} \delta c' \\ \tilde{\mu}(\text{liquid}) &= \left. \left(\frac{\partial \mu}{\partial c} \right) \right|_{c=c_{\text{Eq}}} \delta c\end{aligned}$$

in the solid and the liquid phase. The local concentration differences are given by $\delta c'$ and δc . With chemical diffusivity D'_c and D_c in the solid and the liquid phase respectively, the diffusion equation is given as

$$\begin{aligned}D'_c \nabla^2 \tilde{\mu} &= \frac{\partial \tilde{\mu}}{\partial t} && \text{(solid)} \\ D_c \nabla^2 \tilde{\mu} &= \frac{\partial \tilde{\mu}}{\partial t} && \text{(liquid)}.\end{aligned}$$

Writing the diffusivity as [23] $D_c = M(\partial \mu / \partial c)$ for the liquid (and accordingly primed for the solid), one obtains an equation similar to the heat conservation equation for the pure case

$$v_n \Delta c = [M'(\nabla \tilde{\mu})_{\text{solid}} - M(\nabla \tilde{\mu})_{\text{liquid}}] \cdot \vec{n}, \quad (2.9)$$

where the concentration jump Δc is shown in the phase diagram and curvature effects are neglected since they turn out to be small under ordinary circumstances. Here M and M' are the mobilities in the liquid and the solid phase, respectively.

The local equilibrium condition at the interface is simply that $\tilde{\mu}$ has to be continuous, having the value

$$\tilde{\mu}(\text{interface}) = -\frac{\gamma + \gamma''}{\Delta c} \kappa, \quad (2.10)$$

with surface energy γ and curvature κ as in the pure case.

If one now looks at the setup from figure 2.8 (a), which resembles the quenching of an ingot of molten metal, one finds that it becomes unstable for an alloy. A system, initially entirely liquid at a temperature T_0 , has to be of a concentration c_0 , which is smaller than c_{Eq} to allow solidification. The liquid is hence effectively or constitutionally supercooled [23] and solidification starts from the walls. The solidification front is unstable, solute-poor dendrites of concentration $c \simeq c'_{\text{Eq}}$ are created, rejecting solute into the liquid in the center. To continue with the solidification, the temperature T_0 has to be reduced, increasing $c'_{\text{Eq}}(T_0)$.

Evidence of the created dendrites remains in the solute-segregation pattern, influencing the macroscopic properties of the quenched alloy. Since the dendrites start from different seeds, the alloy finally consists of grains with different orientations, which are the center of interest of this work, even when the models used are based on pure substances for simplicity.

2.2.3 Directional solidification

Another setup, which is also important from the application point of view, is the directional solidification or zone refinement of multicomponent materials [23]. A schematic picture of the setup is shown in figure 2.10. The sample is placed into a temperature gradient G , created by a hot and a cold contact. The hot contact is at a temperature above the melting temperature, while the cold contact is at a temperature below it. Therefore, the solid-liquid interface is forced to be between the two contacts. By pulling the sample through the setup with a given speed v , the interface has to adjust its growth velocity accordingly. Therefore, the growth speed can be controlled externally, allowing to investigate a wide range of instabilities.

The dominant diffusion process is again the chemical diffusion, but the temperature now varies according to the applied temperature gradient. For the case that the thermal diffusion is much faster than the chemical diffusion and if the latent heat is sufficiently small, one can neglect the heat created during the solidification. If the thermal conductivities are assumed to be similar in both phases, the temperature can be written as a linear variation in dependence of the position x , so that $T = T_0 + Gx$, where G is directed along x .

This linear dependency between temperature and x -axis allows to associate the temperature axis in the phase diagram directly with the x -axis. The composition profile $c(x)$ for a steady-state motion with a given v and G can then be drawn into the phase diagram, as shown in figure 2.11 with the heavily dashed line. The line shows the composition profile for a flat interface with temperature T_0 , where the interface position is given by $x = 0$. To obtain a steady-state solution, all the solute from the liquid has to be absorbed by the solid, so that the concentration far in the solid has to be the same as far in the liquid, shown by the vertical dashed line at $c = c_0$. The value of c_0 determines the interface position, T_0 and therefore $x = 0$ is at the intercept between the solidus and this line, as shown in the phase diagram. This definition of T_0 as reference temperature can be generalized and used for unstable interfaces, too. In front of the interface, a solute excess builds up, leading to a concentration gradient, which must be large enough to drive the solute into the liquid at the externally given pulling velocity v . As one increases the velocity, the gradient increases and the concentration profile enters the two-phase region, experiencing constitutional

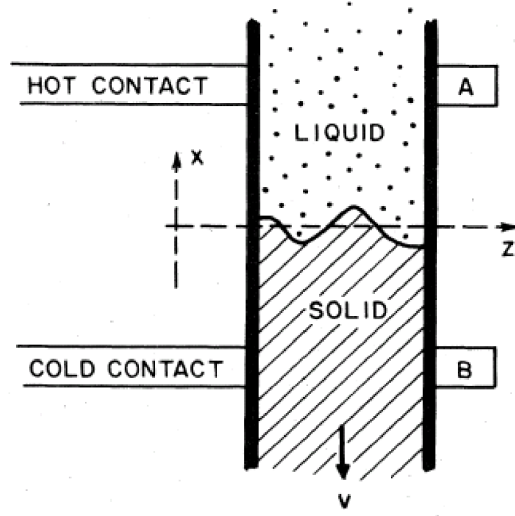


Figure 2.10: Schematic setup of the directional solidification. The sample is pulled through a hot and a cold oven, building up a temperature gradient G . The melting temperature is in between the two contacts, so that the interface speed has to adjust to the pulling velocity v . By varying v/G , the stability of different interface modes can be investigated. From [23].

supercooling and possible instabilities. The same effect is obtained when decreasing the temperature gradient G : the stability depends on the ratio v/G .

The equations of motion for the directional solidification for the two-phase model can be obtained by extending the isothermal model. From the relative chemical potential, one has to subtract the variations of μ coming from the temperature gradient, so that

$$\tilde{\mu}(\text{solid}) \simeq \left. \left(\frac{\partial \mu}{\partial c} \right)' \right|_{c=c'_{\text{Eq}}} \delta c' - \left. \left(\frac{\partial \mu}{\partial T} \right)' \right|_{T=T_0} Gx \quad (2.11)$$

$$\tilde{\mu}(\text{liquid}) \simeq \left. \left(\frac{\partial \mu}{\partial c} \right) \right|_{c=c_{\text{Eq}}} \delta c - \left. \left(\frac{\partial \mu}{\partial T} \right) \right|_{T=T_0} Gx. \quad (2.12)$$

The diffusion equations in the solid and in the liquid are given in the moving frame of reference as

$$D'_c \nabla^2 \tilde{\mu} + v \frac{\partial \tilde{\mu}}{\partial x} = \frac{\partial \tilde{\mu}}{\partial t} \quad (\text{solid})$$

$$D_c \nabla^2 \tilde{\mu} + v \frac{\partial \tilde{\mu}}{\partial x} = \frac{\partial \tilde{\mu}}{\partial t} \quad (\text{liquid}),$$

where the coordinate system moves with the velocity v in x -direction, following the material.

The interface condition can be generalized by allowing an z and a y dependence as $x(\text{interface}) = \xi(y, z, t)$ and one obtains

$$\left(v_n + \frac{\partial \xi}{\partial t} \right) (\vec{n} \cdot \vec{e}_x) \Delta c = [M'(\nabla \tilde{\mu})_{\text{solid}} - M(\nabla \tilde{\mu})_{\text{liquid}}] \cdot \vec{n}, \quad (2.13)$$

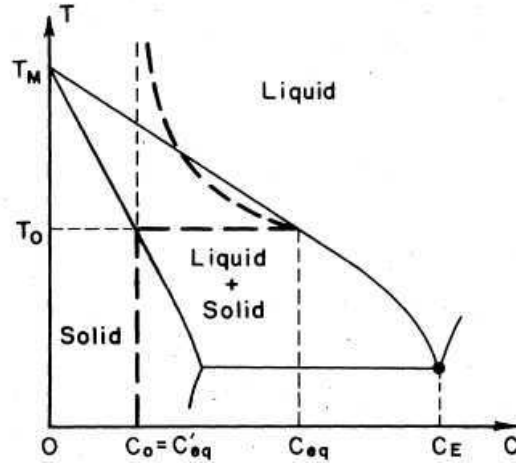


Figure 2.11: Schematic phase diagram of a two-phase solution. The composition profile for a flat interface is shown with the heavy dashed line for directional solidification. To be in a stationary state, the concentrations far in the solid and in the liquid have to be equal, $c = c_0$. The spike shows the solute concentration which builds up in front of the interface. Here, it passes into the coexistence region, instabilities are possible. From [23].

where \vec{e}_x is the unit vector in x -direction.

In the Gibbs-Thomson-Herring boundary condition, the constant temperature T_0 has to be generalized to T , leading to [23]

$$\mu - \mu_{\text{Eq}}(T) = -\frac{\gamma + \gamma''}{\Delta c} \kappa. \quad (2.14)$$

Expanding in first-order differential approximation around T_0 , one obtains as interface condition [23]

$$\tilde{\mu}(\text{solid interface}) = -\frac{\gamma + \gamma''}{\Delta c} \kappa - \left(\frac{\partial \mu}{\partial c} \right)' \Big|_{c=c'_{\text{Eq}}} \left| \frac{dc'_{\text{Eq}}}{dT} \right| G\xi \quad (2.15)$$

$$\tilde{\mu}(\text{liquid interface}) = -\frac{\gamma + \gamma''}{\Delta c} \kappa - \left(\frac{\partial \mu}{\partial c} \right) \Big|_{c=c_{\text{Eq}}} \left| \frac{dc_{\text{Eq}}}{dT} \right| G\xi. \quad (2.16)$$

The derivatives of c'_{Eq} and c_{Eq} with respect to the temperature are the inverse of the slopes of the solidus and liquidus, respectively.

2.2.4 Mullins-Sekerka instability

In this section, the stability of a planar interface is investigated in greater detail. Generally, instabilities drive the pattern-forming process in solidification and their understanding is of great interest. For binary alloys, the stability of a planar steady-state interface and its dependence on these control parameters is well understood theoretically [24].

As it turns out, the thermal and the chemical case as treated in sections 2.2.1 and 2.2.2 are equivalent. This can be seen by rewriting the equations in terms of the dimensionless diffusion field u , which is defined as $u = \frac{T-T_M}{L/c_p}$ in the case of thermal diffusion and as $u = \frac{\bar{\mu}}{\Delta c(\partial\mu/\partial c)}$ in the case of chemical diffusion [23]. In the definition, the unprimed liquid-phase parameters have been used for simplicity. To obtain the exact equivalence, the curvature dependence in Δc has again been neglected.

In this notation, both diffusion equations reduce to

$$D'\nabla^2 u = \partial_t u \quad (\text{solid}) \quad (2.17)$$

$$D\nabla^2 u = \partial_t u \quad (\text{liquid}), \quad (2.18)$$

where the subscripts at the diffusion coefficients have been omitted.

The continuity equation can be written as

$$v_n = D \left[\tilde{\beta}(\nabla u)_{\text{solid}} - (\nabla u)_{\text{liquid}} \right] \cdot \vec{n}, \quad (2.19)$$

where $\tilde{\beta} \equiv (D'c'_p)/(Dc_p)$ in the thermal model and $\tilde{\beta} \equiv M'/M$ in the chemical model.

For the Gibbs-Thomson relation, it follows

$$u(\text{interface}) = -d_0\kappa [a(\Theta) + a''(\Theta)], \quad (2.20)$$

with capillarity length d_0 . In the thermal model, the capillarity length is given by $d_0 = \frac{\gamma_0 T_M c_p}{L^2}$ and in the chemical model as $d_0 = \frac{\gamma_0}{(\partial\mu/\partial c)\Delta c^2}$, where the anisotropic surface energy is given in Eq. (2.7) as $\gamma(\Theta) = \gamma_0 a(\Theta)$.

The steady-state diffusion equation in the moving frame of reference, following the sample in the x direction with the interface velocity v , is given by [23]

$$\nabla^2 u + \frac{2}{l} \frac{\partial u}{\partial x} = 0. \quad (2.21)$$

Here, the diffusion length is introduced as $l = 2D/v$ and $l' = 2D'/v$ in the liquid and the solid, respectively. The solution of Eq. (2.21) and the continuity equation as given in Eq. (2.19) is

$$u = \begin{cases} \exp\left(-\frac{2x}{l}\right) - 1 & (\text{liquid}, x \geq 0) \\ 0 & (\text{solid}, x \leq 0) \end{cases}, \quad (2.22)$$

where the flat interface is placed at $x = 0$. At $x = +\infty$, the undercooling is required to be $u = -1$. At different undercoolings, it is impossible for a planar steady-state solution to exist.

Applying a small sinusoidal perturbation to this planar interface, one can perform a so-called linear stability analysis to obtain an analytical expression for the growth rate in dependence of the different perturbation modes [23]. While in chapter 3 the analysis is performed in details for the case of directional solidification of a liquid crystal mixture, here only the results are presented shortly. As it turns out, there are two competing terms determining the stability of a certain perturbation mode. The destabilizing term is proportional to the velocity and comes from the fact that a forward bulge in the interface leads to a larger temperature gradient and therefore to faster growth. The stabilizing

term comes from the surface energy. The interface possess a higher curvature at the bulge so that the surface energy applies a regularizing force.

The interplay between these two effects depends on the wavelength of the perturbation and determines their growth velocity. For sufficiently long wavelengths, the interface is always stable. This happens at a wavelength of $\lambda_s \simeq 2\pi\sqrt{(1 + \tilde{\beta})/2\sqrt{ld_0}}$, which sets a length scale for the problem.

In the case of directional solidification, yet another length scale appears in the system. The thermal gradient G introduces a thermal length

$$\frac{1}{l_T} \equiv \frac{G}{\Delta c_0} \left| \frac{dc_{Eg}}{dT} \right| \quad (2.23)$$

and similarly with primed constants. Here, a larger gradient G stabilizes the system.

Using the introduced lengths to summarize the stability criteria, the larger the capillary length d_0 and the diffusion length l and the smaller the thermal length l_T , the more stable is the system.

2.3 Phase-field model

In the previous section, the equations of motion for various solidification processes have been presented. Quite generally, the equations consist of a diffusion equation, which has to be solved in conjunction with a certain interface condition. The interface itself can be of a complex shape and evolves with time.

Even if the set of equations is rather simple, the complex shape of the interface makes it very difficult to solve the equations analytically. To solve them numerically, the interface shape has to be discretized in order to make it possible to apply the interface condition. Since the interface itself evolves with time, this discretization has to be adjusted to the changing shape at regular time intervals. This can become very time consuming, especially in three dimensions.

The phase-field method provides a way to circumvent this problem. Instead of tracking the interface explicitly, a phase-field variable ϕ is introduced, which is a function of position and time [25]. It is defined in the entire volume and describes for example whether a given space point is liquid or solid. In between the solid and the liquid phase, the phase field varies smoothly and continuously between the two values representing solid and liquid. In the models developed in this work, the solid phase is described by a value of $\phi = 1$, while the liquid is given by $\phi = 0$. Alternatively, one often finds in the literature $\phi = -1$ for the liquid phase. The interface position can be obtained from the phase-field variable as the contour line where ϕ is of an intermediary value. The actual definition of the value at which the interface position is taken might depend on the model used. In this work, it is usually taken at $\phi = \frac{1}{2}$.

The idea of having a density function, which varies continuously was already introduced by van der Waals [26] to model the liquid-gas interface more than a century ago. The phase-field theory itself is based on the Cahn-Hilliard [27] / Ginzburg-Landau type of classical field theoretic approaches to phase boundaries. Its origin lies in the model C of Halperin, Hohenberg and Ma [28], which was recast by Langer [29] and simultaneously by Collins and Levine [30]. The phase-field model has then been continuously been modified and adapted to be

thermodynamically consistent [31, 32] or extended to binary [33–35] or eutectic solidification [36–38].

One of the possible modifications is to use more than one scalar order parameter for different components in the case of eutectics or for different orientations of polycrystals. It can also be useful to express the order parameter in the form of a tensor, as is shown for liquid crystals in chapter 3.

In this section, the phase-field method is introduced. In section 2.3.1, the phase-field model for the solidification of a pure substance is presented. In section 2.3.2, the phase-field formalism is extended to include more than one phase-field variable to represent different grains with different crystalline orientation. In section 2.3.3, another concept to treat polycrystals is defined: a phase-field model with an orientation-field variable.

2.3.1 Phase-field model for solid-liquid phase transition

Besides the possibility of defining the order parameter physically as shown in section 2.1.2, it is often useful to rather see it as a mathematical indicator function, which is used to distinguish between the two phases, and write down the equation of motions purely phenomenologically.

The equations of motion of the phase-field model, corresponding to the solidification of a pure substance, can be obtained from a single Lyapounov functional \mathcal{F} as [39]

$$\tau(\Theta) \frac{\partial \phi}{\partial t} = - \frac{\delta \mathcal{F}}{\delta \phi} \quad (2.24)$$

$$\frac{\partial U}{\partial t} = \frac{D}{b\lambda} \nabla^2 \frac{\delta \mathcal{F}}{\delta U}, \quad (2.25)$$

the so-called variational form. Here, δ indicates the functional derivative

$$\frac{\delta \mathcal{F}}{\delta \phi} = \frac{\partial f}{\partial \phi} - \sum_{i=x,y,z} \partial_i \frac{\partial f}{\partial (\partial_i \phi)},$$

with $\mathcal{F} = \int f dV$. The independent variables are the nonconserved phase field ϕ and the conserved dimensionless enthalpy

$$U(u, \phi) = u - \frac{h(\phi)}{2}. \quad (2.26)$$

The angle of the interface normal can be obtained from the phase field as

$$\Theta = \tan \left(\frac{\partial \phi / \partial y}{\partial \phi / \partial x} \right) \quad (2.27)$$

and the phenomenological free energy can be written as

$$\mathcal{F} = \int dV \left[\frac{W(\Theta)^2}{2} |\vec{\nabla} \phi|^2 + f(\phi) + b\lambda \frac{u^2}{2} \right]. \quad (2.28)$$

The equations are expressed in dimensionless units, where the dimensionless temperature field is given by

$$u \equiv \frac{T - T_M}{L/c_p}. \quad (2.29)$$

Here, T is the temperature, T_M the melting temperature, L the latent heat of melting and c_p the specific heat at constant pressure. The characteristic time of attachment is given by $\tau(\Theta)$, λ is a dimensionless coupling parameter and D is the thermal diffusivity, which is assumed to be equal in both phases.

As mentioned before, using only one scalar phase-field variable makes it necessary to include the anisotropy in the surface energy and in the interface kinetics manually. This can be done by letting the constants $W(\Theta)$ and $\tau(\Theta)$ depend on the interface direction [40]. Similar to the surface energy, $W(\Theta)$ can be written as $W(\Theta) = W_0 a(\Theta)$, where W_0 turns out to be the interface width, which is usually of the order of a few atomic layers. The angle dependence of the anisotropy is again expressed in terms of the function $a(\Theta)$.

The equations of motion ensure that the free energy is minimized during the time evolution and that the system is driven towards a minimum of the free energy. The energy density f_0 can be obtained from the real free energies of the solid and the liquid phase. But as it turns out [39], the actual form of $f(\phi)$ is not very important, as long as it is of the shape of a double-well potential with minima for the two phases. In the following, the solid phase is given by $\phi = 1$ and the liquid phase by $\phi = -1$. Then, the simplest choice for $f(\phi)$ is

$$f(\phi) = -\frac{\phi^2}{2} + \frac{\phi^4}{4}. \quad (2.30)$$

With this choice comes a requirement to the function $h(\phi)$. To ensure that a unit amount of heat is produced at the interface $h(\phi)$ needs to satisfy

$$\frac{h(\phi = +1) - h(\phi = -1)}{2} = 1. \quad (2.31)$$

Using $h(\phi) = 15(\phi - 2\phi^3/3 + \phi^5/5)/8$ with $b = 16/15$ [39] fully defines a proper set of equations of motion, which in the isotropic case where $W(\Theta) = W_0$ and $\tau(\Theta) = \tau_0$ can be expressed in terms of u and ϕ as

$$\tau_0 \partial_t \phi = W_0^2 \nabla^2 \phi - f'(\phi) - \lambda g'(\phi) u \quad (2.32)$$

$$\partial_t u = D \nabla^2 u + \frac{h'(\phi)}{2} \partial_t \phi. \quad (2.33)$$

Here, an additional function

$$g(\phi) = \frac{b}{2} h(\phi) = \phi - 2\phi^3/3 + \phi^5/5 \quad (2.34)$$

has been introduced.

To simplify the calculations, it is possible to replace $h(\phi)$ by a much simpler function, giving up the possibility of obtaining the equations of motion from a variational functional but without changing the physical properties.

It is useful, to write down a free energy, from which the equations of motion can be obtained in a variational form in the isothermal case

$$\mathcal{F}_{\text{iso}} = \int dV \left[\frac{W(\Theta)^2}{2} |\vec{\nabla} \phi|^2 + f(\phi) + \lambda g(\phi) u \right] \quad (2.35)$$

and write the equations of motion as

$$\tau(\Theta) \partial_t \phi = -\frac{\delta \mathcal{F}_{\text{iso}}}{\delta \phi} \quad (2.36)$$

$$\partial_t u = D \nabla^2 u + \frac{h'(\phi)}{2} \partial_t \phi. \quad (2.37)$$

Choosing h and g as before leads to exactly the same set of equations of motion. But now it is possible to use $h(\phi) = \phi$ as a much simpler and computational more effective function, keeping the form of $g(\phi)$. One can now imagine $g(\phi)$ as a tilting function, which determines which phase is energetically preferred for a given normalized temperature. It has the properties that the minima of the free energy stay fixed at values of $\phi = \pm 1$ independent of u — the first and the second derivative of $g(\phi)$ with respect to ϕ have to vanish at $\phi = \pm 1$.

The form of the free energy density including the temperature dependence $f(\phi) + u\lambda g(\phi)$ is shown in figure 2.12. The solid line corresponds to an under-cooled system (the temperature is below the melting temperature, $u < 0$). The solid phase $\phi = 1$ is energetically favorable. At the melting temperature $u = 0$, both phases are of the same energy, shown with the dashed line. For $u > 0$, above the melting temperature, the liquid phase is of lower energy, as shown with the dotted line.

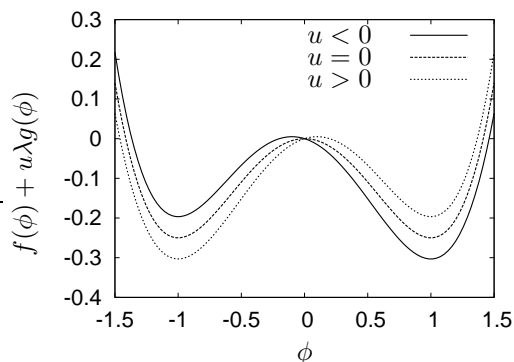


Figure 2.12: Bulk free energy density in dependency of the phase-field variable ϕ . For temperatures below the melting temperature, ($u < 0$), the solid phase ($\phi = 1$) is preferred. At melting ($u = 0$), the energies of both phases are equal while at $u > 0$ the liquid phase ($\phi = -1$) is preferred.

From the formal point of view, it is therefore more consistent to describe the first-order phase transition with a set of equations which can both be derived from the same free-energy functional. Writing down the equation of motion for the temperature field purely phenomenologically is computationally more efficient and reduces to the same free-boundary problem in the limit of small interface thickness [39].

To be able to perform quantitative simulations with the phase-field model, the equations of motion have to reduce to the free boundary problem for the solidification of a pure substance, given in section 2.2.1. The interface condition for the dimensionless temperature is given in Eq. (2.20) as

$$u(\text{interface}) = -d_0\kappa [a(\Theta) + a''(\Theta)] - \beta(\Theta)v_n, \quad (2.38)$$

where the second term is due to the interface kinetics and was neglected in Eq. (2.20). It is proportional to the kinetic coefficient $\beta(\Theta)$ and the normal velocity v_n . It also exhibits anisotropy and becomes important for fast solidification. It arises from the fact that during the solidification process, the atoms in

the liquid have to find their position in the crystal lattice. The capillary length is given by $d_0 = \gamma_0 T_M c_p / L^2$ as introduced in section 2.2.4.

In the limit of thin interface width W_0 , a similar equation can be derived for the phase-field model as shown in the asymptotic matching, for example by Karma et al. [39]. One finds that

$$d_0 = a_1 \frac{W_0}{\lambda} \quad (2.39)$$

and

$$\beta(\Theta) = a_1 \left[\frac{\tau(\Theta)}{\lambda W(\Theta)} - a_2 \frac{W(\Theta)}{D} \right]. \quad (2.40)$$

The constants $a_1 = I/J$ and $a_2 = (\mathcal{K} + JF)/I$ depend on the exact form of the free energy and are obtained from the integrals

$$I = \int_{-\infty}^{\infty} dx (\partial_x \phi_0)^2, \quad (2.41)$$

$$J = - \int_{-\infty}^{\infty} dx \partial_x \phi_0 g^0, \quad (2.42)$$

$$F = \int_0^{\infty} dx \phi_0, \quad (2.43)$$

$$\mathcal{K} = \int_{-\infty}^{\infty} dx \partial_x \phi_0 g^0 \int_0^{x'} dx' \phi_0, \quad (2.44)$$

where here $\phi_0 = \tanh(x/\sqrt{2})$ and $g_0 = g(\phi_0)$.

It is important to point out that the physics of the simulated system is given by the capillary length and the kinetic coefficient. In the phase-field simulations, the interface width W can be artificially increased without changing the physics of the system. This makes the phase-field method so powerful. Using the real interface width, which is of the order of angstroms, is computationally very inefficient if one is interested in microstructure formations which takes place over length scales of microns, especially in three dimensions. Instead, one can artificially increase the interface width when changing $\tau(\Theta)$ and λ accordingly, and leave d_0 and $\beta(\Theta)$ unchanged.

It is also worth noticing that one can choose λ in such a way that the kinetic constant is always zero and hence the interface kinetic vanishes. This is relevant at low undercoolings for a large class of materials, especially for metallic systems with fast kinetics [39, 41–43].

A nickel dendrite, grown with this model in three dimensions and with anisotropic surface energy is shown in figure 2.13.

2.3.2 Multi-phase-field models

To simulate phase transformations with more than two phases, for example eutectic solidification, multi-phase-field models have been developed [44–48]. They usually contain one phase-field variables per phase ϕ_i , which represents the local fraction of this phase. Depending on the model, the free energy can also depend on the corresponding molar fraction [45–48].

The interest of this work is focused on the polycrystalline growth in single-phase materials, where the different grains possess the same chemical composition and lattice structure. Only the local crystalline orientation differs. Here,

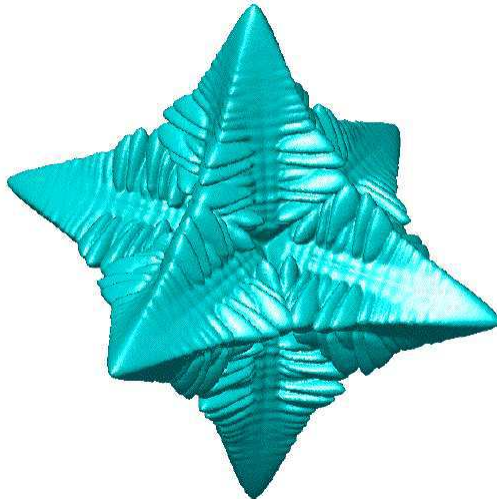


Figure 2.13: The result of a three-dimensional phase-field simulation with anisotropy. From [43].

a model proposed by Chen and Yang [44] is presented, where the different grains are represented by different nonconserved order parameters η_i . In grain i , $\eta_i = \pm 1$, while all other fields $\eta_{j \neq i} = 0$. A possible polycrystalline structure and the corresponding phase-fields are shown in figure 2.14.

The free energy can be seen as a generalization of the free energy of the phase-field model with only one phase field. In general, it can be written as

$$\mathcal{F} = \int dV \left[f_0(\eta_i) + \sum_i \frac{\kappa_i}{2} (\vec{\nabla} \eta_i)^2 \right]. \quad (2.45)$$

One can identify the gradient terms similar to the single-phase model, where the grain boundary properties for different grains can be adapted individually by varying the κ_i . For isotropic grain boundary properties, all κ_i are equal.

The free energy density f_0 consists of a double-well potential for each grain i and a cross term, which penalizes two order parameters being not equal to zero at the same space point. It can then be written as [44]

$$f_0(\eta_i) = \sum_i \left(-\frac{\alpha}{2} \eta_i^2 + \frac{\beta}{4} \eta_i^4 \right) + \gamma \sum_i \sum_{j \neq i} \eta_i^2 \eta_j^2. \quad (2.46)$$

With this choice for the free energy, the energy is always minimized when one order parameter is at plus or minus one and all the others are zero. Going from grain i ($\eta_i = 1, \eta_j = 0$) to grain j ($\eta_j = 1, \eta_i = 0$) is represented by a decrease in the value of field η_i and by a simultaneous increase in the value of field η_j , which is shown in figure 2.15. This leads to an increase in the free energy, which can be associated with the interface or grain boundary energy. The grain boundary energy depends on the model parameters and can be defined in dependence on the crystalline orientations associated with the grains. This grain boundary

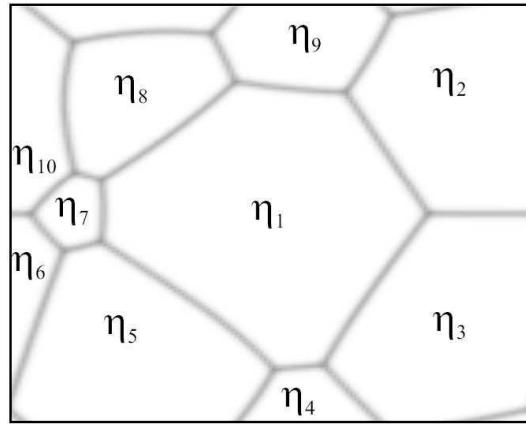


Figure 2.14: Schematic representation of a polycrystalline material, consisting of different grains which are separated by grain boundaries. The grains are of different orientation and are represented by different phase-field variables η_i . Inside of grain i , $\eta_i = \pm 1$ and all other $\eta_{j \neq i} = 0$. From [49].

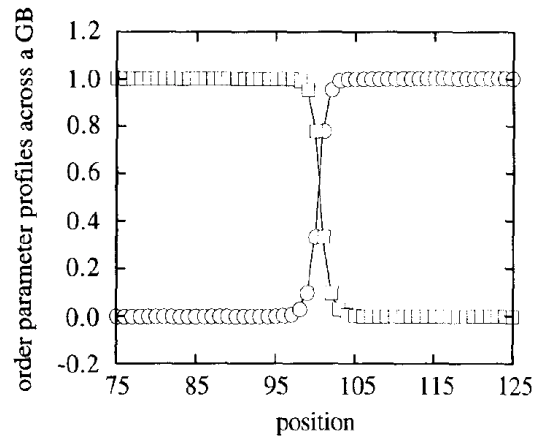


Figure 2.15: The variation of two phase-field variables in a grain boundary. In the left grain, $\eta_i = 1$, shown in squares. As the value of η_i decreases in the grain boundary, η_j increases (circles). Finally, in the right grain, $\eta_i = 0$ and $\eta_j = 1$. From [44].

energy in dependence of the orientation has, however, to be inserted in the model manually — the form of the grain boundary energy does not arise naturally.

The equations of motion for the different fields are then again obtained in the standard way for nonconserved order parameters as

$$\tau_i \partial_t \eta_i = -\frac{\delta \mathcal{F}}{\delta \eta_i}, \quad (2.47)$$

for all phase-field variables η_i .

In general, a polycrystalline material consists of thousands of grain with different orientations. Each grain should be represented with a different order parameter, which makes it computationally difficult to treat.

2.3.3 Phase-field models with orientation field

The multi-phase-field models work very well, simulations with thousands of fields are possible and give a relatively realistic picture of the grain growth in polycrystals. Fundamental problems arise, however, simulating the effect of grain rotation, and the nucleation of new grains with an arbitrary crystalline orientation is difficult to simulate with these kind of models.

Beside these practical reasons, it is from the fundamental point of view interesting to develop a different model, which is based on more physical picture of the degrees of freedom. In two dimensions, a grain boundary between two crystals has two geometrical degrees of freedom [50], an inclination angle Θ and a crystallographic misorientation $\delta\theta$. It is natural to search for a numerical description based on two parameters in two dimensions as well — and accordingly in three dimensions.

Methods have been established which include this effect of the crystalline orientation in the phase-field model [50–57], and which have also been extended to three dimensions [56–58] recently. The main idea is to introduce two order parameters, one being the phase-field variable ϕ and the other a local orientation variable θ . The phase-field variable can also be seen as representing the local order. It is chosen to be $\phi = 1$ in the solid or perfect crystal, $\phi = 0$ in the liquid or without any crystalline order. Near a grain boundary, the local order will decrease and one can assume values of $\phi < 1$, having a minimum value of ϕ_{\min} in the grain boundary. To measure the local orientation with respect to a fixed coordinate system, one single orientation field θ is necessary. The crystal is assumed to have N -fold symmetry, so that θ should be in the domain $-\pi/N < \theta < \pi/N$ [50]. This symmetry has to be taken into account when calculating angle differences numerically.

The main challenge in developing such a phase-field model for polycrystals is to find a suitable free energy which includes both the phase field and the orientation field. The dependence on the phase field is taken similarly to the pure substance case, consisting of a double-well potential with minima for the ordered ($\phi = 1$) and the unordered phases ($\phi = 0$) and a gradient term, which leads to smooth interfaces. The free energy cannot explicitly depend on the angle since there are no preferred orientations; all that counts are angle differences. It turns out that to obtain localized grain boundaries, it is not sufficient to use the usual second order gradient term $(\nabla\theta)^2$, but as lowest order a linear term $|\nabla\theta|$ has to be included. This leads to cusps in the free energy and to singularities

in the equation of motion, which have to be treated explicitly in the numerical simulations.

The free energy can then be written as [50]

$$\mathcal{F} = \int dV \left[f(\phi, T) + \frac{\alpha^2}{2} \Gamma^2 (\nabla\phi, \theta - \Theta) + sg(\phi)|\nabla\theta| + \frac{\epsilon^2}{2} h(\phi)|\nabla\theta|^2 \right]. \quad (2.48)$$

The function $\Gamma(\nabla\phi, \theta - \Theta)$ defines the anisotropy of the system, where the interface inclination can be obtained from the phase field as given in Eq. 2.27. The coupling strengths between ϕ and $\nabla\theta$ are given by s and ϵ , and $g(\phi)$ and $h(\phi)$ are monotonically increasing functions [50].

The equations of motion for ϕ and θ are obtained by minimizing the free energy,

$$Q(\phi, \nabla\theta)\tau_\phi\partial_t\phi = -\frac{\delta\mathcal{F}}{\delta\phi} \quad (2.49)$$

$$= \alpha^2\nabla^2\phi - f'(\phi) - g'(\phi)s|\nabla\theta| - h'(\phi)\frac{\epsilon^2}{2}|\nabla\theta|^2 \quad (2.50)$$

and

$$P(\phi, \nabla\theta)\tau_\theta\partial_t\theta = -\frac{\delta\mathcal{F}}{\delta\theta} \quad (2.51)$$

$$= \nabla \cdot \left[h(\phi)\epsilon^2\nabla\theta + g(\phi)s\frac{\nabla\theta}{|\nabla\theta|} \right], \quad (2.52)$$

where always the explicit form is true for the isotropic case $\Gamma = \nabla\phi$ only. The time constants τ_ϕ and τ_θ are uniform and constant, while the inverse mobility functions P and Q contain the information about the kinetic coefficients and the anisotropy.

As for the phase-field model for pure substance solidification presented in section 2.3.1, the equation of motion for the temperature can generally be derived in a variational way, but is here written down phenomenologically as

$$\partial_t T = D\nabla^2 T + \frac{L}{c_p}\partial_t\phi, \quad (2.53)$$

where L is again the latent heat and c_p the specific heat.

A detailed analysis of this phase-field model with orientation field can be found in [50]. In figure 2.16, one of their results is shown, namely a two dimensional simulation of polycrystalline growth in an undercooled liquid. One can see how the dendritic microstructure emerges where different colors represent different local orientations θ . Since the anisotropy leading to the dendritic shape depends on the local orientation, also the macroscopic shape does. After a while, the heat is extracted at a fixed rate from the system to cause the entire system to freeze.

In figure 2.17, a three-dimensional simulation from the group of Gránásy and Pusztai [56, 58] is shown. In their model, the two-dimensional description using a scalar angle variable is successfully generalized to three dimensions. The three degrees of freedom of a possible misorientation are expressed in terms of quaternions, which allow a very convenient description of angle differences. However, the symmetries of the crystal have to be treated manually by regarding all possible invariant configurations of the crystal when calculating the angle gradients.

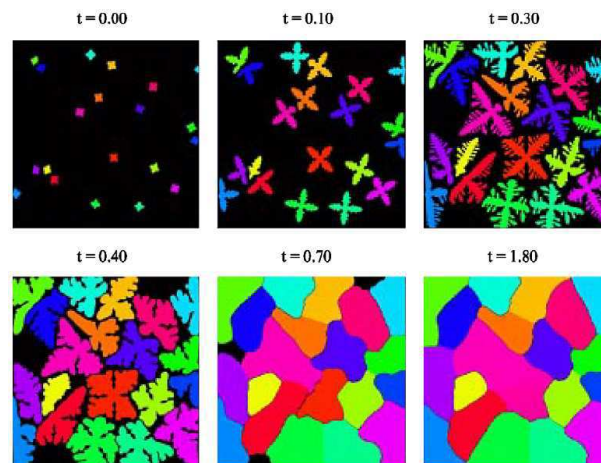


Figure 2.16: Solidification of different grains from their undercooled melt. The local crystalline orientation is different for the different grains, as shown in different colors. Also the macroscopic shape depends on this orientations through the surface anisotropy, therefore the dendritic shapes of the grains are oriented in different directions. After some time, the heat is extracted at a constant rate and the entire system solidifies. From [50].

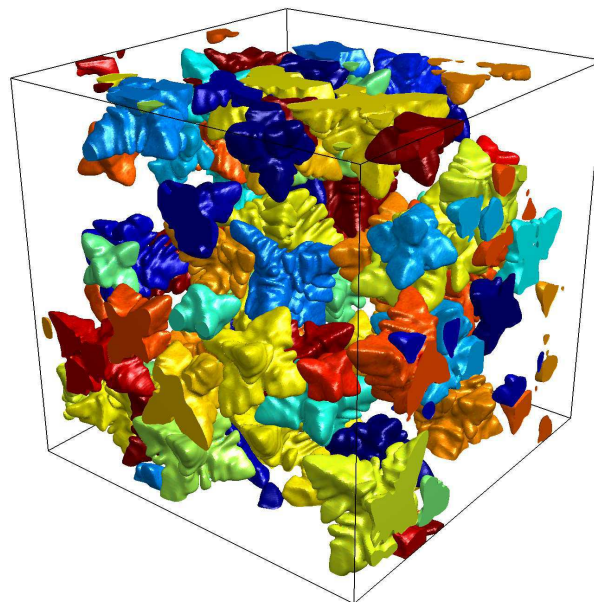


Figure 2.17: Three-dimensional simulation of dendrites with different crystalline orientations. From [59].

Chapter 3

Phase-Field Model for Liquid Crystal Solidification

In this chapter, a model for liquid-crystal solidification is developed using a tensor order parameter. This is of both, technical as well as of physical interest. Technically, it is demonstrated how the advantages of a tensor as a description for an orientation variable can be used in a phase-field model. The standard phase-field equations are generalized, using a rank two tensor as order parameter instead of a scalar field. It is shown how physical quantities such as surface tension or capillary length can be related to the model parameters. Finally, the stability of the steady-state planar interface is studied and a generalized dispersion relation for the directional “solidification” of a liquid crystal “alloy” is presented, taking into account the nematic orientation.

The physical interest in this topic is mainly rooted in experiments that are performed to investigate the microstructures formed during solidification. In experiments on metallic alloys, it is very difficult to explore completely the range of possible instabilities, because very high growth speeds are needed. For this reason, twenty years ago, it was suggested to use the nematic-isotropic phase transition as an “analog” for the solid-liquid transition. Indeed, directional “solidification” of a mixture of a liquid crystal and an isotropic “impurity” produces patterns that are very similar to solidification patterns. The characteristics of the nematic-isotropic phase transition (which is only weakly first order) and of the involved phase diagrams makes a wide range of length scale ratios accessible; in addition, the mixtures are transparent which simplifies observations. These experiments have helped to clarify many issues on pattern formation in parameter regimes that are difficult to access in metallic alloys [60].

However, so far, relatively little work has been done to clarify the role of the nematic director field in the pattern formation process. In the initial quantitative comparison between theory and experiments, a discrepancy was noted which corresponded to a capillary length that was a factor 100 different from the expected value. A stability analysis including the director field and using a relatively crude approximation of strong anchoring at the boundary [61] concluded that the elastic energy in the nematic phase is insufficient to explain this discrepancy. Later, it was found that a satisfactory explanation can be given taking into account the coupling of the director field and the sample walls [62].

Here, a completely different question is investigated. The interest lies in the role of the anisotropy created by the director field for the pattern formation process. This is motivated by recent experimental and theoretical results showing that the crystalline anisotropy is not only important for the stability of dendrites, but also for cellular structures similar to those observed in the liquid crystal experiments. In thin-sample experiments, it was found that stable arrays of cells form only in crystals which have a sufficiently strong anisotropy in the sample plane. For weakly anisotropic crystals, cells are not stable, but can split in two or be overgrown by neighboring cells, such that the front as a whole exhibits spatiotemporal chaos. It is well known that the surface tension of the nematic-isotropic interface in liquid crystals depends on the local orientation of the director with respect to the interface. However, contrary to crystals where the orientation is fixed, the director field can adapt dynamically to the changing shape of the growth front. What is the influence of this interplay on the shape and stability of cellular interfaces?

A privileged tool to investigate this kind of question is the phase-field method, as introduced in section 2.3. Since it is based on free energy functionals of Ginzburg-Landau type, it seems quite natural to incorporate a director field

described by the de Gennes quadrupolar order parameter. An interesting question to address is the relevance of such a model for the description of pattern formation on macroscopic scales. Indeed, in phase-field models, an enormous efficiency gain can be obtained by “upscaling” the interface thickness. Can this “trick” still be used for liquid crystals?

This chapter is organized as follows. The physics of liquid crystals is explained in section 3.1, finishing with a phenomenological free energy for a nematic-isotropic phase transition. Based on this free energy, in section 3.2, a model for the dynamics of a nematic-isotropic interface in an alloy of a liquid crystal and an isotropic impurity is developed. It generalizes the well-known phase-field models for the directional solidification of alloys, which were developed to investigate the effect of anisotropy on the cell formation [63, 64].

Next, in section 3.3, the physical parameters are related to the model parameters, and an expression for the anisotropic surface tension in dependence of the nematic orientation is derived. With this surface tension, an anchoring condition which is satisfied by the director field at the interface is obtained in section 3.4. This condition is used to generalize the linear stability analysis of Bechhoefer and Langer [61]. Simulations of a weakly perturbed planar interface are performed and the growth rates of the perturbations are extracted. The results are in good agreement with the theoretical predictions, as shown in section 3.5. In addition, simulations of cellular structures are carried out, finding that, indeed, the director field can have a substantial effect on pattern stability. For instance, if a lateral bias is introduced, a transition from steady to oscillating and drifting cells is observed. In the end of this chapter, a short conclusion about this model is drawn together with an outlook about how it could be further improved.

3.1 Physics of liquid crystals

In this chapter, materials are described whose mechanical and symmetry properties are, under certain conditions, between those of a liquid and those of a crystal. They are therefore called “liquid crystals”, even if “mesomorphic phases” would be more accurate [65].

To define a liquid crystal, it is useful to first recall the distinction between a crystal and a liquid. The main difference is the average position of the component’s center of gravity. The substance components might be molecules or groups of molecules and are most generally called primitive pattern in the following. In the crystal, they are located on a periodic three-dimensional lattice, so that the density-density correlation function, describing the probability of finding one primitive pattern at point \vec{r} and an identical one at \vec{r}' , remains finite and can be written as

$$\lim_{|\vec{r}-\vec{r}'|\rightarrow\infty} \langle \rho(\vec{r})\rho(\vec{r}') \rangle = F(\vec{r}-\vec{r}'), \quad (3.1)$$

where F is a periodic function characterizing the lattice structure.

For an isotropic liquid, the components are not ordered. The probability of finding a pattern at \vec{r} and an identical pattern at \vec{r}' is given simply by the average particle density $\bar{\rho}$, so that

$$\lim_{|\vec{r}-\vec{r}'|\rightarrow\infty} \langle \rho(\vec{r})\rho(\vec{r}') \rangle \simeq \bar{\rho}^2. \quad (3.2)$$

Liquid crystals can now be defined as systems, in which a liquid-like order exists at least in one direction [65] and in which the density-density correlation function depends on the orientation of $\vec{r}-\vec{r}'$, hence where anisotropy is present.

Following this definition, one can obtain mesophases by either imposing no positional order in at least one dimension or by introducing additional degrees of freedoms not coinciding with the centers of gravity. In this work, the main interest is focused on nematics, which belong to the first group, having no positional order at all, but an anisotropic correlation function, which depends on the local orientation. The simplest case of nematics, the so-called uniaxial nematics, are usually made of rod-like or disc-like molecules, as shown in figure 3.1. Liquid crystals with a crystal-like order in one and two dimensions are called smectics and columnar phases, respectively. For further and more general information about liquid crystals, the reader is referred to “The Physics of Liquid Crystals” by de Gennes and Prost [65].

To summarize the properties important for this work, uniaxial nematics possess no long-range order and the scattering in the X-ray pattern is hence diffuse. There is, however, an order in the orientation of the rod- or disc-like molecules, which can be described by a unit vector \vec{n} , around which the molecules are completely rotationally invariant. The states of the director \vec{n} and $-\vec{n}$ as well as left and right are indistinguishable in the system: the molecules must be identical to their mirror image.

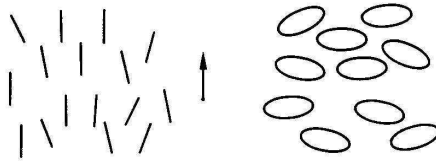


Figure 3.1: Nematic mesophase, made of rod-like (left) and disc-like (right) molecules. From [65].

3.1.1 Order parameter

Being interested in the order of the liquid crystal, one can investigate its symmetry. The nematic phase is of lower symmetry than the isotropic phase, it is “more ordered”, as shown in figure 3.2. To describe this order more quantitatively, it is useful to define an order parameter, which vanishes for symmetry reasons in the isotropic phase but is has a finite value in the nematic phase. This can be done in two ways: microscopically or macroscopically.

Microscopic definition

To define the order parameter microscopically, one needs to distinguish between the average nematic orientation \vec{n} and the local orientation of one molecule \vec{a} , which can be expressed with the polar angles θ and φ . \vec{n} is chosen to be aligned in x -directions, \vec{a} will be distributed around \vec{n} with some distribution function $f(\theta)d\Omega$, where the angle θ gives the misorientation with respect to the x -axis. Due to the complete cylindrical symmetry, the function f does not depend on φ .

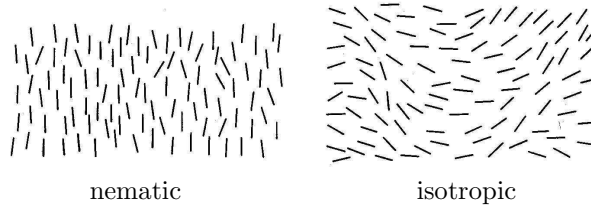


Figure 3.2: Left: “More ordered” nematic phase. Right: Orderless isotropic phase. From [65].

Since the directions \vec{n} and $-\vec{n}$ are equivalent, $f(\theta)$ is also periodic in π , so that $f(\theta) = f(\pi - \theta)$.

To obtain an order parameter, one can investigate the different moments of the function f . Due to the periodicity in π , the average vanishes identically, there is no average dipole. The first non-trivial multipole is the quadrupole, which is defined as

$$S = \frac{1}{2} \langle 3 \cos^2 \theta - 1 \rangle = \int f(\theta) \frac{1}{2} (3 \cos^2 \theta - 1) d\Omega. \quad (3.3)$$

For parallel alignment, $S = 1$, for perpendicular $S = -1/2$ and for an entirely random orientation, where f does not depend on θ , $S = 0$. One can therefore use S as a measure of the alignment.

Macroscopic definition

Another typical difference between the isotropic liquid and the nematic mesophase is found in the measurement of all macroscopic tensor properties. Here, the magnetic response \vec{M} to a field \vec{H} is taken, given by the magnetic susceptibility

$$M_i = \chi_{ij} H_j. \quad (3.4)$$

For a static field, one has a symmetric tensor $\hat{\chi}$. In isotropic liquids, one finds that $\chi_{ij} = \chi \delta_{ij}$, whereas in uniaxial nematics, choosing the x -axis parallel to \vec{n} , one has

$$\hat{\chi} = \begin{pmatrix} \chi_{\parallel} & 0 & 0 \\ 0 & \chi_{\perp} & 0 \\ 0 & 0 & \chi_{\perp} \end{pmatrix}.$$

To define an order parameter which vanishes in the isotropic phase, one extracts the anisotropic part Q_{ij} of the magnetic susceptibility

$$\begin{aligned} Q_{ij} &= G \left(\chi_{ij} - \frac{1}{3} \delta_{ij} \sum_k \chi_{kk} \right) \\ &= G \begin{pmatrix} \frac{2}{3}(\chi_{\parallel} - \chi_{\perp}) & 0 & 0 \\ 0 & -\frac{1}{3}(\chi_{\parallel} - \chi_{\perp}) & 0 \\ 0 & 0 & -\frac{1}{3}(\chi_{\parallel} - \chi_{\perp}) \end{pmatrix}, \end{aligned} \quad (3.5)$$

where G is a normalization factor and the last equality is valid for the uniaxial nematics only.

3.1.2 Angle and absolute value representation

In this subsection, the idea of a tensorial order parameter is generalized and a second representation in terms of an orientation angle and the absolute value of the order parameter is presented. For numerical purposes, it is very useful to express the system in terms of tensors. Then, the symmetry of the system is automatically taken care of, a tensor of rank two is rotationally invariant under a rotation of $\pi/2$, as are the rod-like liquid crystals. In some cases, however, it is very useful to express the two degrees of freedom of the tensor in more natural variables, namely the orientation as an angle θ and the magnitude as a scalar q .

Tensor components in terms of angle and absolute value

In the diagonalized form, the tensor \hat{Q} for a uniaxial nematic can be written as

$$\hat{Q} = \begin{pmatrix} q & 0 & 0 \\ 0 & -q/2 & 0 \\ 0 & 0 & -q/2 \end{pmatrix}, \quad (3.6)$$

where q is proportional to the average magnitude of the orientation of the system.

This diagonal form corresponds to a certain liquid crystal orientation, here described by its angle $\theta = 0$. Allowing arbitrary orientations in the same coordinate system, one can apply a rotation to get a more general form of \hat{Q} . In this work, the liquid crystal is orientated in the x - y -plane, it has only one rotational degree of freedom, the rotational axis being in z -direction.

Generally, a rotation around the z -axis by an angle θ can be expressed by the rotational matrix

$$\hat{a} = \begin{pmatrix} \cos \theta & -\sin \theta & 0 \\ \sin \theta & \cos \theta & 0 \\ 0 & 0 & 1 \end{pmatrix}, \quad (3.7)$$

and rotating a tensor \hat{T} leads to

$$\tilde{T}_{\mu\nu} = \sum_{ij} a_{\mu i} a_{\nu j} T_{ij}. \quad (3.8)$$

Applying this operation to \hat{Q} gives the desired relation between the tensor notation and the corresponding angle and absolute value representation

$$Q_{xx} = \frac{1}{4}q [1 + 3 \cos(2\theta)] \quad (3.9)$$

$$Q_{xy} = \frac{3}{4}q \sin(2\theta) \quad (3.10)$$

$$Q_{yy} = \frac{1}{4}q [1 - 3 \cos(2\theta)] \quad (3.11)$$

$$Q_{zz} = -\frac{1}{2}q \quad (3.12)$$

$$Q_{iz} = Q_{zi} = 0 \quad \text{with } i = x, y. \quad (3.13)$$

The angle θ only appears with a factor 2, which is due to the rotational invariance under a rotation of π .

Angle and absolute value in terms of tensor components

To obtain q and θ as functions of the tensor components Q_{ij} , it is useful to investigate the eigenvalues of the tensorial matrix. The eigenvalues of \hat{Q} are given by $\{q, -q/2, -q/2\}$. This can be seen easily from the diagonal representation, as given in Eq. (3.6). The corresponding eigenvectors are $(\cos \theta, \sin \theta, 0)$, $(-\sin \theta, \cos \theta, 0)$, $(0, 0, 1)$. Therefore, the orientation θ can be obtained from the eigenvectors and the order parameter q from the eigenvalues of \hat{Q} .

The eigenvalues of

$$\hat{Q} = \begin{pmatrix} Q_{xx} & Q_{xy} & 0 \\ Q_{xy} & Q_{yy} & 0 \\ 0 & 0 & Q_{zz} \end{pmatrix} \quad (3.14)$$

are

$$\frac{1}{2} \left(Q_{xx} + Q_{yy} + \sqrt{(Q_{xx} - Q_{yy})^2 + 4Q_{xy}^2} \right), \quad (3.15)$$

$$\frac{1}{2} \left(Q_{xx} + Q_{yy} - \sqrt{(Q_{xx} - Q_{yy})^2 + 4Q_{xy}^2} \right), \quad (3.16)$$

and

$$Q_{zz}. \quad (3.17)$$

The corresponding eigenvectors are

$$\left\{ \frac{1}{2Q_{xy}} \left(Q_{xx} - Q_{yy} + \sqrt{(Q_{xx} - Q_{yy})^2 + 4Q_{xy}^2} \right), 1, 0 \right\}, \quad (3.18)$$

$$\left\{ \frac{1}{2Q_{xy}} \left(Q_{xx} - Q_{yy} - \sqrt{(Q_{xx} - Q_{yy})^2 + 4Q_{xy}^2} \right), 1, 0 \right\}, \quad (3.19)$$

and

$$\{0, 0, 1\}. \quad (3.20)$$

The eigenvector, corresponding to the largest eigenvalue, gives the orientation of the director,

$$\vec{n} = \begin{pmatrix} \cos(\theta) \\ \sin(\theta) \\ 0 \end{pmatrix} \propto \begin{pmatrix} \frac{Q_{xx} - Q_{yy} + \sqrt{(Q_{xx} - Q_{yy})^2 + 4Q_{xy}^2}}{2Q_{xy}} \\ 1 \\ 0 \end{pmatrix}. \quad (3.21)$$

With Eqs. (3.9) to (3.13), one can see that $q = -2Q_{zz}$ and that the angle can be obtained from the eigenvector corresponding to the largest eigenvalue,

$$\theta = \arctan \left[\frac{2Q_{xy}}{(Q_{xx} - Q_{yy} + \sqrt{(Q_{xx} - Q_{yy})^2 + 4Q_{xy}^2})} \right]. \quad (3.22)$$

In the case where \hat{Q} is already in the diagonal form ($Q_{xy} = 0$), $\theta = 0$ for $Q_{xx} = q$ and $\theta = \pi/2$ for $Q_{yy} = q$.

3.1.3 Liquid crystal free energy

In this subsection, a phenomenological free energy for a nematic liquid crystal is developed.

The total free energy f_0 can, most generally, be divided into a potential term f_W and an interaction term f_D ,

$$f_0(\hat{Q}, \vec{\nabla}\hat{Q}) = f_W(\hat{Q}) + f_D(\vec{\nabla}\hat{Q}). \quad (3.23)$$

The potential term describes the dependence of the free energy on the temperature T for temperatures close to the phase-transition temperature T_C and in the absence of deformations. The energy contributions due to different orientations \vec{n} of the liquid crystal in different regions of the system are treated in the distortion term f_D .

Potential free energy

For purely geometrical reasons, the nematic-isotropic phase transition must be of first order [65]. In a Landau-type theory, the potential term can be expanded in powers of the order parameter, leading to

$$f_W(\hat{Q}) = \frac{A}{2}\tilde{\delta}(\hat{Q}) + \frac{B}{3}\Delta(\hat{Q}) + \frac{C}{4}\tilde{\delta}(\hat{Q})^2 \quad (3.24)$$

with

$$\tilde{\delta}(\hat{Q}) = \sum_{i,j} Q_{ij}Q_{ij} \quad (3.25)$$

and

$$\Delta(\hat{Q}) = \sum_{i,j,k} Q_{ij}Q_{jk}Q_{ki}, \quad (3.26)$$

where the possible constant term is set to zero and terms of order \hat{Q}^5 are neglected. A , B and C are constants which are temperature-dependent and shift the potential in such a way that one of the phases is preferred. All terms appearing are rotationally invariant as they should be.

In the diagonal representation, one can determine $\tilde{\delta}$ and Δ as functions of q , leading to

$$\tilde{\delta}(q) = \frac{3}{2}q^2, \quad (3.27)$$

and

$$\Delta(q) = \frac{3}{4}q^3. \quad (3.28)$$

The potential part of the free energy can then be written in terms of q and θ as

$$f_W(q) = \frac{3}{4}Aq^2 + \frac{1}{4}Bq^3 + \frac{9}{16}Cq^4, \quad (3.29)$$

where one can see that it is rotationally invariant since it does not depend on θ .

In a pure substance, the constants A , B , and C are functions of the temperature T only. In the case of an liquid crystal alloy, they depend on the chemical

potential $\mu(c, T)$, which itself is a function of concentration c and temperature T and are given by

$$\begin{aligned} A &= 2 + 6(\mu - \mu_{\text{Eq}}), \\ B &= -12 - 12(\mu - \mu_{\text{Eq}}), \\ C &= 8/3. \end{aligned}$$

At equilibrium ($\mu = \mu_{\text{Eq}}$), the minima in the free energy for the nematic ($q = 1$) and the isotropic phase ($q = 0$) have the same energy. For $\mu < \mu_{\text{Eq}}$, the energy for the nematic phase is lowered, whereas for $\mu > \mu_{\text{Eq}}$ it is raised and therefore the isotropic phase is preferred.

The equilibrium potential μ_{Eq} itself depends on the temperature, which is usually fixed by choosing an impurity concentration c_0 . The corresponding temperature T_0 can then be obtained from the phase diagram as shown in figure 2.9.

Distortion free energy

The ideal, nematic “single crystal” has molecules, which are all (in average) aligned in the same direction $\pm \vec{n}$, where both configurations (“up” and “down”) are equal. In real systems, however, there are usually external constraints such as limiting surfaces of the sample or external fields which destroy this ideal configuration. One has to deal with deformations in the nematic phase, so that the definition of \hat{Q} has to be extended to include arbitrary average orientations $\vec{n}(\vec{r})$. The order parameter can then be constructed as $Q_{ij} = Q(T) (n_i n_j - \frac{1}{3} \delta_{ij})$, where the molecules are aligned along a common direction \vec{n} [65], which is normalized and does not change in length, $|\vec{n}|^2 = 1$. In a weakly distorted system, the magnitude of the anisotropy is unchanged, only the orientation of the optical axis (\vec{n}) has been rotated, and therefore

$$Q_{ij}(\vec{r}) \approx Q(T) \left[n_i(\vec{r}) n_j(\vec{r}) - \frac{1}{3} \delta_{ij} \right]. \quad (3.30)$$

The distortion free energy can be constructed from all possible independent combination of $\nabla \vec{n}$ and \vec{n} , which leads in second order to [66]

$$\begin{aligned} f_D^n &= \frac{1}{2} k_{11} (\text{div } \vec{n})^2 + \frac{1}{2} k_{22} (\vec{n} \cdot \text{curl } \vec{n} - \frac{2\pi}{p_0})^2 + \frac{1}{2} k_{33} (\vec{n} \times \text{curl } \vec{n})^2 \\ &\quad - k_{24} \text{div } (\vec{n} \cdot \text{div } \vec{n} + \vec{n} \times \text{curl } \vec{n}), \end{aligned} \quad (3.31)$$

with height of the cholesterical helix pitch p_0 . Terms one to three correspond to the terms introduced by Frank [67] (k_{11} : splay, k_{22} : twist, k_{33} : bend), see figure 3.3.

The fourth term corresponds to saddle splay and is a pure surface term. Therefore, in the integral over the entire volume, term four can be transformed into a surface integral and therefore be neglected when the bulk is much larger than the surface.

The distortion free energy can also be constructed by using the invariance theory [66]. The invariant terms can be constructed from polynomials in Q_{ij} and $\partial_k Q_{ij}$, which leads in second order to

$$f_D^{\hat{Q}} = \frac{1}{2} c_1 (\partial_k Q_{ij}) (\partial_k Q_{ij}) + \frac{1}{2} c_2 (\partial_j Q_{ij}) (\partial_k Q_{ik}) + \frac{1}{2} c_3 (\partial_k Q_{ij}) (\partial_j Q_{ik})$$

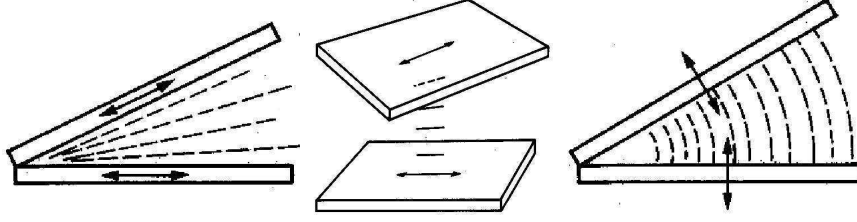


Figure 3.3: Possible deformations in a nematic liquid crystal: splay, twist and bend, from left to right. From [65].

$$\begin{aligned}
& +\frac{1}{2}c_6 Q_{ij}(\partial_i Q_{k,l})(\partial_j Q_{kl}) - \frac{1}{2}c_4 \epsilon_{ijk} Q_{il}(\partial_j Q_{kl}) \\
= & \frac{1}{2}c_1 \sum_{i,j,k} (\partial_k Q_{ij})^2 + \frac{1}{2}c_2 \sum_i \left(\sum_j \partial_j Q_{ij} \right)^2 \\
& +\frac{1}{2}c_3 \sum_{i,j,k} (\partial_k Q_{ij})(\partial_j Q_{ik}) + \frac{1}{2}c_6 \sum_{ij} \left(Q_{ij} \sum_{k,l} (\partial_i Q_{k,l})(\partial_j Q_{kl}) \right) \\
& -\frac{1}{2}c_4 \sum_{i,j,k} \left(\epsilon_{ijk} \sum_l (Q_{il})(\partial_j Q_{kl}) \right).
\end{aligned}$$

For $\hat{Q} = Q(T)(n_i n_j - \frac{1}{3}\delta_{ij})$, the elastic constants are related to the phenomenological constants by [66]

$$\begin{aligned}
c_1 Q^2 &= \frac{1}{6}(3k_{22} - k_{11} + k_{33}) \\
c_2 Q^2 &= k_{11} - 2k_{24} \\
c_3 Q^2 &= 2k_{24} - k_{22} \\
c_4 Q^2 &= 2\frac{2\pi}{p_0}k_{22} \\
c_6 Q^2 &= \frac{1}{2}(k_{33} - k_{11}).
\end{aligned}$$

In the simplest case, where $k_{11} = k_{22} = k_{33} = 2k_{24} = K$ and $p_0 \rightarrow \infty$, there is only one gradient term which is proportional to c_1 . This corresponds to an isotropic system. A non-zero value for c_2 leads to a preferred orientation perpendicular or normal to the interface, depending on the sign of c_2 [68], as discussed further later in this chapter.

The resulting distortion free energy term can then be written as

$$f_D(\nabla \hat{Q}) = \frac{1}{2}c_1 (\partial_k Q_{ij})^2 + \frac{1}{2}c_2 (\partial_j Q_{ij})^2, \quad (3.32)$$

and is used in this work.

For completeness, the distortion free energy is also given in terms of q and θ , so that

$$f_{D1} = \frac{1}{2}c_1 \sum_{\alpha,\beta,\gamma} (\partial_\gamma Q_{\alpha\beta})^2$$

$$\begin{aligned}
&= \frac{1}{2}c_1 \frac{3}{2} [3q^2 ((\partial_x \theta)^2 + (\partial_y \theta)^2) + ((\partial_x q)^2 + (\partial_y q)^2)] \quad (3.33) \\
f_{D_2} &= \frac{1}{2}c_2 \sum_{\alpha} \left(\sum_{\beta} \partial_{\beta} Q_{\alpha\beta} \right)^2 \\
&= \frac{1}{2}c_2 \left\{ \frac{9}{4}q^2 (\partial_x \theta)^2 + \frac{9}{4}q^2 (\partial_y \theta)^2 \right. \\
&\quad + \frac{1}{8} (5 + 3 \cos(2\theta)) (\partial_x q)^2 + \frac{1}{8} (5 - 3 \cos(2\theta)) (\partial_y q)^2 \\
&\quad + \frac{3}{4} \sin(2\theta) (\partial_x q) (\partial_y q) \\
&\quad - \frac{3}{4} q \sin(2\theta) (\partial_x q) (\partial_x \theta) + \frac{3}{4} q \sin(2\theta) (\partial_y q) (\partial_y \theta) \\
&\quad + \frac{3}{4} q (\cos(2\theta) + 3) (\partial_x q) (\partial_y \theta) \\
&\quad \left. + \frac{3}{4} q (\cos(2\theta) - 3) (\partial_y q) (\partial_x \theta) \right\}. \quad (3.34)
\end{aligned}$$

3.2 Phase-field model

To describe a system with a complicated geometry, instead of keeping track of its boundary explicitly, one can introduce a so-called phase-field variable in the entire system, as explained in section 2.3.

In the case of the liquid crystal, the phase-field variable or order parameter arises quite naturally as the director \hat{Q} , where its absolute value $\propto q$ gives its phase (nematic or isotropic), but contains in addition the information of the orientation direction. Here, the isotropic phase is given by $q = 0$, the nematic phase by $q = 1$ and the interface position is taken at the contour line where $q = 1/2$.

3.2.1 Chemical potential

The directional solidification of a metal alloy has already been introduced in section 2.2.3. In this work, the interest is focused on liquid crystals and the metal alloy is replaced by a mixture of a nematic liquid crystal and a pure isotropic substance, which acts as impurity.

To obtain the equation of motion for the normalized diffusion field, the same normalization as in section 2.2.4 is used, $u = \frac{\tilde{\mu}}{\Delta c (\partial \mu / \partial c)} \equiv \frac{\tilde{\mu}}{\lambda}$ with $\tilde{\mu} = \mu - \mu_{E_q}$ and coupling parameter $\lambda \equiv \Delta c (\partial \mu / \partial c)$. In this work, Δc and $\partial \mu / \partial c$ are assumed to be constant, which corresponds to linear and parallel solidus and liquidus lines in the phase diagram in figure 2.9.

The equation of motion in terms of the phase-field formalism is derived in section 2.3.1 for the thermal model. As shown in section 2.2.4, the thermal model is, expressed in terms of the normalized diffusion field, in a good approximation identical to the chemical model. With Eq. (2.33) and the simplest choice of $h(\phi)$, for diffusion equation follows

$$\partial_t u = D \nabla^2 u + \partial_t q.$$

Please note that q varies between 0 and 1 while in the derivation of the phase-field model, ϕ is defined between -1 and 1 . The diffusion coefficient is given in section 2.2.2 as $D = M \left. \frac{\partial \mu}{\partial c} \right|_{T_0}$. Here, for simplicity M and therefore also D are taken to be equal in the nematic and the isotropic phase.

In addition to the time evolution of the normalized chemical potential u , the equations of motion for tensor components Q_{ij} have to be derived, which is done in the following subsection. This is the main difference to the already existing models for the directional solidification of alloys [63, 64].

3.2.2 Tensor components

In this subsection, the equations of motions for an uniaxial nematic liquid crystal are derived, starting from the total free energy functional

$$\mathcal{F}_0(\hat{Q}, \nabla \hat{Q}) = \int \left[f_W(\hat{Q}) + f_D(\nabla \hat{Q}) \right] dV. \quad (3.35)$$

At equilibrium, the free energy is at a local minimum. Assuming that the system approaches its equilibrium configuration by minimizing its free energy continuously with time, the equations of motions can be obtained as

$$\tau \partial_t Q_{ij} = - \frac{\delta \mathcal{F}}{\delta Q_{ij}}.$$

This is the standard way for a nonconserved order parameter, compare section 2.3. The derivation is performed in the most general way, using only symmetry properties of the system. The actual form of the free energy, e.g. the potential constants A , B , and C or the gradient constants c_1 and c_2 do not yet enter the calculation.

The form of Q_{ij} , however, is important. The five tensor components on which \mathcal{F} depends are given by

$$\hat{Q} = \begin{pmatrix} Q_{xx} & Q_{xy} & 0 \\ Q_{yx} & Q_{yy} & 0 \\ 0 & 0 & Q_{zz} \end{pmatrix}. \quad (3.36)$$

From the five variables there are only two independent ones, corresponding for example to the angle of the orientation vector to the x -axis and its absolute value, as described in section 3.1.2. In the following derivation, the three additional variables are eliminated from the free energy using Lagrange multipliers and the equations of motion for the remaining two variables are presented.

Due to the system symmetries, there are three conditions on the five variables, which can be written as

$$g_1(Q_{xy}, Q_{yx}) = Q_{xy} - Q_{yx} = 0 \quad (3.37)$$

$$g_2(Q_{xx}, Q_{yy}, Q_{zz}) = Q_{xx} + Q_{yy} + Q_{zz} = 0 \quad (3.38)$$

$$g_3(\hat{Q}) = \tilde{\delta}(\hat{Q})^3 - 6\Delta(\hat{Q})^2 = 0. \quad (3.39)$$

The first condition is due to the fact that \hat{Q} is symmetric, the second one states that the trace is zero and the third condition arises from the fact that the nematic is uniaxial. The third condition in this 2d-case is equivalent to the

condition that two eigenvalues have to be equal. The eigenvalues are given in Eqs. (3.15) to (3.17), where the first eigenvalue is the largest one, corresponding to the direction of the orientation. Hence, the other two have to be equal, so that

$$\tilde{g}_3(\hat{Q}) = 2Q_{zz} - Q_{xx} - Q_{yy} + \sqrt{(Q_{xx} - Q_{yy})^2 + 4Q_{xy}Q_{yx}} = 0. \quad (3.40)$$

Using Lagrange multipliers to introduce these three conditions into the free energy leads to

$$\begin{aligned} f &= f_0 + \lambda_1(Q_{xy} - Q_{yx}) + \lambda_2(Q_{xx} + Q_{yy} + Q_{zz}) \\ &\quad + \lambda_3 \left(2Q_{zz} - Q_{xx} - Q_{yy} + \sqrt{(Q_{xx} - Q_{yy})^2 + 4Q_{xy}Q_{yx}} \right), \end{aligned} \quad (3.41)$$

where f_0 is the free energy of the system, given e.g. by Eq. (3.23).

To obtain an expression for the Lagrange multipliers λ_i , one differentiates the free energy with respect to the different variables

$$\frac{\delta \mathcal{F}}{\delta Q_{xx}} = \frac{\delta \mathcal{F}_0}{\delta Q_{xx}} + \lambda_2 - \lambda_3 \left(1 - \frac{Q_{xx} - Q_{yy}}{\sqrt{(Q_{xx} - Q_{yy})^2 + 4Q_{xy}Q_{yx}}} \right) \quad (3.42)$$

$$\frac{\delta \mathcal{F}}{\delta Q_{xy}} = \frac{\delta \mathcal{F}_0}{\delta Q_{xy}} + \lambda_1 + \lambda_3 \left(\frac{2Q_{yx}}{\sqrt{(Q_{xx} - Q_{yy})^2 + 4Q_{xy}Q_{yx}}} \right) \quad (3.43)$$

$$\frac{\delta \mathcal{F}}{\delta Q_{yx}} = \frac{\delta \mathcal{F}_0}{\delta Q_{yx}} - \lambda_1 + \lambda_3 \left(\frac{2Q_{xy}}{\sqrt{(Q_{xx} - Q_{yy})^2 + 4Q_{xy}Q_{yx}}} \right) \quad (3.44)$$

$$\frac{\delta \mathcal{F}}{\delta Q_{yy}} = \frac{\delta \mathcal{F}_0}{\delta Q_{yy}} + \lambda_2 - \lambda_3 \left(1 + \frac{Q_{xx} - Q_{yy}}{\sqrt{(Q_{xx} - Q_{yy})^2 + 4Q_{xy}Q_{yx}}} \right) \quad (3.45)$$

$$\frac{\delta \mathcal{F}}{\delta Q_{zz}} = \frac{\delta \mathcal{F}_0}{\delta Q_{zz}} + \lambda_2 + 2\lambda_3, \quad (3.46)$$

where $\mathcal{F}_i = \int f_i dV$.

Since the three conditions $g_1 = 0$, $g_2 = 0$ and $\tilde{g}_3 = 0$ are valid for all times, their time derivative has to be zero, so that

$$\begin{aligned} 0 &= \frac{\partial g_1}{\partial t} = \partial_t Q_{xy} - \partial_t Q_{yx} = -\frac{\delta \mathcal{F}}{\delta Q_{xy}} + \frac{\delta \mathcal{F}}{\delta Q_{yx}} \\ &= \frac{\delta \mathcal{F}_0}{\delta Q_{yx}} - \frac{\delta \mathcal{F}_0}{\delta Q_{xy}} - 2\lambda_1 + \lambda_3 \left(\frac{2(Q_{xy} - Q_{yx})}{\sqrt{(Q_{xx} - Q_{yy})^2 + 4Q_{xy}Q_{yx}}} \right). \end{aligned}$$

Solving for λ_1 gives

$$\begin{aligned} \lambda_1 &= \frac{1}{2} \left[\frac{\delta \mathcal{F}_0}{\delta Q_{yx}} - \frac{\delta \mathcal{F}_0}{\delta Q_{xy}} + \lambda_3 \left(\frac{2(Q_{xy} - Q_{yx})}{\sqrt{(Q_{xx} - Q_{yy})^2 + 4Q_{xy}Q_{yx}}} \right) \right] \\ &\stackrel{Q_{xy}=Q_{yx}}{=} \frac{1}{2} \left[\frac{\delta \mathcal{F}_0}{\delta Q_{yx}} - \frac{\delta \mathcal{F}_0}{\delta Q_{xy}} \right]. \end{aligned} \quad (3.47)$$

Similarly, for g_2 , it follows

$$\lambda_2 = -\frac{1}{3} \left(\frac{\delta \mathcal{F}_0}{\delta Q_{xx}} + \frac{\delta \mathcal{F}_0}{\delta Q_{yy}} + \frac{\delta \mathcal{F}_0}{\delta Q_{zz}} \right). \quad (3.48)$$

For \tilde{g}_3 , one obtains

$$0 = \frac{\partial g_3}{\partial t} = -2 \frac{\delta \mathcal{F}}{\delta Q_{zz}} + \frac{\delta \mathcal{F}}{\delta Q_{xx}} + \frac{\delta \mathcal{F}}{\delta Q_{yy}} + \frac{(Q_{xx} - Q_{yy}) \left(\frac{\delta \mathcal{F}}{\delta Q_{yy}} - \frac{\delta \mathcal{F}}{\delta Q_{xx}} \right) - 2 \left(Q_{yx} \frac{\delta \mathcal{F}}{\delta Q_{xy}} + Q_{xy} \frac{\delta \mathcal{F}}{\delta Q_{yx}} \right)}{\sqrt{(Q_{xx} - Q_{yy})^2 + 4Q_{xy}Q_{yx}}}.$$

Using the expressions for the functional derivatives along with the condition $Q_{xy} = Q_{yx}$ and solving for λ_3 leads to

$$\lambda_3 = \frac{1}{8} \left[\frac{\delta \mathcal{F}_0}{\delta Q_{xx}} + \frac{\delta \mathcal{F}_0}{\delta Q_{yy}} - 2 \frac{\delta \mathcal{F}_0}{\delta Q_{zz}} + \frac{(Q_{xx} - Q_{yy}) \left(\frac{\delta \mathcal{F}_0}{\delta Q_{yy}} - \frac{\delta \mathcal{F}_0}{\delta Q_{xx}} \right) - 2Q_{xy} \left(\frac{\delta \mathcal{F}_0}{\delta Q_{xy}} + \frac{\delta \mathcal{F}_0}{\delta Q_{yx}} \right)}{\sqrt{(Q_{xx} - Q_{yy})^2 + 4Q_{xy}^2}} \right]. \quad (3.49)$$

The equations of motion are then given by

$$\tau \partial_t Q_{xx} = -\frac{2}{3} \frac{\delta \mathcal{F}_0}{\delta Q_{xx}} + \frac{1}{3} \frac{\delta \mathcal{F}_0}{\delta Q_{yy}} + \frac{1}{3} \frac{\delta \mathcal{F}_0}{\delta Q_{zz}} + \lambda_3 \left(1 - \frac{Q_{xx} - Q_{yy}}{\sqrt{(Q_{xx} - Q_{yy})^2 + 4Q_{xy}^2}} \right) \quad (3.50)$$

$$\tau \partial_t Q_{xy} = -\frac{1}{2} \left(\frac{\delta \mathcal{F}_0}{\delta Q_{xy}} + \frac{\delta \mathcal{F}_0}{\delta Q_{yx}} \right) - \lambda_3 \frac{2Q_{xy}}{\sqrt{(Q_{xx} - Q_{yy})^2 + 4Q_{xy}Q_{yx}}} \quad (3.51)$$

$$\tau \partial_t Q_{yx} = -\frac{1}{2} \left(\frac{\delta \mathcal{F}_0}{\delta Q_{xy}} + \frac{\delta \mathcal{F}_0}{\delta Q_{yx}} \right) - \lambda_3 \frac{2Q_{xy}}{\sqrt{(Q_{xx} - Q_{yy})^2 + 4Q_{xy}Q_{yx}}} \quad (3.52)$$

$$\tau \partial_t Q_{yy} = \frac{1}{3} \frac{\delta \mathcal{F}_0}{\delta Q_{xx}} - \frac{2}{3} \frac{\delta \mathcal{F}_0}{\delta Q_{yy}} + \frac{1}{3} \frac{\delta \mathcal{F}_0}{\delta Q_{zz}} + \lambda_3 \left(1 + \frac{Q_{xx} - Q_{yy}}{\sqrt{(Q_{xx} - Q_{yy})^2 + 4Q_{xy}^2}} \right) \quad (3.53)$$

$$\tau \partial_t Q_{zz} = \frac{1}{3} \frac{\delta \mathcal{F}_0}{\delta Q_{xx}} + \frac{1}{3} \frac{\delta \mathcal{F}_0}{\delta Q_{yy}} - \frac{2}{3} \frac{\delta \mathcal{F}_0}{\delta Q_{zz}} - 2\lambda_3. \quad (3.54)$$

Eliminating Q_{yx} , Q_{yy} and Q_{zz}

Using the three constraints $g_1 = 0$, $g_2 = 0$ and $\tilde{g}_3 = 0$, one can eliminate three of the five variables of \hat{Q} and end up with two equations of motion. The first condition leads right away to

$$Q_{yx} = Q_{xy}, \quad (3.55)$$

as already used. The second condition can be easily re-arranged to give $Q_{yy} = -Q_{zz} - Q_{xx}$. To eliminate Q_{zz} , one solves Eq. (3.40) for Q_{zz} , replaces Q_{yy} and obtains

$$Q_{zz} = \frac{1}{4} Q_{xx} - \frac{1}{4} \sqrt{9Q_{xx}^2 + 8Q_{xy}^2}, \quad (3.56)$$

where the negative sign is used since $Q_{zz} < 0$ (as can be seen in the diagonal representation, where $Q_{zz} = -q/2$). Using this again to express Q_{yy} as function

of Q_{xx} and Q_{xy} only, one obtains

$$Q_{yy} = -\frac{5}{4}Q_{xx} + \frac{1}{4}\sqrt{9Q_{xx}^2 + 8Q_{xy}^2}. \quad (3.57)$$

Therefore, the equations of motion can be reduced to

$$\begin{aligned} \tau \partial_t Q_{xx} &= -\frac{2}{3} \frac{\delta \mathcal{F}_0}{\delta Q_{xx}} + \frac{1}{3} \frac{\delta \mathcal{F}_0}{\delta Q_{yy}} + \frac{1}{3} \frac{\delta \mathcal{F}_0}{\delta Q_{zz}} \\ &+ \lambda_3 \left(1 - \frac{\frac{9}{4}Q_{xx} - \frac{1}{4}\sqrt{9Q_{xx}^2 + 8Q_{xy}^2}}{\sqrt{\left(\frac{9}{4}Q_{xx} - \frac{1}{4}\sqrt{9Q_{xx}^2 + 8Q_{xy}^2}\right)^2 + 4Q_{xy}^2}} \right) \end{aligned} \quad (3.58)$$

$$\tau \partial_t Q_{xy} = -\frac{1}{2} \left(\frac{\delta \mathcal{F}_0}{\delta Q_{xy}} + \frac{\delta \mathcal{F}_0}{\delta Q_{yx}} \right) - \lambda_3 \frac{2Q_{yx}}{\sqrt{\left(\frac{9}{4}Q_{xx} - \frac{1}{4}\sqrt{9Q_{xx}^2 + 8Q_{xy}^2}\right)^2 + 4Q_{xy}^2}} \quad (3.59)$$

with

$$\begin{aligned} \lambda_3 &= \frac{1}{8} \left[\frac{\delta \mathcal{F}_0}{\delta Q_{xx}} + \frac{\delta \mathcal{F}_0}{\delta Q_{yy}} - 2 \frac{\delta \mathcal{F}_0}{\delta Q_{zz}} \right. \\ &+ \left. \frac{\overbrace{\left(\frac{9}{4}Q_{xx} - \frac{1}{4}\sqrt{9Q_{xx}^2 + 8Q_{xy}^2}\right)}^{\frac{3}{2}q \cos(2\theta)} \left(\frac{\delta \mathcal{F}_0}{\delta Q_{yy}} - \frac{\delta \mathcal{F}_0}{\delta Q_{xx}}\right) - \overbrace{2Q_{xy}}^{\frac{3}{2}q \sin(2\theta)} \left(\frac{\delta \mathcal{F}_0}{\delta Q_{xy}} + \frac{\delta \mathcal{F}_0}{\delta Q_{yx}}\right)}{\underbrace{\sqrt{\left(\frac{9}{4}Q_{xx} - \frac{1}{4}\sqrt{9Q_{xx}^2 + 8Q_{xy}^2}\right)^2 + 4Q_{xy}^2}}_{\frac{3}{2}q}} \right]. \end{aligned} \quad (3.60)$$

Anisotropic systems

A system with anisotropy can be described by a free energy with gradient coefficients c_1 and c_2

$$\begin{aligned} f_0(\hat{Q}) &= \frac{A}{2} \sum_{i,j} Q_{ij} Q_{ij} + \frac{B}{3} \sum_{i,j,k} Q_{ij} Q_{jk} Q_{ki} + \frac{C}{4} \left(\sum_{i,j} Q_{ij} Q_{ij} \right)^2 \\ &+ \frac{c_1}{2} \sum_{i,j,k} (\partial_i Q_{jk})^2 + \frac{c_2}{2} \sum_j \left(\sum_i \partial_i Q_{ij} \right)^2. \end{aligned}$$

The functional derivatives of $\mathcal{F}_0 = \int f_0 dV$ are given by

$$\begin{aligned} \frac{\delta \mathcal{F}_0}{\delta Q_{xx}} &= A Q_{xx} + B(Q_{xx}^2 + Q_{xy}^2) + C Q_{xx} (Q_{xx}^2 + 2Q_{xy}^2 + Q_{yy}^2 + Q_{zz}^2) \\ &- c_1 (\partial_{xx} Q_{xx} + \partial_{yy} Q_{xx}) - c_2 (\partial_{xx} Q_{xx} + \partial_{xy} Q_{xy}) \quad (3.61) \\ \frac{\delta \mathcal{F}_0}{\delta Q_{xy}} &= A Q_{xy} + B Q_{xy} (Q_{xx} + Q_{yy}) + C Q_{xy} (Q_{xx}^2 + 2Q_{xy}^2 + Q_{yy}^2 + Q_{zz}^2) \end{aligned}$$

$$\begin{aligned}
& -c_1 (\partial_{xx} Q_{xy} + \partial_{yy} Q_{xy}) - c_2 (\partial_{xx} Q_{xy} + \partial_{xy} Q_{yy}) \quad (3.62) \\
\frac{\delta \mathcal{F}_0}{\delta Q_{yx}} = & A Q_{xy} + B Q_{xy} (Q_{xx} + Q_{yy}) + C Q_{xy} (Q_{xx}^2 + 2Q_{xy}^2 + Q_{yy}^2 + Q_{zz}^2) \\
& -c_1 (\partial_{xx} Q_{xy} + \partial_{yy} Q_{xy}) - c_2 (\partial_{yy} Q_{xy} + \partial_{xy} Q_{xx}) \quad (3.63)
\end{aligned}$$

$$\begin{aligned}
\frac{\delta \mathcal{F}_0}{\delta Q_{yy}} = & A Q_{yy} + B (Q_{xy}^2 + Q_{yy}^2) + C Q_{yy} (Q_{xx}^2 + 2Q_{xy}^2 + Q_{yy}^2 + Q_{zz}^2) \\
& -c_1 (\partial_{xx} Q_{yy} + \partial_{yy} Q_{yy}) - c_2 (\partial_{yy} Q_{yy} + \partial_{xy} Q_{xy}) \quad (3.64)
\end{aligned}$$

$$\begin{aligned}
\frac{\delta \mathcal{F}_0}{\delta Q_{zz}} = & A Q_{zz} + B Q_{zz}^2 + C Q_{zz} (Q_{xx}^2 + 2Q_{xy}^2 + Q_{yy}^2 + Q_{zz}^2) \cdot \\
& -c_1 (\partial_{xx} Q_{zz} + \partial_{yy} Q_{zz}) \cdot \quad (3.65)
\end{aligned}$$

The equations of motion are obtained using Eqs. (3.58), (3.59) and (3.60) and are not given explicitly here.

Equation of motion in terms of θ and q

A more intuitive way of writing down the equations of motion is in the representation of absolute value q and orientation angle θ , related to \hat{Q} by Eqs. (3.9) to (3.13). One can write the equations of motion as

$$\begin{aligned}
\tau \partial_t Q_{xx} = & -\frac{1}{4} A q [1 + 3 \cos(2\theta)] - \frac{1}{8} B q^2 [1 + 3 \cos(2\theta)] - \frac{3}{8} C q^3 [1 + 3 \cos(2\theta)] \\
& + c_1 (\partial_{xx} + \partial_{yy}) \left[\frac{1}{4} q (1 + 3 \cos 2\theta) \right] + \lambda_3 [1 - \cos(2\theta)] \\
\tau \partial_t Q_{xy} = & -\frac{3}{4} A q \sin(2\theta) - \frac{3}{8} B q^2 \sin(2\theta) - \frac{9}{8} C q^3 \sin(2\theta) \\
& + c_1 (\partial_{xx} + \partial_{yy}) \left[\frac{3}{4} q \sin 2\theta \right] - \lambda_3 \sin(2\theta)
\end{aligned}$$

with

$$\begin{aligned}
\lambda_3 = & -\frac{3}{4} c_1 q [(\partial_x \theta)^2 + (\partial_y \theta)^2] \\
& + \frac{1}{8} c_2 \{ -\sin(2\theta) (\partial_{xy} q) - 3 \cos(2\theta) [(\partial_x q) (\partial_y \theta) + (\partial_y q) (\partial_x \theta)] \\
& + 6q \sin(2\theta) (\partial_x \theta) (\partial_y \theta) - 3q \cos(2\theta) (\partial_{xy} \theta) \\
& + \frac{1}{2} [1 - \cos(2\theta)] (\partial_{xx} q) + 3 \sin(2\theta) (\partial_x q) (\partial_x \theta) - 3q [1 - \cos(2\theta)] (\partial_x \theta)^2 \\
& + \frac{3}{2} q \sin(2\theta) (\partial_{xx} \theta) \\
& + \frac{1}{2} [1 + \cos(2\theta)] (\partial_{yy} q) - 3 \sin(2\theta) (\partial_y q) (\partial_y \theta) - 3q [1 + \cos(2\theta)] (\partial_y \theta)^2 \\
& - \frac{3}{2} q \sin(2\theta) (\partial_{yy} \theta) \}.
\end{aligned}$$

Using

$$\tau \partial_t Q_{xx} = \frac{1}{4} [1 + 3 \cos(2\theta)] \partial_t q - \frac{3}{2} q \sin(2\theta) \partial_t \theta \quad (3.66)$$

and

$$\tau \partial_t Q_{xy} = \frac{3}{4} \sin(2\theta) \partial_t q + \frac{3}{2} q \cos(2\theta) \partial_t \theta, \quad (3.67)$$

one can express the equations of motion in q and θ , leading to

$$\begin{aligned}
\tau \partial_t q &= -Aq - \frac{1}{2}Bq^2 - \frac{3}{2}Cq^3 \\
&+ c_1 \left\{ (\partial_{xx}q) + (\partial_{yy}q) - 3q \left[(\partial_x\theta)^2 + (\partial_y\theta)^2 \right] \right\} \\
&+ c_2 \left\{ (\partial_{xx}q) \frac{1}{4} \left[\frac{5}{3} + \cos(2\theta) \right] - (\partial_xq)(\partial_x\theta) \frac{1}{2} \sin(2\theta) \right. \\
&\quad - (\partial_x\theta)^2 \frac{1}{2} q [3 + \cos(2\theta)] - (\partial_{xx}\theta) \frac{1}{4} q \sin(2\theta) \\
&\quad + (\partial_{yy}q) \frac{1}{4} \left[\frac{5}{3} - \cos(2\theta) \right] + (\partial_yq)(\partial_y\theta) \frac{1}{2} \sin(2\theta) \\
&\quad - (\partial_y\theta)^2 \frac{1}{2} q [3 - \cos(2\theta)] + (\partial_{yy}\theta) \frac{1}{4} q \sin(2\theta) \\
&\quad + (\partial_{xy}q) \frac{1}{2} \sin(2\theta) + [(\partial_xq)(\partial_y\theta) + (\partial_yq)(\partial_x\theta)] \frac{1}{2} \cos(2\theta) \\
&\quad \left. - (\partial_x\theta)(\partial_y\theta)q \sin(2\theta) + (\partial_{xy}\theta) \frac{1}{2} q \cos(2\theta) \right\} \\
\tau \partial_t \theta &= c_1 \left\{ [(\partial_{xx}\theta) + (\partial_{yy}\theta)] + \frac{2}{q} [(\partial_x\theta)(\partial_xq) + (\partial_y\theta)(\partial_yq)] \right\} \\
&+ c_2 \left\{ \frac{\sin(2\theta)}{12q} [-(\partial_{xx}q) + (\partial_{yy}q)] + \frac{1}{2} [(\partial_{xx}\theta) + (\partial_{yy}\theta)] \right. \\
&\quad \left. + \frac{1}{q} [(\partial_x\theta)(\partial_xq) + (\partial_y\theta)(\partial_yq)] + \frac{\cos(2\theta)}{6q} (\partial_{xy}q) \right\}.
\end{aligned}$$

3.3 Physical parameters

In this section, the physical parameters are related to the model parameters. In section 3.3.1, an expression for the interface thickness in terms of gradient constants is obtained, deriving the equilibrium solution of the phase-field equations. Then, in section 3.3.2, the surface tension is obtained as a function of the interface orientation relative to the liquid crystal orientation. Finally, in section 3.3.3, the capillary length and the kinetic coefficient are calculated, leading to a condition on the model parameters to eliminate kinetic effects, a regime used in all the simulations presented in this work.

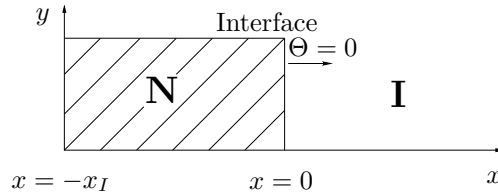


Figure 3.4: System with planar interface. The interface is parallel to the y -axes and located at $x = 0$.

3.3.1 Equilibrium solution and interface thickness

In the phase-field model, the interface is extended over a certain width ξ . The interface width is a physical parameter which arises naturally from the free energy and depends on the model parameters c_1 and c_2 .

To obtain an expression for the interface thickness of the equilibrium solution, one can investigate a system with a planar interface, leading to an effectively one-dimensional problem. If the interface is aligned in the y -direction (corresponding to an interface angle $\Theta = 0$ as shown in figure 3.4), the tensor $\hat{Q}(x)$ is a function of x only. Assuming further that the orientation is constant in the entire system ($\theta = \text{const}$), one can express the equation of motion in terms of the absolute value q and the angle θ as the two degrees of freedom as

$$\tau \partial_t q = -Aq - \frac{1}{2}Bq^2 - \frac{3}{2}Cq^3 + \left\{ c_1 + c_2 \frac{1}{4} \left[\frac{5}{3} + \cos(2\theta) \right] \right\} (\partial_{xx} q).$$

Searching for a stationary solutions with $u = 0$ yield

$$0 = 2(-q + 3q^2 - 2q^3) + W^2(\theta)(\partial_{xx} q),$$

where $W^2(\theta) = c_1 + c_2 \frac{1}{4} \left[\frac{5}{3} + \cos(2\theta) \right]$. This can be written as

$$\partial_{xx} q(x) = \frac{2}{W^2(\theta)} [q(x) - 3q(x)^2 + 2q(x)^3], \quad (3.68)$$

which is identical to the standard scalar phase-field equation and has well-known solution

$$q(x) = \frac{1}{2} \left[1 - \tanh \left(\frac{x}{\xi} \right) \right], \quad (3.69)$$

with interface thickness

$$\xi(\theta) = \sqrt{2}W(\theta) = \sqrt{2c_1 + \frac{c_2}{2} \left[\frac{5}{3} + \cos(2\theta) \right]}. \quad (3.70)$$

3.3.2 Surface energy

The surface energy γ is given by the difference in energy of a system with interface and a system without interface, divided by the area (3d) or length (2d) of the interface S ,

$$\gamma = \frac{\mathcal{F}(\text{with interface}) - \mathcal{F}(\text{without Interface})}{S}. \quad (3.71)$$

With the free energy as chosen in this chapter, the free energy for a homogeneous system without interface is identical to zero, $\mathcal{F}(\text{without Interface}) = 0$. For a planar interface, as shown in figure 3.4, with constant nematic orientation θ and interface orientation in y direction (interface angle $\Theta = 0$) at equilibrium, the free energy is given by

$$\mathcal{F} = \int \left[\frac{3}{2}q^2(1-q)^2 + \frac{3}{4}W^2(\partial_x q)^2 \right] dV, \quad (3.72)$$

as can be seen from Eqs. (3.29), (3.33) and (3.34). With the equilibrium solution given in Eq. (3.69), this leads to

$$\begin{aligned}
 \gamma(\theta) &= \int_{-\infty}^{\infty} 3 [q(x)^2 - 2q(x)^3 + q(x)^4] dx \\
 &= \frac{3}{16} \int_{-\infty}^{\infty} [1 - 2 \tanh^2(x/\xi(\theta)) + \tanh^4(x/\xi(\theta))] dx \\
 &= \frac{3\xi(\theta)}{48} \left[\left(2 + \frac{1}{\cosh^2(x/\xi(\theta))} \right) \tanh(x/\xi(\theta)) \right]_{-\infty}^{\infty} \\
 &= \frac{1}{4} \xi(\theta).
 \end{aligned}$$

Using the interface thickness, given in Eq. (3.70), and generalizing to an arbitrary interface, whose normal has an angle Θ to the x -axis, one obtains

$$\gamma(\theta - \Theta) = \frac{1}{4} \sqrt{2c_1 + \frac{c_2}{2} \left[\frac{5}{3} + \cos[2(\theta - \Theta)] \right]}. \quad (3.73)$$

The surface energy can be written as $\gamma(\theta - \Theta) = \gamma_0 a(\theta - \Theta)$ with the average surface energy $\gamma_0 = \frac{1}{2} [\gamma(0) + \gamma(\pi/2)]$. The function containing the angle dependence can be expressed as $a(\theta) = 1 + \epsilon \tilde{a}(\theta)$, where $\epsilon = \frac{\gamma(0) - \gamma(\pi/2)}{\gamma(0) + \gamma(\pi/2)}$ is a measure of the anisotropy.

3.3.3 Capillary length and kinetic coefficient

Besides the interface thickness and the surface energy, two other material properties can be expressed in terms of model parameters, the capillary length and the kinetic coefficient. In this one-dimensional notation with constant nematic orientation θ and an interface with $\Theta = 0$, the derivation of section 2.3.1 can be used, adjusting the coupling functions to the ones used in this chapter.

The capillary lengths for constant θ is given in Eq. (2.39) as

$$d_0^{\theta=\text{const}} = a_1 \frac{W(\theta)}{\lambda} = \frac{W(\theta)}{3\sqrt{2}\lambda}$$

and the kinetic coefficient in Eq. (2.40)

$$\beta = a_1 \left[\frac{\tau(\theta)}{\lambda W(\theta)} - a_2 \frac{W(\theta)}{D} \right],$$

where here $a_1 = I/J = \frac{1}{3\sqrt{2}}$ and $a_2 = (\mathcal{K} + JF)/I = 5/2$. The integrals $I = 1/(3\sqrt{2})$, $J = 1$, $F = (\ln 2)/\sqrt{2}$ and $\mathcal{K} = (5 - \ln 64)/(6\sqrt{2})$ are defined in in Eqs. (2.41) to (2.44), where here $\phi_0 = \frac{1}{2}[1 - \tanh(x/\sqrt{2})]$ and $g^0 = 3\phi_0^2 - 2\phi_0^3$.

For $\lambda = \frac{D\tau_0}{W_0^2} \frac{1}{a_2}$, the kinetic coefficient vanishes in the isotropic case — this is the configuration chosen for all simulations in this work. In general, there are two more corrections to the interface kinetics. The first one arises from the fact that W depends on Θ and θ and therefore is not constant in the entire system. This can in principle be avoided by having a τ which varies with Θ and θ accordingly. For the liquid crystals, however, there is a second contribution which arises from the deformation in the bulk and the resulting strain. These effects, however, should be rather small for a weakly perturbed planar interface.

3.4 Sharp interface limit

In this section, an analytical expression for the stability of modes which perturb the equilibrium solution is obtained. The dispersion relation ω_k gives the growth rate ω as a function of perturbation wave vector k and can be compared with the numerical results obtained from the model described in section 3.2.

The analytical calculation is made in the so-called sharp interface limit where the width of the diffuse interface region tends to zero, compare section 2.2.

The dispersion relation is obtained by relating the chemical potential at the interface to the pressure difference, using the Gibbs-Thomson relation

$$[\mu - \mu_{\text{Eq}}]_{\text{interface}} = \frac{\Delta p}{\Delta c}. \quad (3.74)$$

To obtain an expression for the pressure, the energy in the sharp interface limit

$$\mathcal{F}_{\text{SI}} = \mathcal{F}_{\text{bulk}} + \mathcal{F}_{\text{interface}} + \mathcal{F}_{\text{elastic}} \quad (3.75)$$

is written as the sum of bulk, interface and elastic contribution and expressed in terms of the interface position ζ . Varying the interface position leads to a change in pressure, coming from the bulk energy [61]

$$\frac{\delta \mathcal{F}_{\text{bulk}}}{\delta \zeta} = h \Delta p, \quad (3.76)$$

where h is the sample thickness. This term has to be canceled out by contributions from the elastic energy and the interface energy, since the total variation has to be zero at equilibrium

$$\frac{\delta \mathcal{F}_{\text{SI}}}{\delta \zeta} = 0. \quad (3.77)$$

$\mathcal{F}_{\text{interface}}$ and $\mathcal{F}_{\text{elastic}}$ can be obtained from the free energy \mathcal{F}_0 as given in Eq. (3.23) but in terms of q and θ , which corresponds to the sum of Eqs. (3.29), (3.33) and (3.34). For a nematic bulk system with constant $q = 1$ but varying orientation angle θ , the elastic energy can be written as

$$\mathcal{F}_{\text{elastic}} = \int \frac{1}{2} W_B^2 |\nabla \theta|^2 dV, \quad (3.78)$$

with bulk gradient constant $W_B^2 = \frac{9}{2}(c_1 + \frac{1}{2}c_2)$.

The interface energy is given by [61]

$$\mathcal{F}_{\text{interface}} = \int \gamma(\theta(I) - \Theta) \delta(\zeta) dV, \quad (3.79)$$

where $\delta(\zeta)$ is the Dirac-Delta function and with the surface energy as given in Eq. (3.73).

Since $\mathcal{F}_{\text{interface}}$ and $\mathcal{F}_{\text{elastic}}$ depend on the orientation of the liquid crystal, an expression for $\theta(x, y)$ has to be obtained first.

For a director orientation which relaxes with a rotational viscosity γ_1 , the equation of motion can be written as

$$\gamma_1 \partial_t \theta = - \frac{\delta \mathcal{F}}{\delta \theta}. \quad (3.80)$$

Furthermore, $\theta(x, y)$ can be developed in first order perturbation around the planar interface, allowing a small sinusoidal perturbation.

In zeroth order, to solve the equation of motion, $\theta_0(x)$ has to depend linearly on x and is hence of the form

$$\theta_0(x) = \mathcal{A}x, \quad (3.81)$$

for which an explicit expression is obtained in section 3.4.1. This approach is also taken to obtain a limiting condition at the interface, relating the orientation to the relation between bulk and interface energy.

In first order perturbation, as ansatz a correction which decays exponentially in x direction away from the interface with the inverse decay length K is taken. The perturbation is sinusoidal in y direction, with a wave vector k and grows or decays exponentially with the time t , depending on the sign of the growth rate ω . The angle, as function of x and y , can then be written as

$$\theta(x, y) = \theta_0(x) + \varepsilon\theta_1 \exp(Kx + \omega t +iky), \quad (3.82)$$

where ε is a small parameter and where θ_1 gives the amplitude of the first order correction. The unknown coefficients are obtained in section 3.4.2 by inserting this ansatz in the equation of motion and using the interface condition.

In section 3.4.3, the explicit forms of $\mathcal{F}_{\text{interface}}$ and $\mathcal{F}_{\text{elastic}}$ are obtained, leading to the Laplace Equation for Δp , which is used to finish the calculations of the dispersion relation in section 3.4.4.

3.4.1 Planar interface

Instead of using the crude approximation that the nematic is always orientated perpendicular to the surface as preferred by the surface energy [61], one can consider an interplay between surface energy and bulk energies.

Caused by the anisotropy in the surface energy, the liquid crystal prefers a certain orientation at the interface, minimizing its energy there. Since the orientation far away in the bulk, however, is fixed at a different orientation, a reorientation at the interface leads to an increase in the bulk energy caused by the nematic deformation. There are two limiting cases. If the surface energy is much larger than the energy cost of the deformation in the bulk, the nematic aligns in the direction as preferred by the surface energy at the interface, regardless of the bulk deformation. In the opposite case, for a very small surface energy and a large bulk energy, the nematic does not change its orientation in the bulk and lives with a higher energy at the interface. In general, a compromise between these two limiting cases is found, for which an analytic expression is obtained here.

Elastic contribution in the bulk

Searching for a stationary solution of Eq. (3.80) with the elastic energy from Eq. (3.78), one obtains

$$\gamma_1 \partial_t \theta = W_B^2 \partial_{xx} \theta = 0,$$

which gives with Eq. (3.81) $\mathcal{A} = \frac{\theta_0(L) - \theta_0(-x_I)}{x_I} = \partial_x \theta_0$, the difference between the orientation at the interface and at the distance x_I from the interface, as

shown in figure 3.4. For the elastic energy, it then follows

$$\mathcal{F}_{\text{elastic}} = \int \frac{1}{2} W_B^2 \left(\frac{\theta_0(I) - \theta_0(-x_I)}{x_I} \right)^2 dV. \quad (3.83)$$

Contribution of the interface

The total free energy can be calculated by the sum of the elastic energy and the interface energy, given in Eq. (3.83) and Eq. (3.79) respectively, to

$$\mathcal{F} = \frac{1}{2} W_B^2 \frac{[\theta_0(I) - \theta_0(-x_I)]^2}{x_I} + \gamma(\theta_0).$$

Being interested in the optimal interface angle $\theta_0(I)$ which minimizes the free energy, one takes the derivative of \mathcal{F} with respect to $\theta_0(I)$ and searches for its root

$$\frac{\partial \mathcal{F}}{\partial \theta_0(I)} = W_B^2 \frac{\theta_0(I) - \theta_0(-x_I)}{x_I} + \gamma'(\theta_0(I)) = 0.$$

The derivative of the interface energy is given by

$$\begin{aligned} \gamma'(\theta) &= \frac{\partial \gamma}{\partial \theta} = -\frac{1}{8} \frac{c_2 \sin[2(\theta)]}{\sqrt{2c_1 + \frac{c_2}{2} \left[\frac{5}{3} + \cos[2(\theta)] \right]}} \\ &\approx \gamma'_0 \sin[2(\theta)], \end{aligned}$$

where

$$\gamma'_0 = -\frac{1}{8} \frac{c_2}{\sqrt{2c_1 + \frac{c_2}{2} \left[\frac{5}{3} + \cos[2\theta_0(I)] \right]}}. \quad (3.84)$$

The interface angle appears in γ'_0 , but in the approximation of small angle variations of the perfect alignment at the interface, $\theta_0(I) \approx 0$ and $\gamma'_0 \approx -\frac{1}{8} \frac{c_2}{\sqrt{2c_1 + \frac{4}{3}c_2}}$.

The condition for an extremum can then be written as

$$\frac{W_B^2}{\gamma'_0} \partial_x \theta|_I = -\sin[2(\theta_0(I) - \Theta)], \quad (3.85)$$

which is the desired anchoring condition.

There are two possible solutions, one for $\theta_0(I) - \Theta \approx 0$ and one for $\theta_0(I) - \Theta \approx \pi/2$, which belong to a minimum in the free energy for $c_2 < 0$ and $c_2 > 0$, respectively. For the first case, a nontrivial solution only exists for $\frac{W_B^2}{x_I \gamma'_0} < 2$.

3.4.2 Perturbation of the planar interface

A small sinusoid perturbation of the interface is introduced, using the ansatz given in Eq. (3.82).

To obtain an expression for the inverse decay length, the equation of motion for the orientation angle, as given in Eq. (3.80) in the moving frame of reference, is considered [61]

$$\frac{\partial \theta}{\partial t} = \frac{W_B^2}{\gamma_1} \nabla^2 \theta + v \frac{\partial \theta}{\partial x}. \quad (3.86)$$

Rewriting the zeroth order solution in the moving frame of reference $\theta_0(x) = \theta_0(I) + \mathcal{A}(x + vt)$ and inserting the ansatz from Eq. (3.82) in the equation of motion, Eq. (3.86), one obtains

$$\begin{aligned} \mathcal{A}v &+ \omega\varepsilon\theta_1 \exp(iky + \omega t + Kx) \\ &= \frac{W_B^2}{\gamma_1} (K^2 - k^2)\varepsilon\theta_1 \exp(iky + \omega t + Kx) \\ &+ \mathcal{A}v + \mathcal{A}K\varepsilon\theta_1 \exp(iky + \omega t + Kx). \end{aligned}$$

Solving for K gives

$$K(k, \omega) = -\frac{v\gamma_1}{2W_B^2} \pm \sqrt{\left(\frac{v\gamma_1}{2W_B^2}\right)^2 + k^2 + \omega\frac{\gamma_1}{W_B^2}}, \quad (3.87)$$

which relates the decay rate in x direction K to the wavelength k of the perturbation and the growth rate ω . Note that it also depends on the pulling velocity v .

Amplitude

Having a relation between the inverse decay length K and k and ω , one still needs an expression for the amplitude θ_1 . In the following, the ansatz for θ , given in Eq. (3.82), is developed around the interface position. It is inserted in the anchoring condition, which was derived in section 3.4.1 for the orientation at the interface.

The anchoring condition can be written in an approximation for small angle differences $\theta|_I - \Theta \ll 1$ as

$$\partial_x \theta|_I \simeq -\frac{2\gamma'_0}{W_B^2} (\theta|_I - \Theta). \quad (3.88)$$

To develop the ansatz for θ around the interface position, one firstly introduces the interface position $\zeta = \varepsilon\zeta_1 \exp(iky + \omega t)$ as a perturbation of the planar interface, where $\zeta = 0$. Going to first order in ε , the orientation at the interface can be written as

$$\begin{aligned} \theta|_I &= \theta_0(\zeta) + \varepsilon\theta_1 \exp(iky + \omega t + Kx) \\ &= \theta_0(0) + \varepsilon \left(\frac{\partial\theta_0}{\partial x} \Big|_{x=0} \zeta_1 + \theta_1 \right) \exp(iky + \omega t). \end{aligned}$$

The derivative with respect to x is then

$$\begin{aligned} \partial_x \theta|_I &= \partial_x \theta_0|_{x=0} + K\varepsilon\theta_1 \exp(iky + \omega t) \\ &= \mathcal{A} + K\varepsilon\theta_1 \exp(iky + \omega t) \end{aligned}$$

and the interface angle can be written as

$$\Theta = -\partial_y \zeta = -ik\varepsilon\zeta_1 \exp(iky + \omega t).$$

Inserting $\theta|_I$ and $\partial_x \theta|_I$ in Eq. (3.88), one obtains an equation for θ_1

$$\underbrace{\partial_x \theta|_I + K\varepsilon\theta_1 \exp(iky + \omega t)} = -\frac{2\gamma'_0}{W_B^2} \underbrace{[\theta_0(I) + \varepsilon(\mathcal{A}\zeta_1 + \theta_1 + ik\zeta_1) \exp(iky + \omega t)]},$$

where the underbraced terms fulfill the boundary condition for θ_0 and drop out. What remains is

$$K\theta_1 = -\frac{2\gamma'_0}{W_B^2} (\mathcal{A}\zeta_1 + \theta_1 + \imath k\zeta_1),$$

and therefore, solving for θ_1 ,

$$\theta_1 = -\frac{\mathcal{A}\zeta_1 + \imath k\zeta_1}{\frac{KW_B^2}{2\gamma'_0} + 1}. \quad (3.89)$$

To eliminate ζ_1 , one can rewrite the angle in terms of the surface slope $\partial_y\zeta$, and obtain an expression for $\theta(x, y)$ to first order

$$\begin{aligned} \theta(x, y) &= \theta_0(x) + \varepsilon\theta_1 \exp(\imath ky + Kx + \omega t) \\ &= \theta_0(x) - \varepsilon \frac{\mathcal{A}\zeta_1 + \imath k\zeta_1}{\frac{KW_B^2}{2\gamma'_0} + 1} \frac{1}{-\imath k\varepsilon\zeta_1} \partial_y\zeta \exp(Kx) \\ &= \theta_0(x) + \frac{1 - \imath \frac{\mathcal{A}}{k}}{\frac{KW_B^2}{2\gamma'_0} + 1} \partial_y\zeta \exp(Kx) \\ &= \theta_0(x) + \theta_A \partial_y\zeta \exp(Kx), \end{aligned} \quad (3.90)$$

with $\theta_A = \frac{1 - \imath \frac{\mathcal{A}}{k}}{\frac{KW_B^2}{2\gamma'_0} + 1}$. For small perturbations, the nematic aligns itself in such a

way that the angle is proportional to the interface slope, but the proportionally constant θ_A depends on surface and bulk properties and reflects the balance between the two energies.

3.4.3 Laplace equation

With the expression for the orientation of the liquid $\theta(x, y)$ and the interface position ζ in first order perturbation, one can continue with the calculation of the Laplace equation. The bulk free energy contribution is already given in Eq. (3.76), but the contributions of the elastic and the interface energies, given in Eqs. (3.78) and (3.79), are still missing.

Interface energy

With the anchoring condition $\theta|_I = \theta_A \partial_y\zeta$ and the interface orientation $\Theta = -\partial_y\zeta$, the surface energy can be written as a function of the interface position $\zeta(y)$ as

$$\gamma(\partial_y\zeta) = \frac{1}{4} \sqrt{2c_1 + \frac{c_2}{2} \left[\frac{5}{3} + \cos[2(\theta_A - 1)\partial_y\zeta] \right]}. \quad (3.91)$$

This leads to a contribution of the interface energy of

$$\begin{aligned} \frac{\delta \mathcal{F}_{\text{interface}}}{\delta \zeta} &= h \frac{\delta}{\delta \zeta} \int_{L_I} \gamma(\theta) ds \\ &= h \frac{\delta}{\delta \zeta} \int dy \gamma(\partial_y\zeta) \sqrt{1 + (\partial_y\zeta)^2}. \end{aligned}$$

$$\begin{aligned}
&= h \left\{ -\sqrt{1 + (\partial_y \zeta)^2} \partial_y \frac{\partial [\gamma(\partial_y \zeta)]}{\partial(\partial_y \zeta)} - \gamma \partial_y \frac{\partial \sqrt{1 + (\partial_y \zeta)^2}}{\partial(\partial_y \zeta)} \right\} \\
&= h \left\{ -\partial_y \left[\frac{\partial \gamma}{\partial(\partial_y \zeta)} \right] \sqrt{1 + (\partial_y \zeta)^2} - \underbrace{\gamma \partial_y \left[\frac{\partial(\sqrt{1 + (\partial_y \zeta)^2})}{\partial(\partial_y \zeta)} \right]}_{= -\gamma \frac{\partial_{yy} \zeta}{(1 + (\partial_y \zeta)^2)^{3/2}} = -\gamma \kappa} \right\}.
\end{aligned}$$

The derivative in the first term can be calculated to

$$\begin{aligned}
\partial_y \left[\frac{\partial \gamma}{\partial(\partial_y \zeta)} \right] &= \partial_y \left[-\frac{1}{8} \frac{c_2(\theta_A - 1) \sin[2(\theta_A - 1)\partial_y \zeta]}{\sqrt{2c_1 + \frac{c_2}{2} \left[\frac{5}{3} + \cos[2(\theta_A - 1)\partial_y \zeta] \right]}} \right] \\
&= -\frac{1}{4} \frac{c_2(\theta_A - 1)^2 \cos[2(\theta_A - 1)\partial_y \zeta] \partial_{yy} \zeta}{\sqrt{2c_1 + \frac{c_2}{2} \left[\frac{5}{3} + \cos[2(\theta_A - 1)\partial_y \zeta] \right]}} \\
&\quad + \frac{1}{16} \frac{c_2^2(\theta_A - 1)^2 \sin^2[2(\theta_A - 1)\partial_y \zeta] \partial_{yy} \zeta}{\left\{ 2c_1 + \frac{c_2}{2} \left[\frac{5}{3} + \cos[2(\theta_A - 1)\partial_y \zeta] \right] \right\}^{3/2}} \\
&= (\partial_{\theta\theta} \gamma)(\theta_A - 1)^2 \partial_{yy} \zeta.
\end{aligned}$$

Finally, the interface contribution is given by

$$\frac{\delta \mathcal{F}_{\text{interface}}}{\delta \zeta} \approx -h\kappa [\gamma + (\theta_A - 1)^2 \partial_{\theta\theta} \gamma]. \quad (3.92)$$

Without anisotropy ($\partial_{\theta\theta} \gamma = 0$) and without elastic energy, the usual Laplace equation $\Delta p = \kappa \gamma$ follows with Eq. (3.77). The anisotropy is treated in the following together with the elastic energy.

Elastic energy

In this work, the nematic orientation is allowed to change in the bulk to align with the surface. Therefore, the elastic energy caused by this deformation has to be considered as well, as given in Eq. (3.76) as

$$\begin{aligned}
\mathcal{F}_{\text{elastic}} &= \frac{W_B^2}{2} \int dy \int_{-x_I}^0 dx |\nabla \theta|^2 \\
&= \frac{W_B^2}{2} \int dy \int_{-x_I}^0 dx |\nabla [\theta_A \partial_y \zeta(y) e^{Kx}]|^2 \\
&= \frac{W_B^2}{2} \int dy \int_{-x_I}^0 dx |\theta_A|^2 \left[\frac{\partial}{\partial y} \partial_y \zeta(y) e^{Kx} + \partial_x (\partial_y \zeta(y) e^{Kx}) \right]^2 \\
&= \frac{W_B^2}{2} \theta_A^2 \int dy \int_{-x_I}^0 dx [\partial_{yy} \zeta + K \partial_y \zeta]^2 \exp(2Kx) \\
&= \frac{W_B^2}{2} \theta_A^2 [1 - e^{-2Kx_I}] \int dy \left\{ \frac{1}{2K} (\partial_{yy} \zeta)^2 + \frac{1}{2} K (\partial_y \zeta)^2 \right\} \\
&\quad + \text{boundary terms.}
\end{aligned}$$

Neglecting the boundary terms, the functional derivative yields

$$\begin{aligned}
\frac{\delta \mathcal{F}_{\text{elastic}}}{\delta \zeta} &= \frac{W_B^2}{2} \frac{\delta}{\delta \zeta} \int dx dy |\nabla \theta|^2 \\
&= \frac{W_B^2}{2} \theta_A^2 (1 - e^{-2Kx_I}) \left(\frac{1}{K} \frac{\partial^4 \zeta}{\partial y^4} - K \frac{\partial^2 \zeta}{\partial y^2} \right) \\
&\equiv \frac{1}{2} l_E^2 |\theta_A|^2 (1 - e^{-2Kx_I}) \left(\frac{1}{K} \frac{\partial^4 \zeta}{\partial y^4} - K \frac{\partial^2 \zeta}{\partial y^2} \right), \quad (3.93)
\end{aligned}$$

with

$$l_E^2(k, \omega) = W_B^2. \quad (3.94)$$

Laplace Equation

With this additional term for the elastic energy and with the anisotropy, the Laplace equation can be written as

$$\Delta p = [\gamma + (1 - \theta_A)^2 \partial_{\theta\theta} \gamma] \kappa - \frac{1}{2} l_E^2 |\theta_A|^2 (1 - e^{-2Kx_I}) \left(\frac{1}{K} \frac{\partial^4 \zeta}{\partial y^4} - K \kappa \right).$$

3.4.4 Dispersion relation

The dispersion relation for an isotropic system without considering the elastic energy is derived e.g. by Langer [23] for a solid-liquid system, investigating the so-called Mullins-Sekerka instability of a planer surface, as explained in section 2.2.4. In the following, the basic steps of the analysis are performed for the directional solidification, giving the results for the two systems a) without and b) with anisotropy and elastic energy, respectively.

The Gibbs-Thomson relation is given as

$$\begin{aligned}
[\mu - \mu_{\text{Eq}}](\text{interface}) &= \frac{\Delta p}{\Delta c} \\
a) &= -\frac{\gamma \kappa}{\Delta c} \\
b) &= -\frac{1}{\Delta c} \left[(\gamma + (1 - \theta_A)^2 \partial_{\theta\theta} \gamma) \kappa - \frac{l_E^2 |\theta_A|^2 (1 - e^{-2Kx_I})}{2} \left(\frac{1}{K} \frac{\partial^4 \zeta}{\partial y^4} - K \kappa \right) \right].
\end{aligned}$$

Without elastic energy contributions, $\theta_A^2 = 0$ (perfect anchoring) so that equation b) reduced to Eq. (2.14). One can see that θ_A^2 represent the relation between the bulk and the interface contribution. For $\theta_A^2 = 0$, the contribution of the surface anisotropy is maximal, while the bulk contribution vanishes. For the opposite case, $\theta_A^2 = 1$, the surface contribution vanishes and the bulk deformation contributes maximally.

For the normalized concentration u , the interface condition can be written as

$$\begin{aligned}
u^{N/I}(\text{Interface}) &= \frac{[\mu - \mu_{\text{Eq}}]_{\text{Interface}}}{\Delta c \left. \frac{\partial \mu}{\partial c} \right|_{c_{\text{Eq}}^{N/I}}} - \frac{\zeta}{l_T^{N/I}} \quad (3.95) \\
a) &= -d_0 \kappa - \frac{\zeta}{l_T^{N/I}}
\end{aligned}$$

$$b) = -d_0 \left[(a(\theta) + (1 - \theta_A)^2 a''(\theta)) \kappa - \frac{1}{2} \frac{l_E^2 |\theta_A|^2 (1 - e^{-2Kx_I})}{\gamma_0} \left(\frac{1}{K} \frac{\partial^4 \zeta}{\partial y^4} - K \kappa \right) \right] - \frac{\zeta}{l_T^{N/I}},$$

compare Eqs. (2.16) and (2.15). The capillary length is given in section 2.2.4 as $d_0 = \frac{\gamma_0}{(\Delta c)^2 \frac{\partial \mu}{\partial c} \Big|_{c_{\text{Eq}}^{N/I}}}$.

There are two equations describing the time evolution of the system. The first one is the continuity equation

$$v_n = D \left[\tilde{\beta} (\nabla u)_N - (\nabla u)_I \right] \cdot \vec{n}, \quad (3.96)$$

with $\tilde{\beta} = (D^N c_p^N) / (D^I c_p^I)$ and as given in Eq. (2.19).

The second one is the diffusion equation in the both phases, as already given in Eqs. (2.17) and (2.18), here in the moving frame of reference

$$D^{N/I} \nabla^2 u^{N/I} + v \frac{\partial u^{N/I}}{\partial x} = \frac{\partial u^{N/I}}{\partial t}. \quad (3.97)$$

As ansatz, one can consider a small sinusoidal perturbation around a flat interface [23]

$$\begin{aligned} \zeta(y, t) &\simeq \varepsilon \zeta_1 \exp(iky + \omega_k t) \\ u^I &\simeq \exp\left(-\frac{2x}{l}\right) - 1 + \varepsilon u_1^I \exp(-\alpha^I x +iky + \omega_k t) \\ u^N &\simeq \varepsilon u_1^N \exp(\alpha^N x +iky + \omega_k t), \end{aligned}$$

with ζ interface position and $u^{I/N}$ normalized concentration in isotropic and nematic phase respectively.

Inserting this ansatz in diffusion equation Eq. (3.97), one obtains

$$\begin{aligned} D^I \left(-k^2 + (\alpha^I)^2 - \frac{2}{l^I} \alpha^I \right) &= \omega_k \\ D^N \left(-k^2 + (\alpha^N)^2 + \frac{2}{l^I} \alpha^I \right) &= \omega_k, \end{aligned}$$

where $l^{N/I} = \frac{2D^{N/I}}{v}$.

Solving for $\alpha^{N/I}$ leads to the inverse decay lengths α^I and α^N , given as

$$\begin{aligned} \alpha^I &= \frac{1}{l^I} + \sqrt{\frac{1}{(l^I)^2} + k^2 + \frac{\omega_k}{D^I}} \\ \alpha^N &= -\frac{1}{l^N} + \sqrt{\frac{1}{(l^N)^2} + k^2 + \frac{\omega_k}{D^N}}. \end{aligned}$$

To obtain the amplitudes, one inserts the ansatz in Eq. (3.95). One has to take care to use the values at the actual boundary $\zeta(y, t)$ (see for example Kassner [69]) $u(\zeta(y), y, t) = u_0(0) + \partial_x u_0(0) \zeta + u_1(0)$, leading to

$$\begin{aligned} u^I(\text{Interface}) &= \varepsilon \left(u_1^I - \frac{2}{l^I} \zeta_1 \right) \exp(iky + \omega_k t) \\ u^N(\text{Interface}) &= \varepsilon u_1^N \exp(iky + \omega_k t). \end{aligned}$$

In the case a), one obtains with the interface condition

$$u^I(\text{Interface}) = u^N(\text{Interface}) = d_0 \partial_{yy} \zeta - \frac{1}{l_T^{N/I}} \zeta,$$

where $\kappa = -\partial_{yy} \zeta$.

For the amplitudes, it follows $-\frac{2}{l^I} \zeta_1 + u_1^I = u_1^N = \left(-d_0 k^2 - \frac{1}{l_T^{N/I}}\right) \zeta_1$, or

$$\begin{aligned} u_1^I &= \left(\frac{2}{l^I} - d_0 k^2 - \frac{1}{l_T^{N/I}} \right) \zeta_1 \\ u_1^N &= \left(-d_0 k^2 - \frac{1}{l_T^{N/I}} \right) \zeta_1. \end{aligned}$$

For b), one obtains

$$\begin{aligned} u_1^I &= \left\{ \frac{2}{l^I} - d_0 [(a(\theta) + (1 - \theta_A)^2 a''(\theta)) k^2 \right. \\ &\quad \left. + \frac{1}{2} \frac{l_E^2 |\theta_A|^2 (1 - e^{-2Kx_I})}{\gamma_0} \left(\frac{k^4}{K} + K k^2 \right) \right] - \frac{1}{l_T^{N/I}} \right\} \zeta_1 \\ u_1^N &= \left\{ -d_0 [(a(\theta) + (1 - \theta_A)^2 a''(\theta)) k^2 \right. \\ &\quad \left. + \frac{1}{2} \frac{l_E^2 |\theta_A|^2 (1 - e^{-2Kx_I})}{\gamma_0} \left(\frac{k^4}{K} + K k^2 \right) \right] - \frac{1}{l_T^{N/I}} \right\} \zeta_1. \end{aligned}$$

In this linear approximation, the continuity equation can be written as

$$(v + \dot{\zeta}) = D \left[\tilde{\beta} \partial_x u^N|_{\text{interface}} - \partial_x u^I|_{\text{interface}} \right],$$

since $\vec{n} \simeq (1, 0, 0)$. The derivatives at the interface are given by

$$\begin{aligned} \partial_x u^N|_{\text{interface}} &= \varepsilon u_1^N \alpha^N \exp(iky + \omega_k t) \\ \partial_x u^I|_{\text{interface}} &= -\frac{2}{l^I} + \varepsilon \left(\frac{4}{(l^I)^2} \zeta_1 - u_1^I \alpha^I \right) \exp(iky + \omega_k t). \end{aligned}$$

In accordance with the phase-field model, all physical constants are taken to be equal in the nematic and in the isotropic phase ($D^N = D^I = D$, $l^N = l^I = l$, $\tilde{\beta} = 1$ and $l_T^N = l_T^I = l_T$). It then follows

$$\begin{aligned} v + \varepsilon \zeta_1 \omega_k e^{iky + \omega_k t} &= D \left[\alpha^N \varepsilon u_1^N e^{iky + \omega_k t} + \frac{2}{l} \right. \\ &\quad \left. + \varepsilon \left(u_1^I \alpha^I - \frac{4}{l^2} \zeta_1 \right) e^{iky + \omega_k t} \right] \\ \zeta_1 \omega_k &= D (\alpha^N u_1^N + \alpha^I u_1^I) - \frac{2v}{l} \zeta_1. \end{aligned}$$

Using the relation between the amplitudes, one obtains for a)

$$\omega_k = v \left(\alpha^I - \frac{2}{l} \right) - D d_0 k^2 (\alpha^I + \alpha^N) - \frac{D(\alpha^I + \alpha^N)}{l_T},$$

and for b)

$$\begin{aligned}\omega_k &= v \left(\alpha^I - \frac{2}{l} \right) - Dd_0k^2 [a(\theta) + (1 - \theta_A)^2 a''(\theta) \\ &\quad + \frac{1}{2} \frac{l_E^2 |\theta_A|^2 (1 - e^{-2Kx_I})}{\gamma_0} \left(\frac{k^2}{K} + K \right)] (\alpha^N + \alpha^I) - \frac{D}{l_T} (\alpha^N + \alpha^I).\end{aligned}$$

For a), this leads to the dispersion relation when inserting the expressions for $\alpha^{N/I}$

$$\begin{aligned}\omega_k &= v \left(\frac{1}{l} + \sqrt{\frac{1^2}{l} + k^2 + \frac{\omega_k}{D}} - \frac{2}{l} \right) \\ &\quad - 2D \sqrt{\frac{1^2}{l} + k^2 + \frac{\omega_k}{D}} d_0k^2 - \frac{2D}{l_T} \sqrt{\frac{1^2}{l} + k^2 + \frac{\omega_k}{D}} \\ &= -\frac{v^2}{2D} + \left(\frac{v^2}{2D} - \frac{v}{l_T} - vd_0k^2 \right) \sqrt{1 + \frac{4D^2k^2}{v^2} + \frac{4D\omega_k}{v^2}},\end{aligned}$$

which is solved by

$$\omega_k = \frac{v^2}{2D} (A - 1) + \sqrt{\frac{v^4}{4D^2} A(A - 1) + v^2 k^2 A}, \quad (3.98)$$

with $A(k) = \left(1 - \frac{2Dd_0}{v} k^2 - \frac{2D}{l_T v} \right)^2$.

For the case b) with elasticity and anisotropy, the dispersion relation is given by

$$\begin{aligned}\omega_k &= -\frac{v^2}{2D} + \left\{ \frac{v^2}{2D} - \frac{v}{l_T} - vd_0k^2 [a(\theta) + (1 - \theta_A)^2 a''(\theta) \right. \\ &\quad \left. + \frac{1}{2} \frac{l_E^2 |\theta_A|^2 (1 - e^{-2Kx_I})}{\gamma_0} \left(\frac{k^2}{K} + K \right)] \right\} \sqrt{1 + \frac{4D^2k^2}{v^2} + \frac{4D\omega_k}{v^2}},\end{aligned} \quad (3.99)$$

where K is still a function of k and ω and given by Eq. (3.87) as

$$K(k, \omega) = -\frac{v\gamma_1}{2W_B^2} \pm \sqrt{\left(\frac{v\gamma_1}{2W_B^2} \right)^2 + k^2 + \omega \frac{\gamma_1}{W_B^2}}.$$

To obtain the dispersion relation for an anisotropic system, Eq. (3.99) has to be solved numerically. This is performed using a fail-safe routine that uses a combination of bisection and Newton-Raphson method [70].

3.5 Numerical results

3.5.1 Physical lengths and model parameters

To see whether the model is capable of describing real systems, it is necessary to identify the model parameters with physical values. The physical important

values are lengths, namely the thermal length (l_T), which appears directly in the model,

$$\begin{aligned} \text{the diffusion length} & \quad l = \frac{2D}{v}, \\ \text{the capillary length} & \quad d_0 = \frac{2}{3\lambda}\gamma_0 \\ \text{and the elastic length} & \quad l_E = \sqrt{\frac{W_B^2 d_0}{\gamma_0}} = \sqrt{\frac{2}{3\lambda}}W_B. \end{aligned}$$

The model parameters are D diffusion constant, v pulling speed, λ coupling parameter and $\gamma_0 = \frac{1}{2}[\gamma(0) + \gamma(\pi/2)] = \frac{1}{8}\left(\sqrt{2c_1 + \frac{4}{3}c_2} + \sqrt{2c_1 + \frac{1}{3}c_2}\right)$ mean value of the anisotropic surface energy, $W_B = \sqrt{(9/2)(c_1 + c_2/2)}$, both a combination of the gradient constants c_1 and c_2 .

One can see that for a given anisotropy (combination of c_1 and c_2), l_E and d_0 cannot be chosen independently of each other. Furthermore, they scale differently with the coupling constant λ ($l_E/d_0 \propto \lambda^{3/2}$), which is used to artificially increase the interface thickness in order to decrease the necessary resolution and gain calculation time.

To be able to compare the model parameters with a real system, not the absolute values are important, but the relations between the lengths. For the values used in the simulations presented in this work ($\lambda = 0.4$, $v = 0.08$, $D = 1$, $l_T = 300$, $\gamma_0 \approx 0.5$, $W_B \approx 2.7$), the relative length scales can be calculated to $l/l_T \approx 0.08$, $d_0/l_T \approx 0.003$ and $l_E/l_T \approx 0.015$.

As one example for a real system, the values from 8CB are given (taken from [61], similar in [71]) in Tab. 3.1. It then follows

$$\begin{aligned} l_T &= \frac{\Delta T}{G} = 4.88 \times 10^{-3} \text{ cm} \\ l &= \frac{2D}{v} = 1.34 \times 10^{-3} \text{ cm} \\ d_0 &= \frac{\gamma}{L} \frac{T_0}{\Delta T} = 8.83 \times 10^{-7} \text{ cm} \\ l_E &= \sqrt{\frac{K}{L} \frac{T_0}{\Delta T}} = 9.64 \times 10^{-6} \text{ cm}. \end{aligned}$$

The relative length ratios can then be calculated to $l/l_T \approx 0.27$, $d_0/l_T \approx 1.8 \times 10^{-4}$ and $l_E/l_T \approx 0.002$.

Comparing the model parameters with this example for a real liquid crystal, one finds that the relative elastic lengths differs by a factor of 7.5, which is however not too bad, especially since the elastic lengths are experimentally not very accurately measured. The relative diffusion lengths is by a factor 3 too small, at the same time as the capillarity length is by a factor of 15 too large. The model system does therefore not agree perfectly with a real liquid crystal system, but is sufficiently close to be able to draw qualitative conclusions from the results.

3.5.2 Dispersion relation

Using the model developed in section 3.2, the directional solidification of a liquid crystal alloy can be simulated by solving the evolution equations for the fields, which are given by the concentration u and the two degrees of freedom

Latent heat L	2.05×10^7 erg/cm ³
Undercooling ΔT	0.21 K
Diffusion constant D	6.7×10^{-7} cm ² /sec
Surface energy γ	0.95×10^{-2} erg/cm ²
Temperature gradient G	43K/cm
Frank elastic constant K	$\approx 10^{-6}$ dyn
Equilibrium temperature T_0	400 K
Pulling velocity v	10^{-3} cm/sec

Table 3.1: Typical values for an 8CB liquid crystal as given by Bechhoefer and Langer [61].

of the nematic \hat{Q} , here expressed in the magnitude of order q and the nematic orientation θ . In figure 3.5, the initial and the final value of the different fields are shown as a function of their position x and y .

To compare the model with the theory, one can examine the dispersion relation for a fixed pulling velocity. Using the equations of motion obtained for the directional growth of the nematic phase of the liquid crystal, one can calculate the time evolution of a cell according to the model. To test the stability of the planar interface, one applies a small sinusoidal perturbation to the interface and investigates its evolution. As described in section 3.4, the perturbation is expected to grow or decay exponentially with a growth rate ω_k .

Analyzing the interface shape for its Fourier modes, the different growth rates ω_k for different perturbation wave numbers k can be obtained. For a system with strong anisotropy ($c_1 = 3$ and $c_2 = -3$) and where the first mode is given by $k\zeta = 0.079$, the amplitudes for the modes $k\zeta$ to $8k\zeta$ are shown in figure 3.6. For small times, the first mode dominates and it grows exponentially, as predicted by the theory, note the logarithmic scale.

The value of ω_k can be obtained by a linear fit of the curve. At larger times, the other modes become important and the system approaches a stationary shape, which is shown in figure 3.7. Here, the orientation in the nematic phase changes in the bulk, tending to align perpendicular to the interface. The actual nematic orientation at the interface is not perpendicular to the interface, which would be the case for the strong anchoring condition. This is in good agreement with the boundary condition assumed in this work.

Repeating the calculation for systems with different cell widths, one excites different modes k and the growth amplitudes ω_k can be obtained as a function of k . The comparison between this ω_k obtained numerically and the theoretical result, given as dispersion relation in Eq. (3.99), is shown in figure 3.8 for different anisotropies ϵ . The results obtained from the simulation, shown in open symbols, agree very well with the theory, shown in solid lines.

3.5.3 Cell structure depending on the orientation

To investigate the influence of the nematic orientation, a cell similar to the one in figure 3.7 is numerically simulated, with the difference that now the liquid crystal far in the bulk is not orientated perpendicular to the unperturbed interface. This symmetry breaking prevents a stable cell from forming and leads to a shape

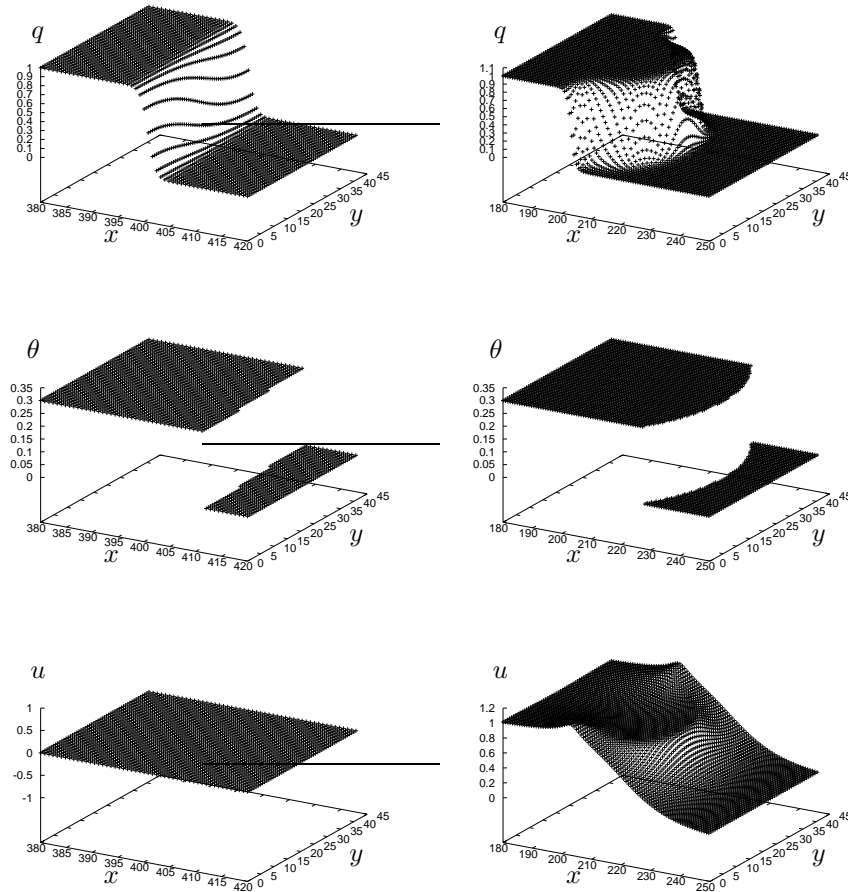


Figure 3.5: In this figure, the initial (left) and the final state (right) of a system without anisotropy and constant angle ($\theta = 0.3$) is shown. The interface is initially perturbed which causes the final stationary cell to build up. The fields shown, from top to bottom: magnitude of order q , orientation angle θ and normalized chemical potential u .

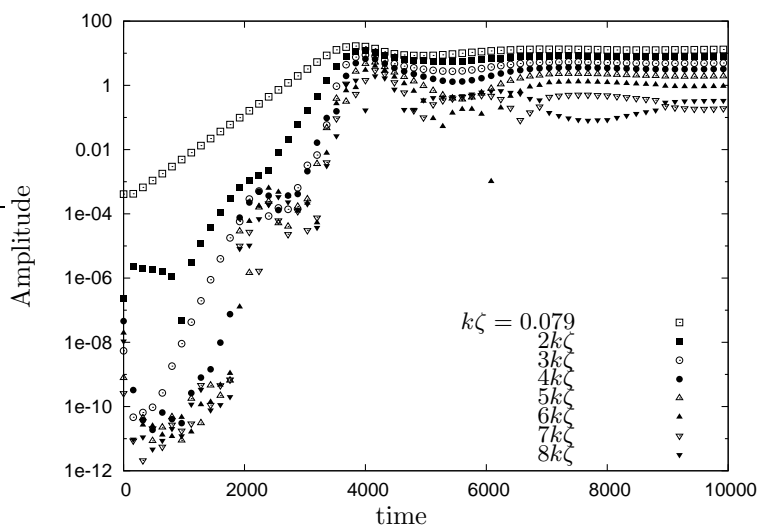


Figure 3.6: The time evolution of the interface modes, obtained by a Fourier analysis of the interface. Shown in a semi-logarithmic plot, so that the growth rates ω_k of the different modes k can be obtained from the slope of the curves for small times. One can see that the first mode with $k\zeta = 0.079$ dominates, until the system reaches its stationary shape.

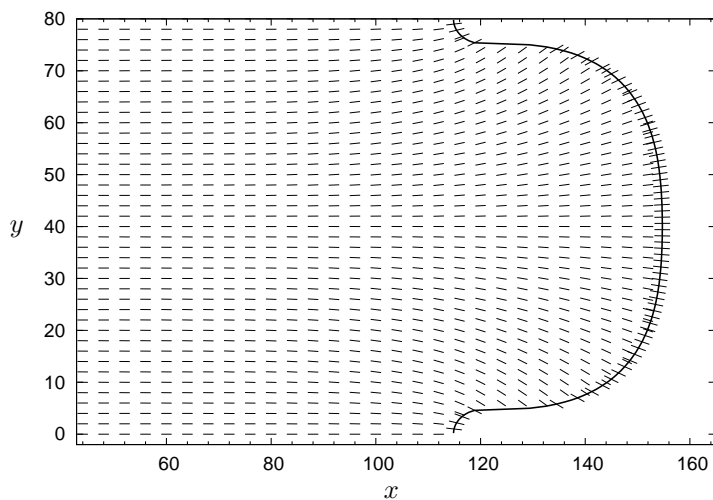


Figure 3.7: The steady-state cell shape. At the interface (thick solid line), the interface normal is shown (dashed lines) as well as the actual nematic orientation (solid lines). In the bulk, the nematic deforms and finds a compromise between bulk deformation and perpendicular interface orientation.

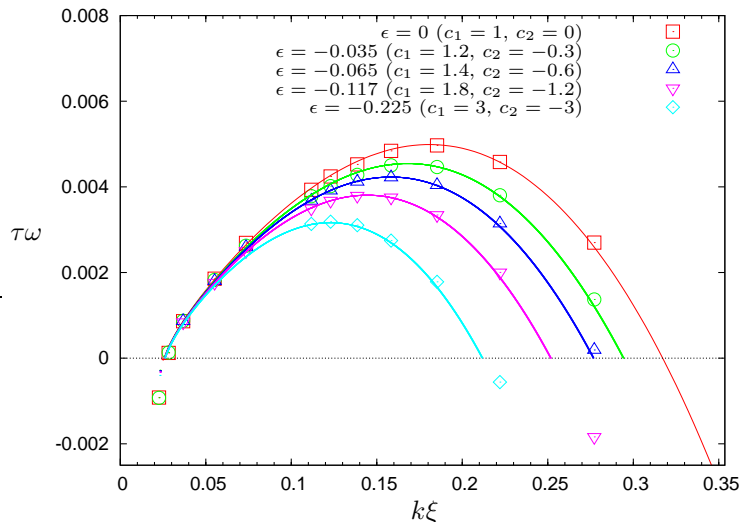


Figure 3.8: Dispersion relation for different anisotropies ϵ . The results from the simulation are shown with open symbols, the lines represent theory as given in Eq. (3.99). As one can see, the results agree well for all anisotropies investigated.

which varies with time. This is shown in a time series in figure 3.9. The nematic isotropic interface is shown with the thick solid line, the nematic orientation in the interface and the bulk with solid lines and the colored background indicates the impurity concentration c , going from 0.2 (white) to -1.0 (black).

3.5.4 Conclusion and outlook

In this chapter, the standard phase-field model has been generalized using a tensorial order parameter to include the nematic orientation of a liquid crystal. To validate this model, planar nematic-isotropic interfaces in a directional solidification setup has been perturbed and the stability was tested for systems with different anisotropies of the surface energy. The numerical results were compared with the theory obtained by generalizing a stability analysis based on the sharp interface limit. The results are in very good agreement with the theoretical description. Finally, the influence of the nematic orientation in the bulk has been investigated. It was shown that it can affect the symmetry of the entire system and plays an important role in the pattern forming process.

This model, however, does not allow to artificially increase the interface width in the same way as in phase-field models with a simple scalar phase field, since the additional length scale introduced by the elasticity is coupled to the capillary length. To circumvent this problem, it might be useful to introduce an additional scalar phase-field variable, which is then coupled to the tensorial order parameter. With this additional coupling constant, it should be possible to vary the elastic length and the capillarity length independently and therefore rescale the interface width to access larger systems with physical parameters. However, the parameters accessible with this model are similar enough to the

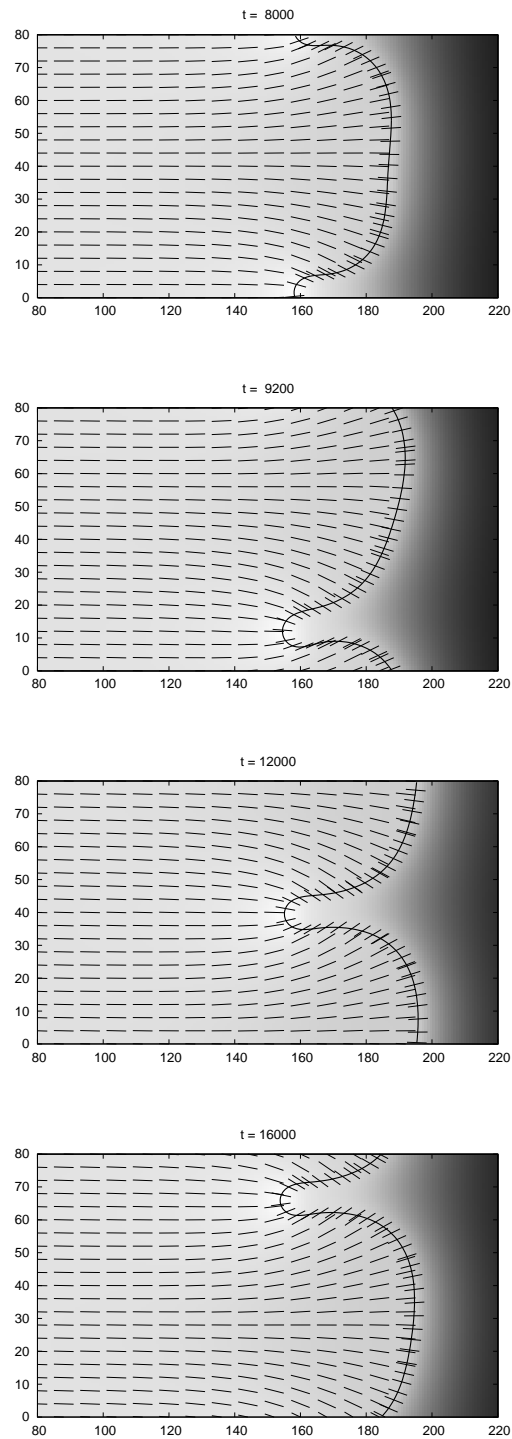


Figure 3.9: Time series of a cell of a liquid crystal whose nematic orientation is asymmetric at the start. One can see that instead of forming an stationary cell, the shape varies with time. The colored background indicates the impurity concentration c , going from 0.2 (white) to -1.0 (black).

ones of real liquid crystals to draw qualitative conclusions from the simulation results.

Chapter 4

Grain Boundary Structure in the Phase Field Crystal Model

In this chapter, the main interest is focused on the structure of grain boundaries. To investigate the role of topological defects and dislocations at the grain boundary, a phase field crystal model [72, 73] is used. This model has proven to be a successful extension of the phase-field model approach. Instead of having a uniform solution, its equilibrium configuration is periodic in space, corresponding to the atomic density field. Effects which are caused by the crystalline structure and its symmetries are automatically incorporated, including elastic and anisotropic properties. Also dislocations, vacancies as well as other topological defects appear naturally. Since the underlying field is a time-average density field, the phase field crystal method is able to represent the evolution over time scales which are larger than vibration modes (order of 10^{-15} s) but much shorter than diffusive processes in the system such as the viscous glide of dislocations, which are typically of the order of 10^{-6} seconds. The model is thus able to capture time scales that govern diffusive processes during phase transitions in pure materials [73–75] and alloys [76].

This chapter is organized as follows. The phase field crystal model is presented in section 4.1, while in section 4.2 the details of the numerical implementation are given. In section 4.3, the results are presented, with an emphasis on three aspects: on the local order in the interfaces, on the grain boundary properties and on the stability of liquid films between two solid grains. In section 4.4, a short conclusion is drawn and an outlook is given.

4.1 Phase field crystal model

To investigate the properties of grain boundaries numerically, in this work a phase field crystal model [72, 73] is used. To describe the crystalline structure, a conserved field ϕ is introduced, which represents the time averaged local atomic density. In the solid, the atoms vibrate around their fixed positions in the lattice, which leads to high values of ϕ at the lattice sites and low values in between. In the liquid, the atoms are distributed equally, leading to a constant ϕ in the time average.

In the phase-field model, the solidification is controlled by the diffusion of heat, which is released as latent heat at the interface. In the phase field crystal model, the densities in the two phases are different so that the solidification is limited by the exchange of mass. Instead of the temperature, the chemical potential determines which phase is preferred and controls whether the solid grows or melts.

To use the phase field crystal model for solidification processes, a free energy is constructed which supports at least a constant and the periodic phase. Most generally, the free energy contains a potential term and two gradient terms of different order, which enter with opposite signs. In section 4.1.1, a possible choice of the free energy is presented.

From the free energy, it is possible to construct the corresponding phase diagram, as shown in section 4.1.2. The obtained phase diagram can be compared with the phase diagram of real physical systems and the region of best agreement can be chosen. In section 4.1.3, it is shown how the grain boundary energy can be obtained in the phase field crystal model. To be able to compare the results with theoretical descriptions of the grain boundaries, the elastic properties of the phase field crystal model are obtained and related to the physical

parameters.

4.1.1 Free energy and equation of motion

Most generally, the free energy giving rise to a constant and a periodic solution can be written as [73]

$$F = \int d\vec{r} \left[f(\phi) + \frac{\phi}{2} G(\nabla^2)\phi \right].$$

The exact form of $G(\nabla^2)$ can be determined for any pure material by the liquid-state structure factor [73], but in the simplest case can be assumed to be of the form $G(\nabla^2) = \lambda(q_0^2 + \nabla^2)^2$. To obtain the constants λ and q_0 , the form of $G(\nabla^2)$ can be fitted to the first-order peak of the structure factor.

The free energy can then be written as [73]

$$F = \int d\vec{r} \left\{ \frac{\phi}{2} [a\Delta T + \lambda(q_0^2 + \nabla^2)^2] \phi + u \frac{\phi^4}{4} \right\}, \quad (4.1)$$

where the nonlinear term ϕ^4 leads to a hexagonal pattern solution. To obtain a free energy which favors a different crystalline lattice structure, other non-linear terms can be used. So far, however, there is not a systematic method of deriving the nonlinear terms corresponding to a given crystalline structure [73].

The dynamics for the conserved field ϕ is given as

$$\frac{\partial \phi}{\partial \tau} = \Gamma \nabla^2 \frac{\delta F}{\delta \phi},$$

plus additional noise terms, which are neglected in this work. Γ is a phenomenological mobility coefficient.

It is convenient to non-dimensionalize the free energy and the equation of motion by using the dimensionless variables $\vec{x} = \vec{r}q_0$, $\psi = \phi \sqrt{\frac{u}{\lambda q_0^4}}$, $r = \frac{a\Delta T}{\lambda q_0^4}$ and $t = \Gamma \lambda q_0^6 \tau$. The free energy then becomes in two dimensions $\mathcal{F} = \frac{F}{\lambda^2 q_0^6 / u}$

$$\begin{aligned} \mathcal{F} &= \int d\vec{x} \left\{ \frac{\psi}{2} [r + (1 + \nabla^2)^2] \psi + \frac{1}{4} \psi^4 \right\} \\ &= \int dV \left\{ \frac{1}{2} \psi [(r + 1) \psi + 2\nabla^2 \psi + \nabla^4 \psi] + \frac{1}{4} \psi^4 \right\} \end{aligned} \quad (4.2)$$

and the equation of motion

$$\partial_t \psi = \nabla^2 \{ [r + (1 + \nabla^2)^2] \psi + \psi^3 \}. \quad (4.3)$$

Equations (4.2) and (4.3) are controlled by two dimensionless parameters, the dimensionless undercooling r and the average density $\bar{\psi} = \langle \psi \rangle$, which is conserved. To describe a real material, the model parameters have to be adjusted to the material properties. Some quantities, as the lattice constant q_0 or the bulk modulus, can be adjusted easily, since the lengths are rescaled with q_0 and the free energy additionally with λ and u . The lattice structure, however, results directly from the form of the free energy and is always triangular for this choice of the free energy [73].

4.1.2 Phase diagram

In the following, the free energy is analyzed in greater detail. As mentioned before, the free energy is constructed in such a way as to allow a periodic phase with a hexagonal structure in two dimensions and a constant phase. As it turns out, there is also a striped phase present [73], which is, however, not important for the situations treated in this work.

In the liquid phase, the constant solution is given by $\psi_L(x, y) = \bar{\psi}$. The energy of the liquid phase can be calculated analytically by inserting $\psi_L(x, y)$ in the free energy, Eq. (4.2), and integrating over a unit volume, leading to $\mathcal{F}_L(\bar{\psi}) = \frac{1}{2}(1+r)\bar{\psi}^2 + \frac{1}{4}\bar{\psi}^4$.

The hexagonal structure can be described by the basis vectors

$$\vec{a} = \frac{2\pi\sqrt{3}}{q} \left(\frac{\sqrt{3}}{2}, \frac{1}{2} \right)$$

and

$$\vec{b} = \frac{2\pi\sqrt{3}}{q} (0, 1),$$

compare section 2.1.

The density for the two-dimensional hexagonal structure can be given in one-mode approximation as [73]

$$\psi_H(x, y) = A_t \left[\cos(qx) \cos(qy/\sqrt{3}) - \cos(2qy/\sqrt{3})/2 \right] + \bar{\psi}. \quad (4.4)$$

To obtain the free energy in the hexagonal phase, the solution ansatz $\psi_H(x, y)$ as given in Eq. (4.4) is inserted into the free energy, Eq. (4.2). Executing the integration over a unit cell and minimizing the free energy with respect to A_t and q gives

$$A_t = \frac{4}{5} \left(\bar{\psi} \pm \frac{1}{3} \sqrt{-15r - 36\bar{\psi}^2} \right), \quad (4.5)$$

where the \pm is for positive/negative $\bar{\psi}$, respectively, and

$$q = \frac{\sqrt{3}}{2}.$$

Reinserting the result into the free energy yields $\mathcal{F}_H(\bar{\psi}, r)$, the analytical one-mode approximation for the free energy in the hexagonal phase.

To obtain the phase diagram of this model system, the free energy of the hexagonal phase is compared with the one of the liquid phase. Since the density is conserved, the coexistence region is given by the solution of the following two equations, corresponding to the graphical common tangent construction. At equilibrium, the chemical potentials in both phases have to be equal, as well as the grand canonical potentials, so that

$$\left. \frac{\partial \mathcal{F}_H}{\partial \bar{\psi}} \right|_{\bar{\psi}_H} = \mu_H = \left. \frac{\partial \mathcal{F}_L}{\partial \bar{\psi}} \right|_{\bar{\psi}_L} = \mu_L \equiv \mu_{Eq} \quad (4.6)$$

and

$$\Omega_H = \mathcal{F}_H(\bar{\psi}_H) - \mu_H \bar{\psi}_H V = \Omega_L = \mathcal{F}_L(\bar{\psi}_L) - \mu_L \bar{\psi}_L V. \quad (4.7)$$

Here, μ is the chemical potential and Ω the grand canonical potential.

With the free energies \mathcal{F}_H and \mathcal{F}_L , one can solve this set of equations numerically, leading to two functions $\bar{\psi}_H(r)$ and $\bar{\psi}_L(r)$, shown in the phase diagram in figure 4.1 as lines limiting the coexistence region.

Between the lines, the liquid and the hexagonal phase can coexist. To be in equilibrium, the chemical potentials in both phases are equal, $\mu_S = \mu_L = \mu_E$. The densities in the two coexisting phases are given by $\bar{\psi}_H(r)$ and $\bar{\psi}_L(r)$, so that the total density of a system at a given r can be written as

$$\bar{\psi}A = \bar{\psi}_H A_H + \bar{\psi}_L A_L,$$

where A is the total area. A_L and A_H are the areas filled by the liquid and the hexagonal phase, respectively.

Solving for the liquid area gives with $A = A_L + A_H$

$$A_L = \frac{\bar{\psi} - \bar{\psi}_H}{\bar{\psi}_L - \bar{\psi}_H} A. \quad (4.8)$$

Varying $\bar{\psi}$ through the coexistence region from $\bar{\psi}_L$ to $\bar{\psi}_H$ decreases the area of liquid phase linearly from the entire system area A to zero, when the entire system is in the hexagonal phase. This linear dependence is called lever rule.

Since the solution of the hexagonal phase is only a one-mode approximation, also the obtained phase diagram is only an approximation. The difference between this approximate free energy \mathcal{F}_H and the free energy obtained from the simulations is shown figure 4.2. While the difference in the free energy is hardly visible, the difference in the chemical potential $\mu_S = \partial_{\bar{\psi}} \mathcal{F}$ is rather large close to the coexistence region, as shown in figure 4.3.

Using the numerically obtained free energy \mathcal{F}_S and chemical potential μ_S , the coexistence lines can be calculated in the same way as described above. This result is shown in figure 4.1 with circles, while the lines correspond to the solution for the one-mode approximation. The crosses represent the coexistence densities as obtained from the simulations. As mentioned before, the free energy also supports a third phase, where the solution is striped or smectic. It is the preferred phases for $\bar{\psi}$ close to zero and does not occur in the simulations in this work. The full phase diagram in one-mode approximation is given e.g. by Elder and Grant [73].

4.1.3 Grain boundary energy

Here, the main interest is focused on the properties of grain boundaries, which are investigated with the phase field crystal model in this chapter. In the following, one has to distinguish between two different integration methods, as explained in section 4.2. The simulations can be performed by fixing the density $\bar{\psi}$ at a certain value and allowing the chemical potential μ to adjust accordingly. This treatment arises quite naturally from the equations of motion. The second method is to fix the chemical potential at a certain value and to allow the density to adjust. This method is more closely related to the thermodynamics of the system, where at equilibrium the grand potentials are equal.

While most of the simulations are performed at constant $\bar{\psi}$, firstly the grain boundary energy is derived generally for a grand canonical ensemble.

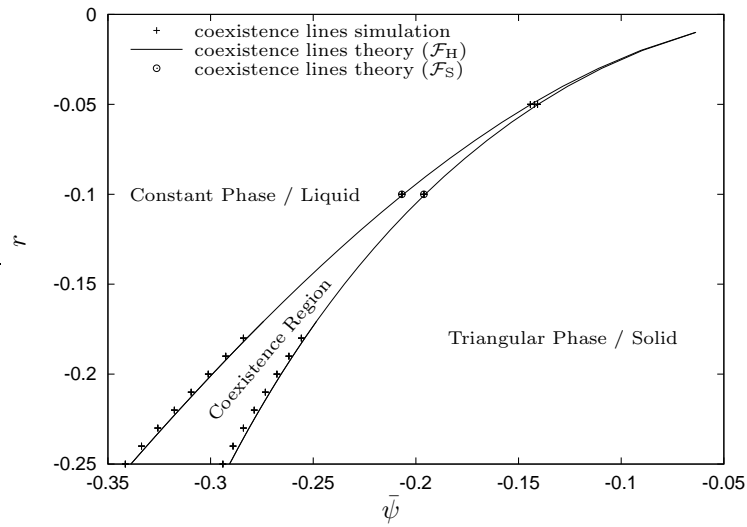


Figure 4.1: Phase diagram showing the coexistence lines for the liquid and the hexagonal phase. The lines show the coexistence lines calculated as described in section 4.1.2 with the free energy \mathcal{F}_H . The points are calculated numerically by relaxing solid-liquid systems with $\bar{\psi}$ in the coexistence region. For small r , the results differ slightly. The difference can be reduced by calculating the coexistence line using the numerically obtained free energy \mathcal{F}_S instead of \mathcal{F}_H , as shown with circles.

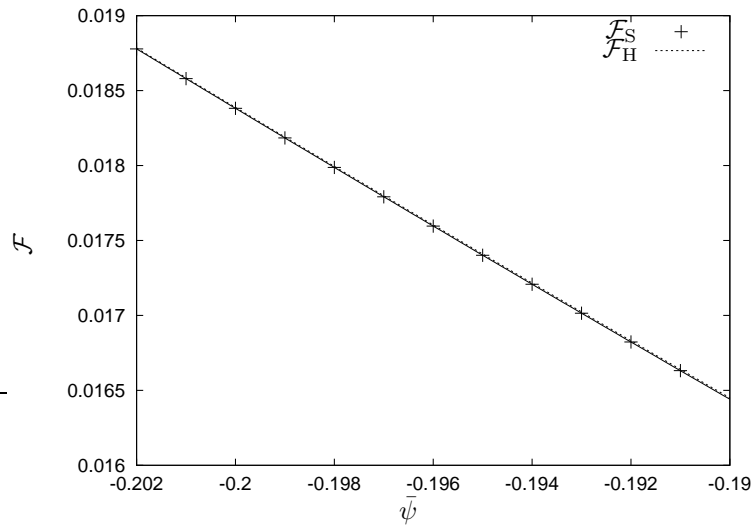


Figure 4.2: Real free energy \mathcal{F}_S of a pure solid compared with the free energy for the hexagonal phase. The differences are hardly visible.

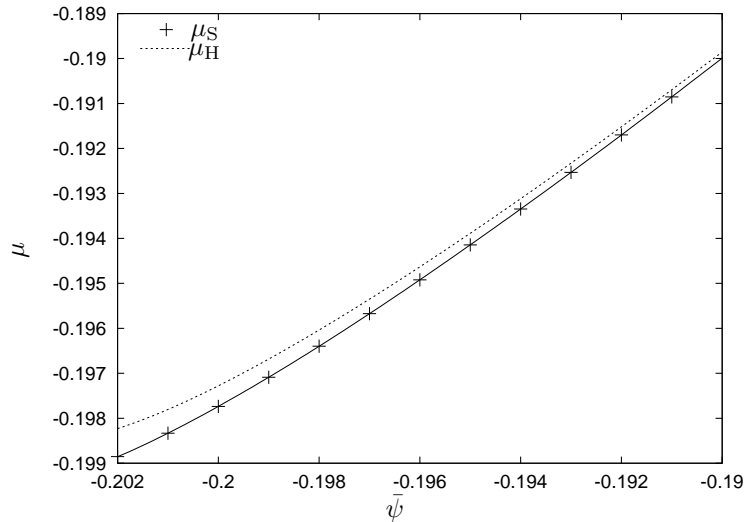


Figure 4.3: Chemical potential $\mu_S = \partial_{\bar{\psi}} \mathcal{F}_S$ of a pure solid compared with μ_H for the hexagonal phase. Here, the differences become important.

Instead of the excess free energy, the grain boundary energy is then given as the excess free grand potential

$$\gamma_{\text{GB}} L_I = \omega_{\text{exc}} = \int [\omega(x, y) - \omega_S] dV, \quad (4.9)$$

where L_I is the length of the interface and the reference state is the solid state.

For a system with planar interface parallel to the y -axis which is on a mesoscopic scale translationally invariant in y direction, one can carry out the integration and use the average values ω and f in the system with interface. Using $\omega = f - \mu\bar{\psi}$, the excess free energy can be written as,

$$\begin{aligned} 2\gamma_{\text{GB}} &= L_x [\omega - \omega_S] \\ &= L_x \{f - f(\bar{\psi}_S) - \mu [\bar{\psi} - \bar{\psi}_S]\}. \end{aligned} \quad (4.10)$$

The factor two takes into account that in the periodic systems treated here always two interfaces are present, compare figure 4.4 (bottom). It is, however, assumed that they are well separated and that they do not interact.

In the case of constant $\bar{\psi}$ and varying μ , one can expand $f(\bar{\psi}_S)$ around $\bar{\psi}$ and one obtains with $\mu = \partial_{\bar{\psi}} f(\bar{\psi})$

$$\begin{aligned} f &\approx \frac{2\gamma_{\text{GB}}}{L_x} + f(\bar{\psi}) + \mu(\bar{\psi}_S - \bar{\psi}) + \mu(\bar{\psi} - \bar{\psi}_S) \\ &= \frac{2\gamma_{\text{GB}}}{L_x} + f(\bar{\psi}). \end{aligned} \quad (4.11)$$

The total free energy of a system with grain boundary f can be easily obtained from the simulations. To determine the corresponding free energy $f(\bar{\psi})$ turns out to be more difficult, since very small variations lead to a large differences in the grain boundary energy. In this work, it is therefore preferred to

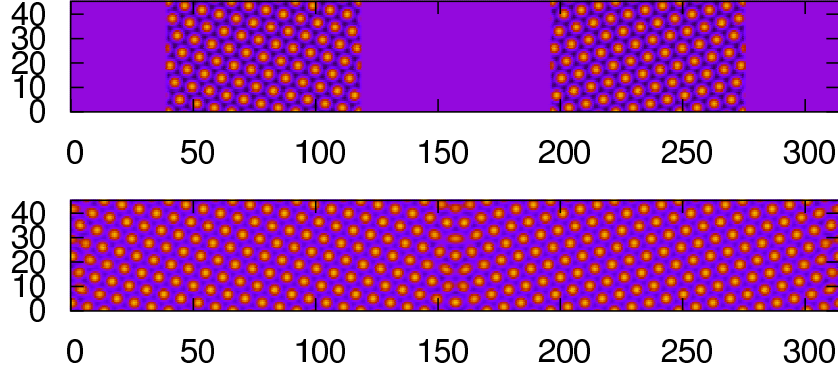


Figure 4.4: Top: Initial condition for the grain boundary simulations. Two solids with different orientations are separated by liquid layers. Bottom: After a few time steps, the liquid solidifies and the grain boundaries build up. Due to periodic boundary conditions, there are always two solid-solid interfaces: one in the middle of the system and the other one at the boundaries.

plot f versus $1/L_x$ for several system lengths L_x and exploit the linear dependency. A linear fit gives as slope $2\gamma_{\text{GB}}$ and as y -intercept the free energy of a corresponding solid without interface.

For simulations at constant μ , the grain boundary energy can be obtained similarly, but then $\bar{\psi}$ varies with L_x .

To compare the simulations with the theory, the grain boundary energy for small angles given in Eq. (2.2) is written as

$$\begin{aligned} \gamma_{\text{GB}} &= \frac{Ga}{4\pi(1-\sigma)}\theta [1 - \ln(2\pi\theta) + \ln(a/r_0)] \\ &\equiv E_M\theta \left[1 - \ln \frac{\theta}{\theta_M} \right], \end{aligned} \quad (4.12)$$

with $E_M = \frac{Ga}{4\pi(1-\sigma)}$ and $\theta_M = \frac{a}{2\pi r_0}$ as derived by Elder et al. [72]. As explained in section 2.1, r_0 is a length to be obtained by atomistic calculations and $a = 2\pi/q$ is the lattice constant.

Please note that σ appearing in the Read-Shockley grain boundary energy is the three-dimensional Poisson's ratio, while the σ from Elder et al. [72, 73] is the two-dimensional Poisson's ratio.

For the one-mode approximation, the elastic properties of the phase field crystal model can be derived [72, 73]. The resulting elastic constants are $C_{11}/3 = C_{12} = C_{44} = \left(3\bar{\psi} - \sqrt{-15r - 36\bar{\psi}^2}\right)^2 / 75$. The bulk modulus can then be calculated to $B = 2 \left(3\bar{\psi} - \sqrt{-15r - 36\bar{\psi}^2}\right)^2 / 75$ and the shear modulus or rigidity modulus $G = C_{44}$. Furthermore, the three-dimensional Poisson's ratio is given as $\sigma = \frac{1}{2} \frac{3B-2G}{3B+2G} = 1/4$.

As one can see, the elastic constants depend on the dimensionless temperature r and on the density $\bar{\psi}$. For the grain boundary energy, written as a function

of r and $\bar{\psi}$, it then follows

$$\gamma_{\text{GB}}(\bar{\psi}, r) = \frac{4}{25\sqrt{3}} \left[\bar{\psi} - \frac{1}{3} \sqrt{-15r - 36\bar{\psi}} \right]^2 \theta [1 - \ln(2\pi\theta) + \ln(a/r_0)]. \quad (4.13)$$

Please remember that in this work the average density is taken to be negative, therefore $\bar{\psi}_S > \bar{\psi}_L$. In Elder et al. [72, 73], positive densities are chosen. This explains the different sign in front of the square-root.

The radius r_0 is taken as a free parameter, which also might depend on the density $\bar{\psi}$ and on the dimensionless temperature r .

4.2 Implementation

The phase field crystal model is based on a differential equation, which contains a sixth order gradient term. This makes it numerically time-consuming when using the simplest integration algorithm, as used for the phase-field model in the rest of this work. In section 4.2.1, an implicit scheme is presented, where the gradients are calculated in Fourier space.

Numerically, one is restricted to finite systems, where the boundaries have to be defined. Since the crystal is represented by a periodic function, the simulation box has to respect this periodicity. This leads to box sizes which depend on the orientation of the crystal, as shown in section 4.2.2.

4.2.1 Integration of the equation of motion

Conserved order parameter

Treating ψ as conserved order parameter, the equation of motion is given in Eq. (4.3) as

$$\begin{aligned} \partial_t \psi &= \nabla^2 \left(\frac{\delta \mathcal{F}}{\delta \psi} \right) \\ &= (r+1)\nabla^2 \psi + 2\nabla^4 \psi + \nabla^6 \psi + \nabla^2 \psi^3 \\ &= \hat{L}\psi + f, \end{aligned} \quad (4.14)$$

where here the linear operator $\hat{L} = (r+1)\nabla^2 + 2\nabla^4 + \nabla^6$ and the nonlinear function $f = \nabla^2 \psi^3$ have been introduced.

To avoid the numerically challenging gradient terms in real space, one can solve the equation of motion in Fourier space. Multiplying by $\exp(i\vec{k}\vec{x})$ and integrating both sides over the entire volume leads to

$$\begin{aligned} \int \partial_t \psi(\vec{x}) \exp(i\vec{k}\vec{x}) d\vec{x} &= \underbrace{\int \hat{L}\psi(\vec{x}) \exp(i\vec{k}\vec{x}) d\vec{x}}_{\int \exp(i\vec{k}\vec{x}) [\hat{L}\psi + \psi \hat{L} \exp(i\vec{k}\vec{x})] d\vec{x}} + \int f \exp(i\vec{k}\vec{x}) d\vec{x} \\ \partial_t \tilde{\psi}_k &= \hat{L}_k \tilde{\psi}_k + \tilde{f}_k, \end{aligned} \quad (4.15)$$

where one can identify the Fourier modes of the density $\tilde{\psi}_k = \int \psi \exp(i\vec{k}\vec{x}) dx$. Here, $\hat{L}_k = -(r+1)k^2 + 2k^4 - k^6$ is the linear operator in Fourier space and \tilde{f}_k is the Fourier transform of the nonlinear function f .

“Non-local” conserved dynamics

Another way of calculating the time evolution of the system is to formally treat ψ as nonconserved order parameter in the way of writing the equation of motion, but ensure that it remains globally conserved by using a Lagrange multiplier.

The advantage of this method is that the equilibrium can be found faster. Since in the equation of motion the concentration is formally not conserved, the mass can be transported in a faster way by taking it at some place and placing it at another, as favored by the free energy. Therefore, the dynamics of this method is different. In this work, the method can be used without problems since the main interest is focused on equilibrium situations.

The conservation condition for ψ is given as

$$\frac{1}{A} \int \psi(\vec{x}) d\vec{x} - \bar{\psi} = 0,$$

where A is the total volume or, in two dimensions, the total area.

The free energy, including the constraint, can then be written as

$$\tilde{\mathcal{F}} = \mathcal{F} + \mu \left[\frac{1}{A} \int \psi(\vec{x}) d\vec{x} - \bar{\psi} \right],$$

where the Lagrange multiplier is called μ . For the equation of motion one obtains

$$\begin{aligned} \partial_t \psi &= -\frac{\delta \mathcal{F}}{\delta \psi} + \frac{\mu}{A} \\ &= [-(r+1) - 2\nabla^2 - \nabla^4] \psi - \psi^3 + \frac{\mu}{A} \\ &= \hat{L} \psi + f, \end{aligned} \quad (4.16)$$

where now $\hat{L} = -(r+1) - 2\nabla^2 - \nabla^4$ and $f = -\psi^3 + \frac{\mu}{A}$. In Fourier space, the operator and the nonlinear function are given as $\hat{L}_k = -(r+1) + 2k^2 - k^4$ and $\tilde{f}_k = -\tilde{\psi}_k^3 + \frac{\tilde{\mu}_k}{A}$, where $\tilde{\psi}_k^3$ is the Fourier transform of ψ^3 and $\tilde{\mu}_k$ the one of μ . Since μ is a constant, $\tilde{\mu}_k \propto \delta(k)\mu$.

The Lagrange multiplier μ can be obtained from the condition

$$0 = \partial_t \bar{\psi} = \frac{1}{A} \int \partial_t \psi(\vec{x}) d\vec{x} = \frac{1}{A} \int \left[-\frac{\delta \mathcal{F}}{\delta \psi} + \frac{\mu}{A} \right] d\vec{x},$$

or

$$\mu = \int \frac{\delta \mathcal{F}}{\delta \psi} d\vec{x} = \int [(r+1)\psi(\vec{x}) + \psi^3(\vec{x})] d\vec{x},$$

since the integral over the gradients for a periodic system is zero.

The Lagrange multiplier is called μ for a good reason: it corresponds to the chemical potential of the system. Therefore, this method also allows to fix the chemical potential and let the total density adjust accordingly. This method corresponds more closely to the thermodynamical idea of having a grand canonical ensemble.

However, a problem with this method arises for simulations with $\bar{\psi}$ inside the coexistence region. Here, the density $\bar{\psi}$ is not a unique function of μ , since for all $\bar{\psi}_L < \bar{\psi} < \bar{\psi}_S$ the chemical potential $\mu = \mu_{\text{Eq}}$.

Proof that the energy is minimized

In the following, it is shown that \mathcal{F} is minimized, being subject to the constraint

$$\int d\vec{x}\psi = A\bar{\psi}, \quad (4.17)$$

in a domain of volume A .

Using the standard method of Lagrange multipliers, one seeks to minimize

$$\tilde{\mathcal{F}} = \mathcal{F} - \mu \left(\frac{1}{A} \int d\vec{x}\psi - \bar{\psi} \right), \quad (4.18)$$

which yields the evolution equation

$$\partial_t\psi = -\frac{\delta\mathcal{F}}{\delta\psi} + \mu, \quad (4.19)$$

where μ needs to be determined by the differential form of Eq. (4.17)

$$\int d\vec{x}\partial_t\psi = 0. \quad (4.20)$$

Integrating both sides of Eq. (4.19) and using Eq. (4.20), one obtains

$$\mu = \frac{1}{A} \int d\vec{x} \frac{\delta\mathcal{F}}{\delta\psi}. \quad (4.21)$$

Substituting Eq. (4.21) into Eq. (4.19) yields the final evolution equation

$$\partial_t\psi = -\frac{\delta\mathcal{F}}{\delta\psi} + \frac{1}{A} \int d\vec{x} \frac{\delta\mathcal{F}}{\delta\psi}. \quad (4.22)$$

So one just needs to evolve ψ using Eq. (4.22) and, at the end of the calculation, gets μ from Eq. (4.21) after ψ has reached a stationary state.

It can be shown that this dynamics leads to a continuous decrease of the modified free energy $\tilde{\mathcal{F}}$. From the time derivative of Eq. (4.18), one obtains

$$\frac{d\tilde{\mathcal{F}}}{dt} = \int d\vec{x} \frac{\delta\tilde{\mathcal{F}}}{\delta\psi(\vec{x})} \frac{\partial\psi(\vec{x})}{\partial t} + \frac{d\mu}{dt} \left(\int d\vec{x}\psi - A\bar{\psi} \right). \quad (4.23)$$

However, the last term is zero because the bracket contains just the constraint to be enforced. For the first term, since $\delta\tilde{\mathcal{F}}/\delta\psi(\vec{x}) = \delta\mathcal{F}/\delta\psi(\vec{x}) - \mu$ from Eq. (4.18), using Eq. (4.19) yields

$$\frac{d\tilde{\mathcal{F}}}{dt} = - \int d\vec{x} \left(\frac{\delta\mathcal{F}}{\delta\psi} - \mu \right)^2. \quad (4.24)$$

Thus, the time derivative is always negative and becomes zero for $\delta\mathcal{F}/\delta\psi(\vec{x}) = \mu$ as desired. Note that μ changes with time and is not determined a priori. Therefore, as usual with this kind of evolution, one can end up in metastable states which can be characterized by a different μ than the real equilibrium state. Hence, it is important to start with an initial guess not too far from the desired final state.

Implicit scheme

To be able to increase the time steps in the integration, it is possible to use an implicit integration scheme. Instead of solving Eq. (4.15) directly numerically, one can rewrite it by using the ansatz $\tilde{\psi}_k = u(t) \exp(\hat{L}_k t)$. One then obtains

$$\partial_t \tilde{\psi}_k = \hat{L}_k \exp(\hat{L}_k t) u(t) + (\partial_t u) \exp(\hat{L}_k t) = \hat{L}_k \exp(\hat{L}_k t) u(t) + \tilde{f}_k,$$

so that $\partial_t u(t) = \exp(-\hat{L}_k t) \tilde{f}_k$. Integrating over time from t to $t + \Delta$ gives

$$u(t + \Delta) - u(t) = \int_t^{t+\Delta} dt' \exp(-\hat{L}_k t') \tilde{f}_k(t')$$

and with $u(t) = \exp(-\hat{L}_k t) \psi(t)$ in terms of ψ

$$\exp[-\hat{L}_k(t + \Delta)] \psi(t + \Delta) - \exp(-\hat{L}_k t) \psi(t) = \int_t^{t+\Delta} dt' \exp(-\hat{L}_k t') \tilde{f}_k(t').$$

Even if \tilde{f}_k is not known as a function of t , it can be expanded in a good approximation around $t' = t$, leading to

$$\begin{aligned} \tilde{\psi}_k(t + \Delta) &= e^{\Delta t \hat{L}_k} \tilde{\psi}_k(t) \\ &+ e^{\hat{L}_k(t+\Delta t)} \int_t^{t+\Delta t} dt' e^{-\hat{L}_k t'} \left[\tilde{f}_k(t) + \frac{\tilde{f}_k(t) - \tilde{f}_k(t - \Delta t)}{\Delta t} (t' - t) \right] \\ &= e^{\Delta t \hat{L}_k} \tilde{\psi}_k(t) + \frac{\tilde{f}_k(t)}{\hat{L}_k} \left(e^{\hat{L}_k \Delta t} - 1 \right) \\ &+ \frac{\tilde{f}_k(t) - \tilde{f}_k(t - \Delta t)}{\Delta t \hat{L}_k^2} \left(e^{\hat{L}_k \Delta t} - 1 - \Delta t \hat{L}_k \right). \end{aligned} \quad (4.25)$$

This scheme can be applied independently of the integration mode, whether the density or the chemical potential is kept fixed. One only has to choose the appropriate linear operator \hat{L} and non-linear function f .

Due to the implicit integration scheme, the time-steps can be chosen quite large, in the simulations in this work $\Delta t = 0.4$. Since the gradients are calculated in Fourier-space, also the discretization of the space can be chosen rather large, $dx \approx \pi/4$, depending slightly on the orientations in the system.

4.2.2 Boundary conditions

In numerical simulations, one is restricted to finite systems. It is therefore important to define proper boundary conditions. Usually, periodic or reflecting boundary conditions are applied, allowing to extend the system theoretically to infinity. Due to the use of the Fourier transformation, periodic boundary conditions arise quite naturally, but it is also possible to use reflecting boundary conditions. In either way, the boundary condition imposes certain constraints on the crystalline structure inside the simulation box. Or, with other words, it is important to have the correct size of the simulation box to fit exactly an integer multiple of the periodicity of the atomic structure.

For the two-dimensional hexagonal structure, the solution is given in Eq. (4.4) as

$$\psi_H(x, y) = A_t \left[\cos(qx) \cos(qy/\sqrt{3}) - \cos(2q/\sqrt{3})/2 \right] + \bar{\psi}.$$

The resulting structure can be described by two basis vectors $\vec{a} = \frac{2\pi\sqrt{3}}{q} \left(\frac{\sqrt{3}}{2}, \frac{1}{2} \right)$ and $\vec{b} = \frac{2\pi}{q}\sqrt{3}(0, 1)$, compare section 4.1.2. Allowing a rotation of the entire structure by an angle θ ($x \rightarrow x \cos \theta + y \sin \theta$ and $y \rightarrow -x \sin \theta + y \cos \theta$), the vectors can be written as

$$\begin{aligned}\vec{a}' &= \frac{2\pi}{q}\sqrt{3} \begin{pmatrix} \sqrt{3}/2 \cos(\theta) + \frac{1}{2} \sin(\theta) \\ -\sqrt{3}/2 \sin(\theta) + \frac{1}{2} \cos(\theta) \end{pmatrix} \quad \text{and} \\ \vec{b}' &= \frac{2\pi}{q}\sqrt{3} \begin{pmatrix} \sin(\theta) \\ \cos(\theta) \end{pmatrix}.\end{aligned}$$

To have a periodic structure in the simulation box, there are two restrictions on the lengths L_x and L_y :

$$\begin{aligned}n\vec{a}' - m\vec{b}' &= \begin{pmatrix} L_x \\ 0 \end{pmatrix} \quad \text{and} \\ i\vec{b}' - j\vec{a}' &= \begin{pmatrix} 0 \\ L_y \end{pmatrix},\end{aligned}$$

where n , m , i and j are integer numbers and $\theta < \pi/3$.

Solving the two equations where the right hand side is equal to zero for θ leads to conditions for n , m , i and j , namely

$$\begin{aligned}\tan \theta &= \frac{n - 2m}{\sqrt{3}n} \quad \text{and} \\ \tan \theta &= \frac{\sqrt{3}j}{2i - j}.\end{aligned}$$

For the lengths of the simulation box, it then follows

$$\begin{aligned}L_x &= \frac{2\pi}{q}\sqrt{3} \left[n \frac{\sqrt{3}}{2} \cos \theta + \left(\frac{n}{2} - m \right) \sin \theta \right] \quad \text{and} \\ L_y &= \frac{2\pi}{q}\sqrt{3} \left[\left(i - \frac{j}{2} \right) \cos \theta + \frac{\sqrt{3}}{2} j \sin \theta \right].\end{aligned}$$

One can see that the required system size depends strongly on the orientation. This limits the orientations which can be simulated in this work. Especially, going to smaller misorientations requires larger simulation boxes. In the case of grain boundaries, this can be seen directly from the dislocation picture. The smaller the misorientation, the larger is the distance between the dislocations and therefore also the required system size.

4.3 Numerical results

In the following, systems with planar interfaces are investigated. The interface is aligned parallel to the y -axes, so that the system is macroscopically translationally invariant in this direction, compare figure 4.4 (bottom). Microscopically, however, it is not invariant under an arbitrary translation. This can best be seen in the case of a grain boundary, which can be described as a line of discrete dislocations, whose distance determines the misorientation angle. It becomes clear

that microscopically the system is only invariant under translations which are multiples of this distance. This problem is also discussed in section 4.2.2.

Due to the periodic boundary conditions, one always has at least two interfaces in the system. They are, however, far enough away from each other not to interact.

The grain boundaries are constructed by rotating two solid slabs by an angle $\theta/2$ in opposite directions, forming a symmetric tilt grain boundary of an angle θ . The solid is created using the density field given by the one-mode approximation $\psi_H(x, y)$, as given in Eq. (4.4). In between the solid slabs, a liquid phase is placed, where $\bar{\psi}_L = \bar{\psi}$, as shown in figure 4.4 (top). The densities are chosen to be on the negative branch of the phase diagram. Therefore, the density of the solid phase is larger than the density in the liquid phase. To obtain grain boundaries, $\bar{\psi}$ is chosen to be in the coexistence region or within the solid phase. Within a few time-steps, the liquid hence solidifies and the grain boundary builds up. To find the real grain boundary properties, the system is evolved for a much longer time, to ensure that the system is in equilibrium and the chemical potential μ is uniform in the entire system.

If not explicitly stated, the control parameter r is fixed in the following at a value of $r = -0.1$ and the average density $\bar{\psi}$ is varied.

4.3.1 Order in the grain boundary

In this subsection, the main interest is focused on the grain boundary and how a local order parameter can be defined in it. On both sides of the grain boundary, in the solid bulk, the hexagonal lattice is unperturbed, characterized by a periodically oscillating density function. Integrating over a full period gives a local average density, which is constant in the bulk phases. Since the system is periodic parallel to the interface, integrating along the y -axis corresponds to integrating over a full period. One can define $\bar{\psi}_y(x) \equiv \int \psi(x, y) dy$, which is independent of x in all solids with exception of grains aligned with the y -axis. Here, this integration gives an oscillating function and one has to integrate over a period of x , too.

In the liquid, as has been shown in section 4.1, the density function is always constant with a value smaller than the average value in the solid. Defining a $\bar{\psi}_y(x)$ is therefore possible, too.

To investigate a solid-liquid phase transition with an interface parallel to the y -axis, one can now plot $\bar{\psi}_y(x)$ as function of x , varying x from the solid to the liquid phase. The result is shown in figure 4.5. One can see how $\bar{\psi}_y(x)$ decreases smoothly when going from solid to liquid, varying over a certain interface width ξ of a few atomic layers. This is in agreement with theoretical and experimental findings about solid-liquid interfaces [5].

Similarly, $\bar{\psi}_y(x)$ can be plotted as a function of x for a system with two solids with different orientations. The result is shown in figures 4.6 and 4.7 with the red line for two grain boundaries with different average densities. As one goes from one grain to the other, passing the grain boundary, the density decreases. The closer the system is to the coexistence region (smaller $\bar{\psi}$), the further down the density goes. For the system with rather low density, far inside the solid phase, one can see that $\bar{\psi}_y(x)$ starts to oscillate in the grain boundary, increasing exactly in between the two grains.

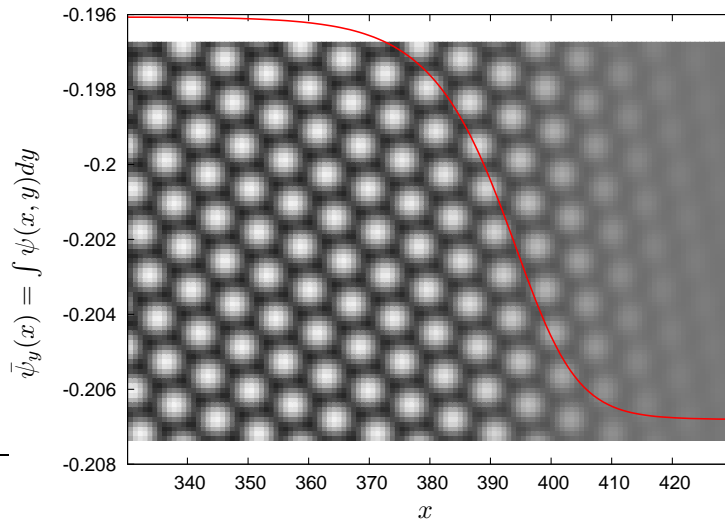


Figure 4.5: Solid-liquid interface. The red line shows how the local average density $\bar{\psi}_y(x) = \int \psi(x, y) dy$ changes over the interface. It varies continuously from $\bar{\psi}_S$ in the solid to $\bar{\psi}_L$ in the liquid. The variation takes place over a certain interface width ξ . In the background, the density field $\psi(x, y)$ is shown in a gray-scale plot. The light regions correspond to a high density, whereas the darker ones correspond to a low density. One can clearly see the hexagonal structure in the solid phase and the transition to the continuous liquid phase. The average density in the system is $\bar{\psi} = -0.2$, a value being far inside the coexistence region.

Being interested in the local order, one can define a local order parameter by performing a wavelet transformation [77]. This is shown with the blue line. One can see that this parameter also decreases in the interface but without oscillations.

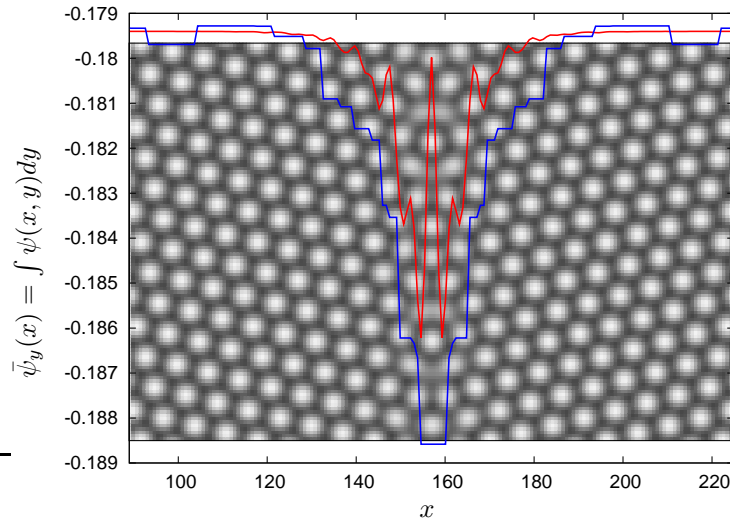


Figure 4.6: Solid-solid interface of a symmetric tilt grain boundary with a misorientation angle of 32.2° . With the red line, the local average density $\bar{\psi}_y(x) = \int \psi(x, y) dy$ is shown. $\bar{\psi}_y(x)$ is constant in both solid bulk phases and decreases in the grain boundary. However, there are oscillations, corresponding to higher densities with a maximum at the dislocation line in the middle of the grain boundary. To avoid these oscillations, one can use another measurement of the order, as shown with the blue line. In the background, $\bar{\psi}(x, y)$ is shown. The average density $\bar{\psi} = -0.18$, a value far inside the solid region.

To summarize, one can state that the local order decreases in the grain boundary, similar as the order decreases as going from solid to liquid. Regarding the local orientation of the crystalline phase, it remains constant in the two phases where the order is high and changes drastically in the grain boundary, where the order is decreased.

This observation is used in chapter 5 when developing a phase-field model for polycrystalline solidification.

4.3.2 Grain boundaries

In this subsection, the grain boundaries as obtained in the phase field crystal model are investigated for different misorientations and densities. Before calculating the grain boundary energy, some snapshots of grain boundaries are presented. The system size of the simulation box is chosen as small as possible, it always contains one pair of dislocations. Since the distance between the dislocations increases as the misorientation becomes smaller, the largest simulation boxes are needed for the smallest misorientations. Inversely, the dislocations

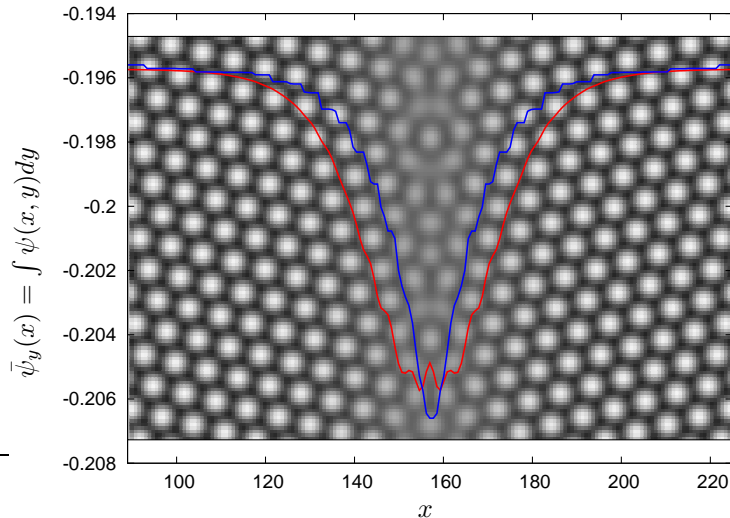


Figure 4.7: Same solid-solid interface as in figure 4.6 but with an average density $\bar{\psi} = -0.198$, a value still in the coexistence region but close enough to the solid region to allow the solid-solid interface to build up.

approach each other as the angle becomes larger and, since their core radius is rather independent of the misorientation, start to overlap for large misorientations. One can therefore see quite clearly when the picture of having a line of separated dislocations breaks down, and with it the estimation of the grain boundary energy following Read-Shockley [21].

In figure 4.8 to figure 4.13, the grain boundary is shown for different misorientations. The average density is far inside the solid region of the phase diagram, $\bar{\psi} = -0.1$. To make it easier to see the dislocation pairs, the plotted region is extended using the periodicity and twice the thickness used in the simulation is plotted, showing two dislocation pairs instead of one. Also, only one of the simulated grain boundaries is shown. The left and right part of the simulation box is omitted.

In figure 4.14, a low-angle grain boundary (left) and a high-angle grain boundary (right) are shown for different values of $\bar{\psi}$. As $\bar{\psi}$ is increased from top to bottom, the liquid layer between the two grains becomes smaller. As the grain boundaries interact, one can see that the behavior is different for the two cases. For the high-angle grain boundary, the liquid remains as a film of constant width between the grains. For the low-angle grain boundary, the liquid is collected around the dislocation cores. The two dislocations attract each other, sharing a liquid pool around their cores and hence breaking the symmetry of the system. As $\bar{\psi}$ is further increased, the distance between the dislocations becomes relatively equal. Without liquid, this allows to minimize the elastic energy.

Grain boundary energy

In the following, the grain boundary energy is obtained for systems with different misorientations. As explained in section 4.1.3, one can exploit the linear behavior

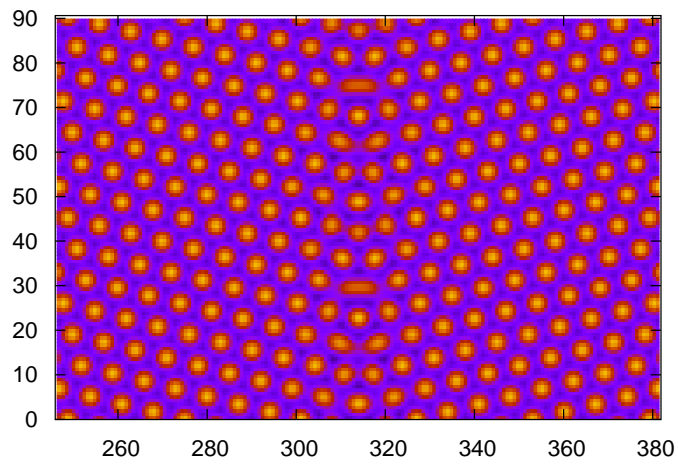


Figure 4.8: Snapshot of a grain boundary with a misorientation $\theta = 32.2^\circ$.

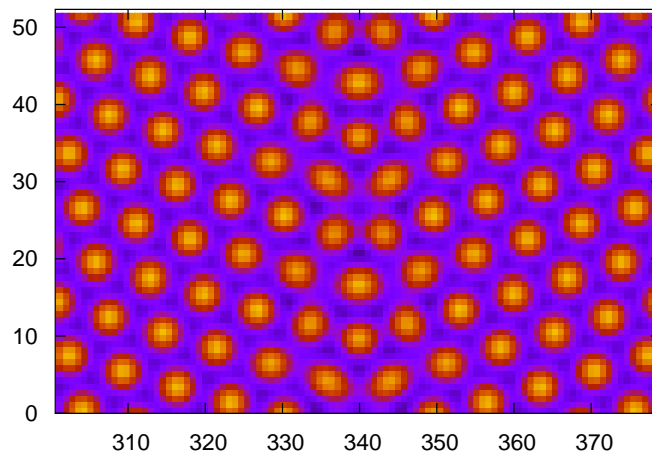


Figure 4.9: Snapshot of a grain boundary with a misorientation $\theta = 27.8^\circ$.

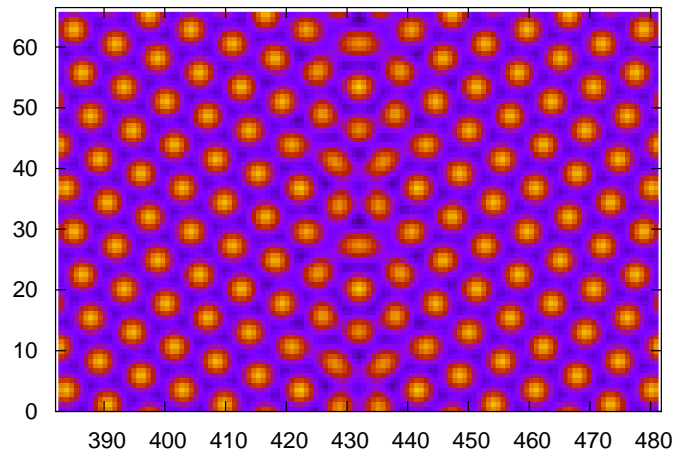


Figure 4.10: Snapshot of a grain boundary with a misorientation $\theta = 21.8^\circ$.

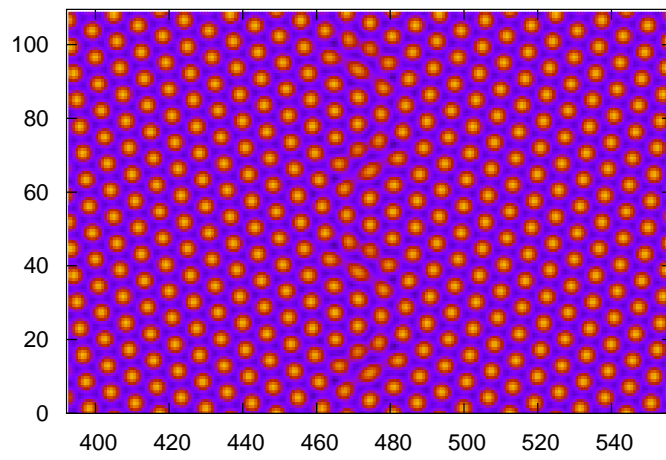


Figure 4.11: Snapshot of a grain boundary with a misorientation $\theta = 13.2^\circ$.

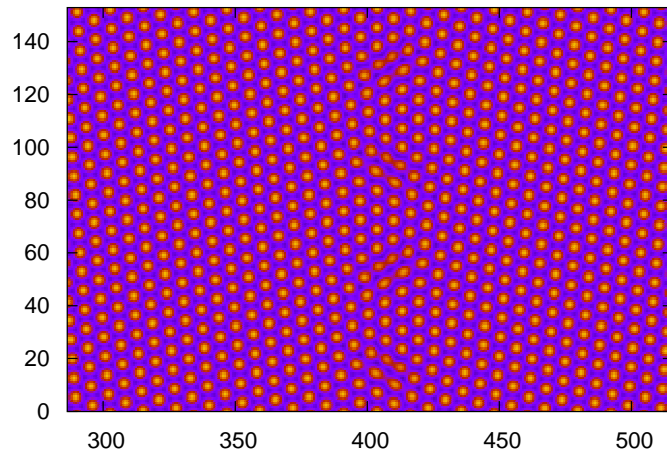


Figure 4.12: Snapshot of a grain boundary with a misorientation $\theta = 9.4^\circ$.

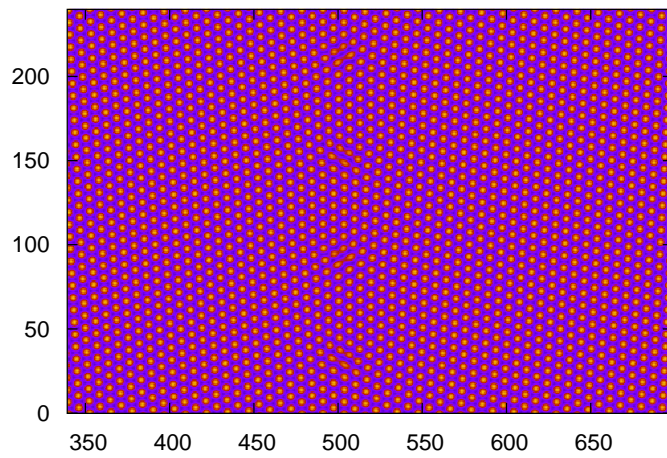


Figure 4.13: Snapshot of a grain boundary with a misorientation $\theta = 6.0^\circ$.

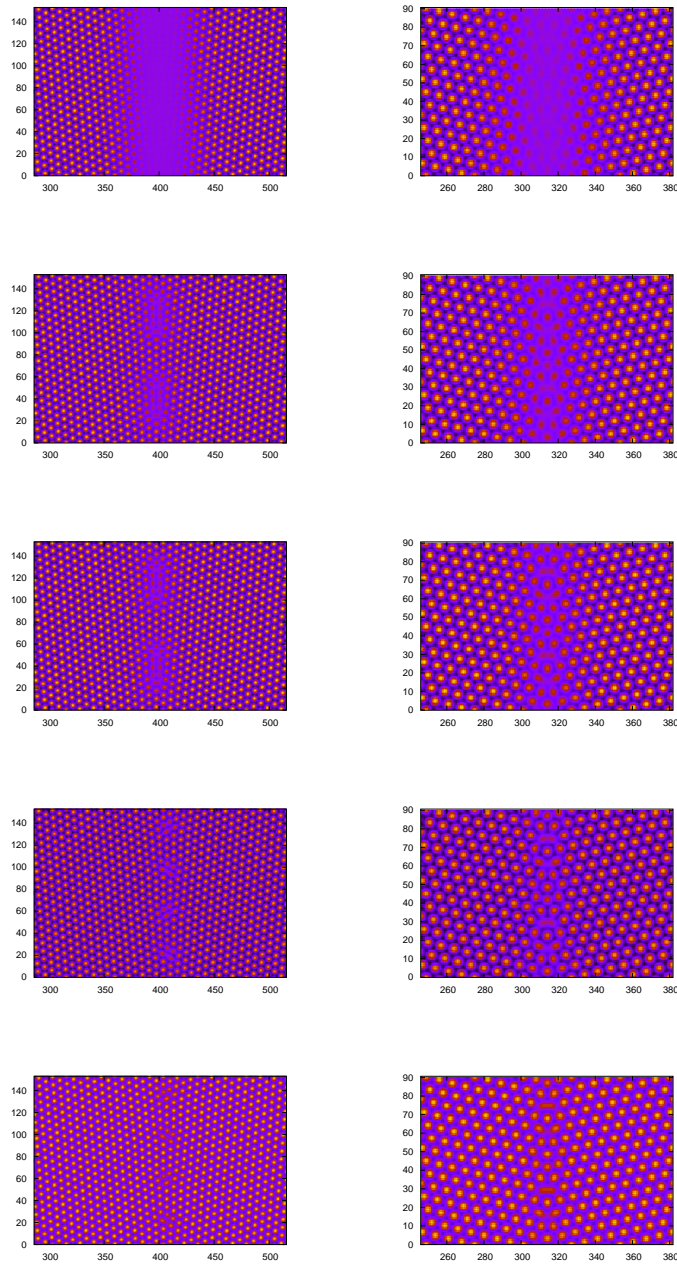


Figure 4.14: Snapshots of a low-angle grain boundary with $\theta = 9.4^\circ$ (left) and high-angle grain boundary with $\theta = 32.2^\circ$ (right) for different values of $\bar{\psi}$. From top to bottom, the average density is increased from $\bar{\psi} = -0.198$ to $\bar{\psi} = -0.197$, both being inside the coexistence region, to $\bar{\psi} = -0.196$ just below coexistence, further to $\bar{\psi} = -0.190$ and finally to $\bar{\psi} = -0.180$, quite far inside the solid region. One can see that the liquid forms a rather homogeneous film for the high-angle grain boundary, while in the low-angle case the liquid concentrates around the dislocation cores when the two grains get closer.

of the free energy with the grain boundary energy when plotting it against $1/L_x$, where L_x is the system length perpendicular to the interface, as given in Eq. (4.11).

This is shown in figure 4.15, for a system with $r = -0.1$, $\bar{\psi} = -0.1$ and a misorientation of 6° . The points are fitted by a straight line, giving the grain boundary energy as its slope. Using more than two systems of different lengths allows one to obtain an estimation for the error of γ_{GB} from the fit. This method is repeated for systems with different misorientations and different densities $\bar{\psi}$.

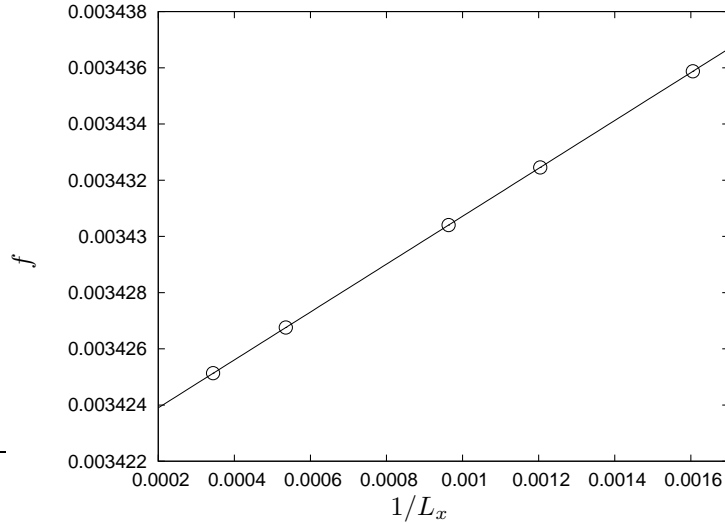


Figure 4.15: The grain boundary energy is obtained by plotting the free energy of systems with the same misorientation and average densities $\bar{\psi}$ but different lengths L_x perpendicular to the interface against $1/L_x$. The slope gives twice the grain boundary energy, where the factor of two is due to the fact that in periodic systems there are always two grain boundaries.

The grain boundary energy is shown in figure 4.16 as a function of the misorientation θ for different values of $\bar{\psi}$. On the lower x -axis, the misorientation angle is given in radians, while on the upper one it is given in degrees. The data is compared with the theoretical grain boundary energy as given in Eq. (4.13), where the parameter r_0 is obtained by a least square fit. Since this expression is only valid for small misorientations, for the fit only systems with $\theta < 15^\circ$ have been included. One can see that the agreement is very good for small angles, while it fails for larger misorientations.

In figure 4.17, the obtained radius r_0 is shown as a function of the average density $\bar{\psi}$. One can see that it is rather constant for large values of $\bar{\psi}$, which are far inside the coexistence region. The estimate of $r_0 = a \exp(-0.5) = 4.4$ from Elder and Grant [73] is rather good average value. The lattice constant is given as $a = 7.26$ in these simulations.

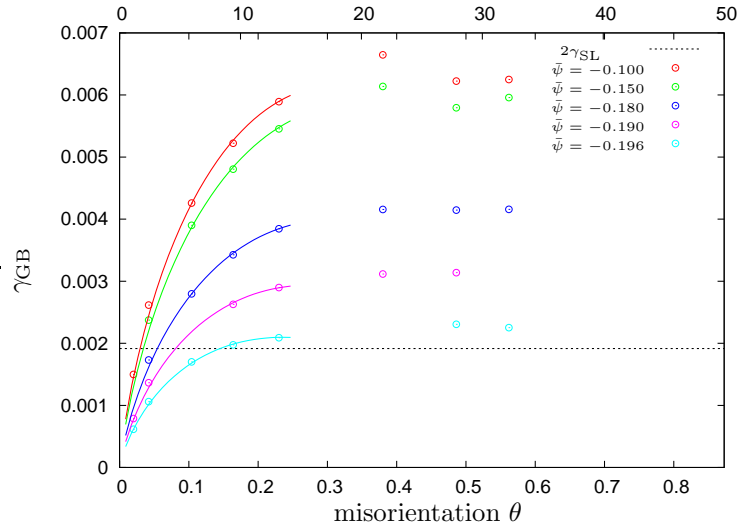


Figure 4.16: Grain boundary energy as a function of the misorientation θ , shown for different densities. The lowest curve, $\bar{\psi} = -0.196$, is very close to the coexistence region ($\bar{\psi}_S \approx -0.19608$), while the upper curve is far inside the solid region. The lines correspond to the grain boundary energy as obtained from Eq. (4.13), where r_0 is obtained by a least square fit. As predicted in the derivation of the grain boundary energy, the agreement is very good for small misorientation, while it fails for high-angle grain boundaries.

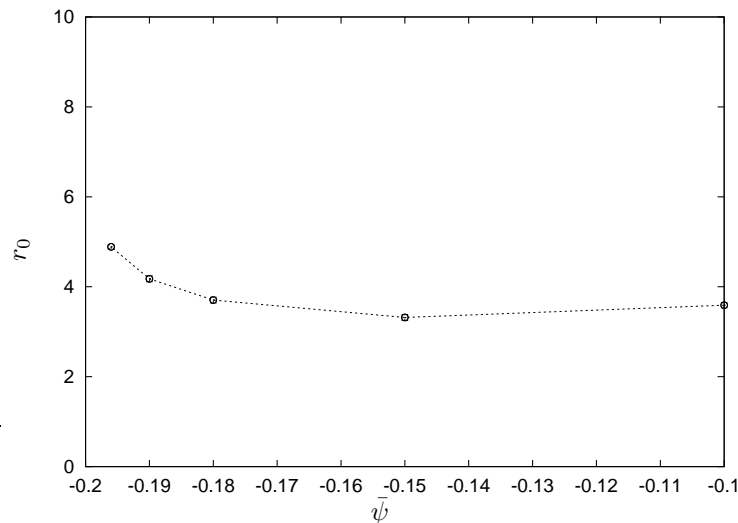


Figure 4.17: The values of r_0 as obtained in the fit, shown in figure 4.16 as a function of the average density $\bar{\psi}$. Far inside the solid region, r_0 is rather constant, while it increases when approaching the coexistence region. For comparison, the lattice constant is $a = 7.26$ and the value estimated by Elder and Grant [73] is $r_0 = 4.4$.

4.3.3 Grain boundary wetting

During the solidification, two grains with different orientations can approach each other, having a thinner and thinner liquid film between them, as shown in figure 4.14 for two different misorientations. An interesting question is now whether the liquid film is stable or unstable, hence whether it is energetically preferable to keep a liquid film in between a solid-solid grain boundary or not. This question is of importance since having a liquid film between two solids affects the elastic properties of the macroscopic body.

In this subsection, a phenomenological model from Rappaz, Jacot and Boettinger [78] for the contact potential between two grain boundaries is presented. It depends on the grain boundary energy and distinguishes in general between attractive and repulsive grain boundaries. Grain boundaries, whose grain boundary energy is larger than twice the solid liquid interface energy are expected to be repulsive or “wet” grain boundaries, whereas grain boundaries with $\gamma_{GB} < 2\gamma_{SL}$ are expected to be attractive or “dry”.

The model is schematically demonstrated in figure 4.18. As the two solids are well separated by a liquid of width X , where X is much larger than the interface width δ , the interfaces do not interact and the energy costs of such a “grain boundary” corresponds to twice the solid-liquid interface energy. As the interfaces approach each other, they start to interact and the interaction can be described by an interaction potential $\gamma(X)$, which depends on the width of the liquid layer. As the two solids continue to approach each other, the liquid interface width X goes to zero and the energy corresponds to the grain boundary energy γ_{GB} .

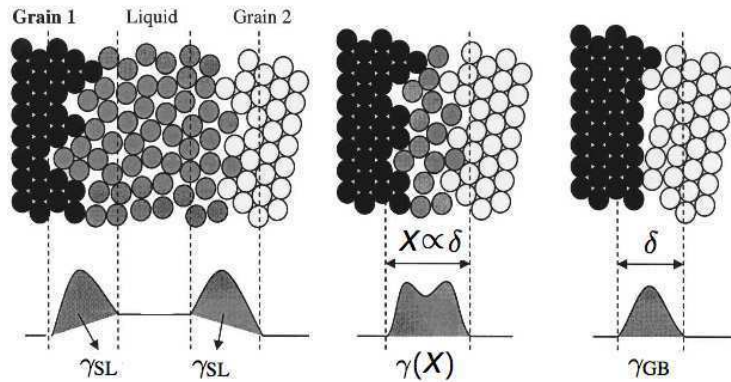


Figure 4.18: Schematics of two solid grains separated by a liquid film of width X . As the two solids approach each other, they start to interact. The interaction potential can be written as $\gamma(X)$, with the two limiting values $2\gamma_{SL}$ for large X and γ_{GB} for $X \rightarrow 0$. From [78].

Since the solid order decays exponentially into the liquid, as a first approximation the interaction potential can be estimated as [78]

$$\gamma(X) = 2\gamma_{SL} + (\gamma_{GB} - 2\gamma_{SL}) \exp(-X/\delta). \quad (4.26)$$

The free energy of a system with two differently orientated solid phases with a liquid film of width X in between can then be written as

$$\mathcal{F}L_x = \mathcal{F}_S(\bar{\psi}_S)(L_x - X) + \mathcal{F}_L(\bar{\psi}_L)X + \varepsilon e^{-X/\delta},$$

where $\bar{\psi}_L$ is the value of ψ in the liquid phase and $\bar{\psi}_S$ is the average over ψ in a unit cell of the solid. Here, the constant term has been neglected and $\varepsilon = (\gamma_{GB} - 2\gamma_{SL})$. The total system is assumed to be translationally invariant parallel to the interface. Its length perpendicular to the interface is L_x , the length of the solid phases is therefore $L_x - X$.

To add the constraint of the lever rule

$$\bar{\psi}L_x = \bar{\psi}_S(L_x - X) + \bar{\psi}_L X, \quad (4.27)$$

one can use a Lagrange multiplier μ and obtain

$$\mathcal{F}L_x = \mathcal{F}_S(\bar{\psi}_S)(L_x - X) + \mathcal{F}_L(\bar{\psi}_L)X - \mu [\bar{\psi}_S(L_x - X) + \bar{\psi}_L X - \bar{\psi}L_x] \varepsilon e^{-X/\delta}.$$

Minimizing the free energy with respect to the liquid layer width X leads to

$$L_x \frac{d\mathcal{F}}{dX} = -\mathcal{F}_S + \mathcal{F}_L + \mu\bar{\psi}_S - \mu\bar{\psi}_L - \frac{\varepsilon}{\delta} e^{-X/\delta} = 0,$$

which can be written as

$$\mathcal{F}_S - \mathcal{F}_L = \mu(\bar{\psi}_S - \bar{\psi}_L) - \frac{\varepsilon}{\delta} e^{-X/\delta}. \quad (4.28)$$

Minimizing the free energy with respect to $\bar{\psi}_S$ and $\bar{\psi}_L$ gives

$$\begin{aligned} L_x \frac{d\mathcal{F}}{d\bar{\psi}_S} &= \frac{d\mathcal{F}_S(\bar{\psi}_S)}{d\bar{\psi}_S} (L_x - X) - \mu(L_x - X) = 0, \text{ and} \\ L_x \frac{d\mathcal{F}}{d\bar{\psi}_L} &= \frac{d\mathcal{F}_L(\bar{\psi}_L)}{d\bar{\psi}_L} X - \mu X = 0, \end{aligned}$$

so that

$$\mu = \frac{d\mathcal{F}_S(\bar{\psi}_S)}{d\bar{\psi}_S} = \frac{d\mathcal{F}_L(\bar{\psi}_L)}{d\bar{\psi}_L}. \quad (4.29)$$

With Eqs. (4.27), (4.28), and (4.29) one has four equations for the unknowns X , $\bar{\psi}_S$, $\bar{\psi}_L$ and μ . The system is therefore fully determined and can be solved numerically. Note that $\bar{\psi}_S$ and $\bar{\psi}_L$ are now functions of X and μ , while for the case without interaction they are constants as given in the phase diagram.

One is now in the position to test the model presented above. Simulations are performed as shown in figure 4.14, where increasing $\bar{\psi}$ forces two solid grains to approach each other. The chemical potential μ and the density in the solid $\bar{\psi}_S$ can be obtained directly from the simulation. The average density $\bar{\psi}_L$ is not well defined when the two grains are very close together but can be defined via the dependence on the chemical potential. In the liquid, $\bar{\psi}_L$ is known as function of $\bar{\psi}$ as well as the chemical potential $\mu_L = \partial_{\bar{\psi}} \mathcal{F}_L$. Defining $\bar{\psi}_L(\mu)$ then allows to use the lever rule to define a $X(\mu) = \frac{\bar{\psi} - \bar{\psi}_S}{\bar{\psi}_L(\mu) - \bar{\psi}_S} L_x$.

If the theory and the simulation results agree well, one will be able to fit the theory to the simulation results and obtain values for ε and δ which are

independent of the system size. This is done plotting $\mu - \mu_{Eq}$ for different system lengths L_x versus the average density $\bar{\psi}$. The numerical data is then fitted with a least square fit, solving the equations above numerically. The numerical data is shown in open symbols in figure 4.19, as well as the fit which is plotted with lines. The obtained values for ε and δ are also given. One can see that the agreement is very good, the fitted values of $\varepsilon \approx 0.0045$ agree well with $\varepsilon = \gamma_{GB} - 2\gamma_{SL} = 0.0043$, independent of the system size. The fitted interface widths $\delta \approx 13.3$ are comparable with the width of a solid-liquid interface, which can be obtained from a plot like figure 4.5 and is given as $\delta \approx 12.5$. The green vertical line in all figures represents the equilibrium value of $\bar{\psi}_S$, it divides the coexistence region from the solid one.

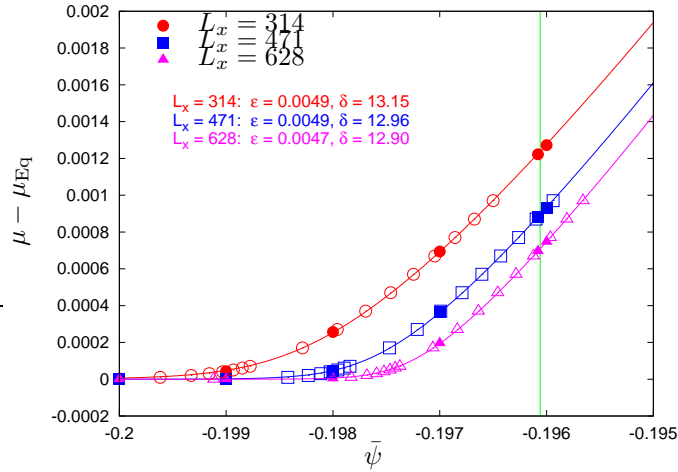


Figure 4.19: $\mu - \mu_{Eq}$ for a high-angle grain boundary with a misorientation of 32.2° . The fitted values of ε agree well with $\gamma_{GB}(\text{saturated}) - 2\gamma_{SL} = 0.0043$. The same is true for the values of δ which are in good agreement with the interface width of $\delta = 12.5$.

In figure 4.20, the liquid layer width X divided by the system length L_x is shown, also for different system lengths and compared with the theory. One can see nicely how the liquid layer width follows the lever rule (solid black line) as the interfaces are well separated and then deviates to larger values, showing the repulsive behavior.

In figures 4.21 and 4.22, the relative chemical potential and the interface width are shown as functions of the average density $\bar{\psi}$ for a low-angle grain boundary. One can see that μ becomes smaller than μ_{Eq} for some values of $\bar{\psi}$. Also the liquid layer width falls below the lever rule. Both properties are expected for attractive grain boundaries. For even larger values of $\bar{\psi}$, X becomes larger than the lever-rule value and $\mu > \mu_{Eq}$, again a repulsive behavior.

As the misorientation becomes smaller, the dislocations become further separated and instead of having a liquid film between the two solids, one rather observes liquid pools around the dislocation cores, as shown in figure 4.14. Here, the theory starts to fail and the agreement with the simulation gets worse.

To obtain a better understanding of what is happening, it is useful to obtain

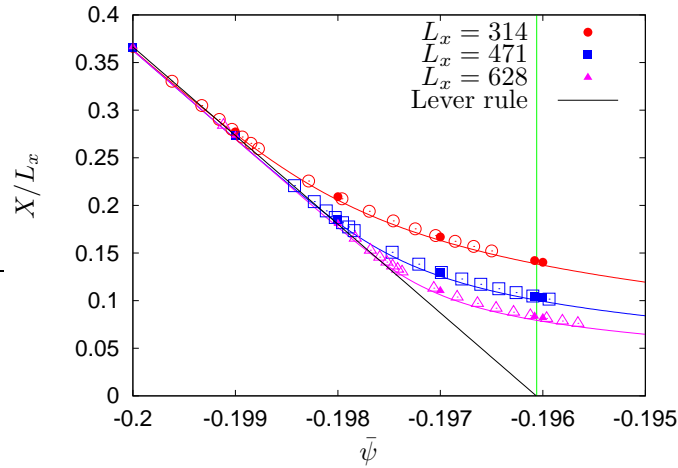


Figure 4.20: The width of the liquid phase X divided by the total length L_x is shown for a misorientation of 32.2° . The simulation results are given with the symbols while the lines represent the results as obtained by the theory. One can nicely see how X deviates from the lever rule towards larger values as the two interfaces interact, showing the repulsive behavior.

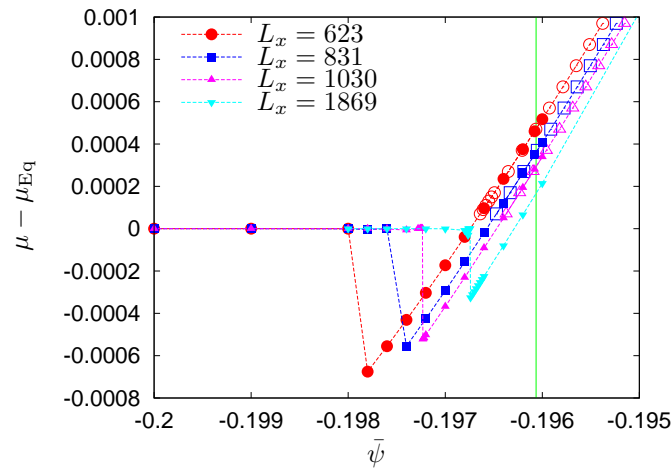


Figure 4.21: $\mu - \mu_{Eq}$ for a low-angle grain boundary with a misorientation of 6° . For low-angle grain boundaries, the phenomenological model fails and is therefore not shown in this figure. One can see that the chemical potential falls below its equilibrium value as the two interfaces interact, showing attractive behavior. For even larger values of $\bar{\psi}$, it represents the repulsive nature again.

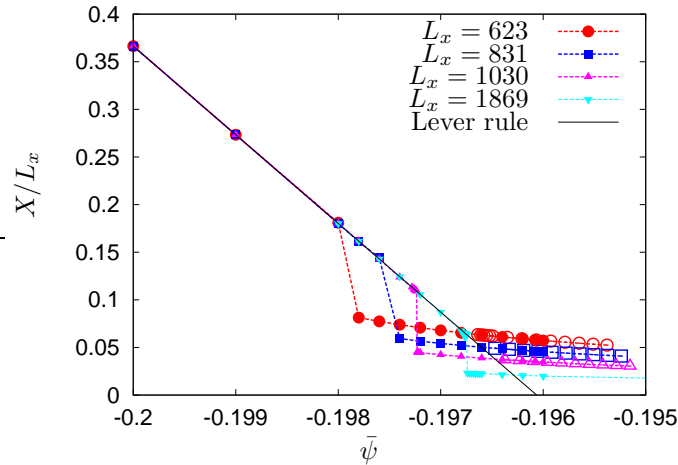


Figure 4.22: The width of the liquid phase X divided by the total length L_x is shown for a low-angle grain boundary with a misorientation of 6° . The simulation results are given with the symbols for different system lengths. As the two interfaces interact, X drops below the lever-rule value, showing that the interaction potential is attractive here. For larger $\bar{\psi}$, the behavior changes again, the interaction potential becomes repulsive.

the contact potential numerically. The contact potential can be obtained by writing down the grand potential in terms of the interface width X

$$\Omega(X) = \Omega_S(L_x - X) + \Omega_L X + 2\gamma_{SL} + V(X)$$

and minimizing with respect to X gives

$$0 = \Omega_L - \Omega_S + V'(X)$$

or

$$\begin{aligned} V'(X) &= \Omega_S - \Omega_L \\ &= f_S(\bar{\psi}_S) - \mu\bar{\psi}_S - f_L + \mu\bar{\psi}_L. \end{aligned}$$

Knowing the free energies f_S and f_L as well as the relations between μ and $\bar{\psi}$ for solid and liquid, one can invert them to obtain an expression for $\bar{\psi}_S(\mu)$ and $\bar{\psi}_L(\mu)$ respectively. This then leads to an expression for $V'(\mu)$, without using explicit information of about the system size or the grain boundary.

With the knowledge of $X(\bar{\psi})$ and $\mu(\bar{\psi})$ as shown in figures 4.20 and 4.19, one can obtain $V'(X)$ and integrate it to $V(X)$. This contact potential is shown in figure 4.23 for two different systems. A high-angle grain boundary is shown in red, where the liquid is rather homogeneous between the solids and the model by Rappaz [78] holds, one can see that the agreement between the simulation data (open points) and $\gamma(X)$ with the values of ε and δ as obtained from the grain boundary energy and the interface width (lines) is very good. For a low-angle grain boundary, the contact potential is shown in blue. One can see that the agreement is rather poor, even qualitatively there are differences. For intermediary values of X , the contact potential becomes negative and hence “attractive”.

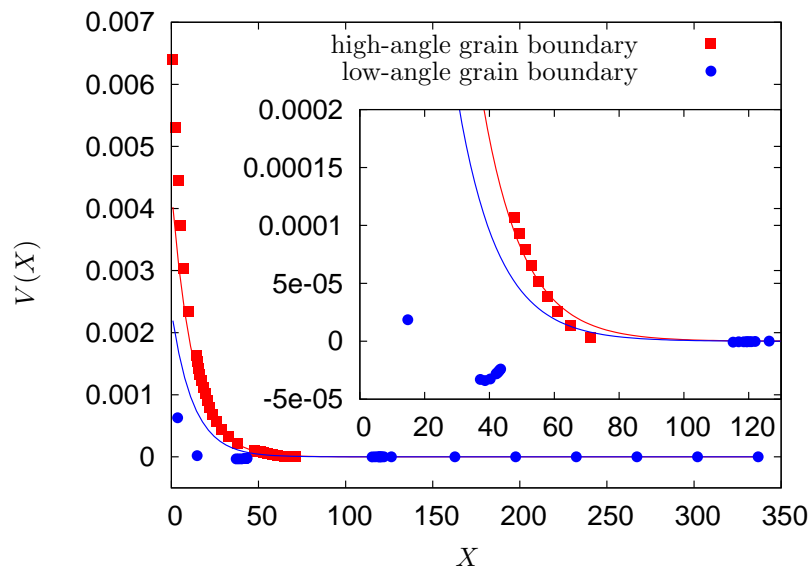


Figure 4.23: Contact potential for an high-angle and a low-angle grain boundary compared to the theory by Rappaz et al. [78]. For high-angle grain boundaries the simulations agree well with the theory, whereas for low-angle grain boundaries it fails.

4.4 Summary and conclusion

In this chapter, grain boundaries have been studied in great detail with a phase field crystal model. It has been shown that grain boundaries of different misorientations can be created and investigated for different values of the average density $\bar{\psi}$. In this work, three aspects are of special interest.

Firstly, it has been investigated how grain boundaries are formed and how an order parameter can be defined in them. In a solid-liquid system, the order decays from the solid phase into the liquid phase over the distance of a few atomic layers, which is in perfect agreement with theory and experiments. In a solid-solid system, one can also define an order which then is reduced inside the grain boundary. The orientation is constant where the order is high and varies in the region where the order is reduced.

In the second part, the structure of the grain boundary has been investigated. It has been shown that the grain boundary can be seen as a line of dislocations for small misorientations. Then, the dislocations are well separated. The grain boundary energy has been obtained and compared with the Read-Shockley theory and a very good agreement was found for low-angle grain boundaries. For large misorientations, the dislocations overlap and the Read-Shockley theory fails, as predicted. The grain boundary energy has been calculated for different values of $\bar{\psi}$ and radius r_0 as appearing in the Read-Shockley theory has been determined in dependence of $\bar{\psi}$.

In a third part, the formation of grain boundaries has been investigated further. During the solidification process, the liquid film remaining between grains

of the same or different orientation can affect the elastoplastic properties of the macroscopic body crucially. It is important to know whether the liquid film is stable or unstable, hence whether the grain boundary is wet or dry. A phenomenological model by Rappaz, Jacot and Boettinger [78] has been presented, which divides the grain boundary in attractive and repulsive grain boundaries. The theory has been tested and was found to hold for high-angle grain boundaries, while for low-angle grain boundaries, the description of a homogeneous liquid film between the two grains fails. It has been shown that there are pools of liquid around the dislocation cores, which seem to attract each other. The contact potential has been determined numerically for a high- and a low-angle grain boundary and it has been shown that the low-angle grain boundaries are not monotonously repulsive or attractive, but attractive at larger distances while repulsive on shorter ones.

It is very interesting to continue this work and go to even smaller misorientations to obtain grain boundaries that are really attractive. For the moment, the only problem in doing so is the computation time: small misorientations consist of dislocations which are separated by a large distance and hence large systems are needed. It is also interesting to investigate the transition between the low-angle and high-angle regime and how it depends on the interface width δ . This can be done by varying the normalized temperature r .

Chapter 5

Phase-Field Model for Polycrystals

The solidification of an anisotropic alloy from its melt is well understood and appropriate numerical models exist. In this work, the question is raised how two or more crystals with different local crystalline orientation interact. The formation and the evolution of grain boundaries is investigated, generalizing the phase-field model for single crystals to include the local crystalline orientation.

In section 2.3, the standard phase-field model for the solidification of a pure substance with only one local crystalline orientation has been presented, as well as two ways of generalizing the model to polycrystals. In this chapter, a different model is developed and tested.

This chapter is organized as follows. Based on the properties of polycrystals as presented in section 2.1, a phenomenological free energy is derived in section 5.1, which is then used to obtain the set of equations of motion for the solidification of a polycrystal. In section 5.2, the model is tested for stability and it is discussed whether the simulation results correspond to the underlying physics. Some problems are pointed out and their importance is investigated. Finally, some results of the simulation of polycrystalline solidification are presented. In section 5.3, the model properties are summarized and some propositions for the further development are outlined.

5.1 Phase-field model

To develop a model which describes the solidification of crystals with different crystalline orientations θ , the already existing and well explored model for the solidification of an anisotropic monocrystal, as introduced in section 2.3.1, is generalized. The two phases solid and liquid are given by a phase-field variable ϕ , here with $\phi = 1$ in the solid and $\phi = 0$ in the liquid phase. For the crystalline orientation, an extra orientation field θ is introduced. A grain boundary is then given by a change in the orientation field, while the orientation is constant in the different grains. As seen in section 4.3.1, the change in the orientation is accompanied by a lowered crystalline order, which is in this model represented by a decrease in the phase field ϕ .

In section 5.1.1, a phenomenological free energy including both fields, ϕ and θ , is developed. An important aspect of the model is the anisotropy of the surface energy due to the crystalline structure, which is introduced in section 5.1.2. It depends on the orientation field θ and has to be included in the free energy. In section 5.1.3, it is shown how the equations of motion can be obtained by minimizing the free energy with time by taking the functional derivative. Finally, the model parameters are related to physical quantities in section 5.1.4.

5.1.1 Free energy

Since the physics is invariant under a global rotation, the free energy cannot depend on the crystalline orientation θ explicitly, but on its gradients only. The lowest order gradient term obtained from a Landau expansion is $(\nabla\theta)^2$. In the following, the precise form of the free energy is derived.

The first part of the free energy is identical to the standard free energy of phase-field models for solid-liquid phase transitions, as explained in section 2.3.1. It consists of a gradient term, a double well potential $f(\phi)$ and a coupling function $g(\phi)$, which allows to shift the minima in the double well for the phases

solid and liquid according to the normalized temperature u , using the coupling parameter λ . The second part is here given most generally as the lowest order gradient term $(\nabla\theta)^2$, coupled with a coupling constant ν and a coupling function $\tilde{g}(\phi)$. The free energy can then be written as

$$\mathcal{F} = \int \left[\frac{1}{2} W^2 (\nabla\phi)^2 + f(\phi) + u\lambda g(\phi) + \nu\tilde{g}(\phi)(\nabla\theta)^2 \right] dV. \quad (5.1)$$

The function $\tilde{g}(\phi)$ has to take into account the different energy costs in the solid and the liquid phase. The orientational variable θ is defined in the entire system, even in the liquid phase where it has no physical meaning. Therefore, the coupling function $\tilde{g}(\phi)$ has to ensure that angle variations in the liquid do not lead to an increase in the free energy and hence $\tilde{g}(\phi = 0)$ has to vanish.

The explicit form of $\tilde{g}(\phi)$, especially in the limit $\phi \rightarrow 1$, is crucial for the model and is discussed in the following. To point out the problem, a finite value for $\tilde{g}(\phi = 1)$ is assumed and two simple limiting cases are discussed. In both cases, the orientation is fixed at the left and right boundary of the system to a value θ_1 and θ_2 , respectively. The effect of the phase field is for the moment neglected, ϕ can be assumed to be constant. In the first example, shown in figure 5.1 a), the crystalline orientation varies rapidly in a localized region of width W and is constant in the rest of the system. The free energy is given by $\mathcal{F}_\theta \propto W \left(\frac{\theta_2 - \theta_1}{W} \right)^2$. The opposite behavior, shown in figure 5.1 b), is a continuous variation over the entire system length L , leading to a free energy of $\mathcal{F}_\theta \propto L \left(\frac{\theta_2 - \theta_1}{L} \right)^2$. In the limit of large systems, $L \rightarrow \infty$, for a given value of W and a finite coupling function $\tilde{g}(\phi)$, the continuous case is always energetically favorable.

This remains true if one allows ϕ to vary in the grain boundary. The most extreme variation of ϕ is to put it to zero in the interface. Then, the orientation can vary without increasing the energy, but a finite energy contribution arises from the change in ϕ , basically forming two solid-liquid interfaces. This finite energy, which is independent of the system size, again becomes larger than the continuous deformation for systems above a certain critical length.

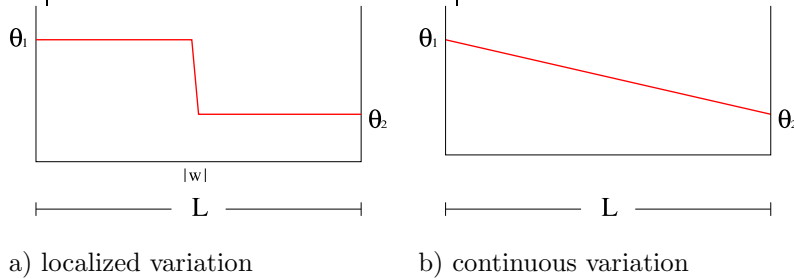


Figure 5.1: Examples for a possible variation of the crystalline orientation θ . In a), the localized case is shown, where θ is constant in the entire system but in a small region W , where it varies rapidly. In b), the opposite behavior is shown. The orientation varies continuously over the entire system length L .

A possible way to circumvent this problem is to introduce a second, non-analytical gradient term $\propto |\nabla\theta|$, as demonstrated in section 2.3.3. Here, another

approach is developed, namely to use the standard second order gradient term only but with a singular coupling function $\tilde{g}(\phi)$, which tends to infinity in the solid phase.

Form of coupling function

As mentioned before, the explicit form of \tilde{g} turns out to be crucial for the existence of localized grain boundaries. In the following, it is investigated for which functions of \tilde{g} grain boundaries remain stable.

Most generally, with the two limits $\tilde{g}(\phi \rightarrow 0) \rightarrow 0$ and $\tilde{g}(\phi \rightarrow 1) \rightarrow \infty$, a form $\tilde{g}(\phi) = \frac{\tilde{g}_1(\phi)}{(1-\phi)^\alpha}$ is assumed, where α is some positive real exponent and \tilde{g}_1 is a polynomial in ϕ . At equilibrium ($u = 0$, $\delta\mathcal{F}/\delta\theta = 0$, $\delta\mathcal{F}/\delta\phi = 0$), one obtains for a one-dimensional system:

$$0 = \partial_x [\tilde{g}(\phi)\partial_x\theta], \quad (5.2)$$

$$0 = -f'(\phi) + W^2\partial_{xx}\phi - \tilde{g}'(\phi)(\partial_x\theta)^2. \quad (5.3)$$

From Eq. (5.2), it follows that at equilibrium $\tilde{g}(\phi)\partial_x\theta = A$, where A is a constant to be determined. With this expression, Eq. (5.3) can be written as

$$W^2\partial_{xx}\phi = f'(\phi) + \tilde{g}'(\phi)\frac{A^2}{\tilde{g}(\phi)^2} = -\frac{d}{d\phi} \left[-f(\phi) + \frac{A^2}{\tilde{g}(\phi)} \right]. \quad (5.4)$$

Replacing x by t and ϕ by y , one has the equation of a particle moving in a potential $V_{\text{eff}} = -f(\phi) + A^2/\tilde{g}(\phi)$. The localized grain boundary solution then corresponds to the trajectory of a particle that starts with zero velocity at $y = 1$, goes to $y = y_0$ in an infinite time and comes back. The infinite duration of the trajectory leads to the requirement that V_{eff} has a maximum at $\phi = 1$, hence

$$\frac{dV_{\text{eff}}}{d\phi} = -f'(\phi) + A^2 \left[-\alpha(1-\phi)^{\alpha-1} \left(\frac{1}{\tilde{g}_1} \right) + (1-\phi)^\alpha \left(\frac{1}{\tilde{g}_1} \right)' \right] = 0 \quad (5.5)$$

$$\begin{aligned} \frac{d^2V_{\text{eff}}}{d\phi^2} &= -f''(\phi) + A^2 \left[\alpha(\alpha-1)(1-\phi)^{\alpha-2} \left(\frac{1}{\tilde{g}_1} \right) - 2\alpha(1-\phi)^{\alpha-1} \left(\frac{1}{\tilde{g}_1} \right)' \right. \\ &\quad \left. + (1-\phi)^\alpha \left(\frac{1}{\tilde{g}_1} \right)'' \right] < 0, \end{aligned} \quad (5.6)$$

For $f(\phi) = \phi^2(\phi-1)^2$ as used in this work, the first and second derivatives of the double well potential at $\phi = 1$ are given by $f'(\phi = 1) = 0$ and $f''(\phi = 1) = 2$. From Eq. (5.5), it follows immediately that $\alpha > 1$. From Eq. (5.6), one can see that a solution exists for $\alpha = 2$ only for appropriate values of A , and always for $\alpha > 2$. In figure 5.2, the effective potential is shown for different values of α , where for simplicity $A = 1$ and $\tilde{g}_1(\phi) = 1$ are chosen.

Another requirement on the form of \tilde{g} is that the energy of a system with continuous orientation variation and constant ϕ tends to a limit value larger than zero as L goes to infinity.

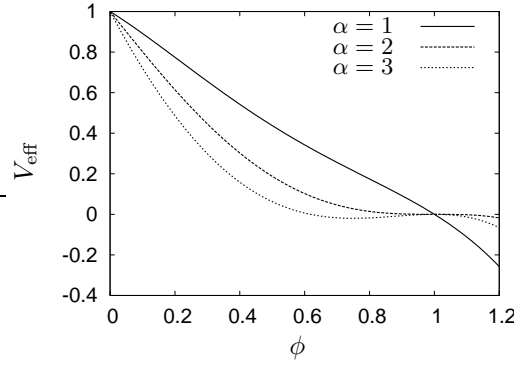


Figure 5.2: The effective potential V_{eff} is shown for different values of α , where for simplicity $A = 1$ and $\tilde{g}_1(\phi) = 1$ are chosen. For $\alpha = 2$, $\phi = 1$ is extremal.

In an homogeneous system, the phase-field variable is constant and close to 1, $\phi = \phi_0 \equiv 1 - \phi_1$ with $\phi_1 \ll 1$. The gradient of θ can be written as $(\nabla\theta)^2 = (\Delta\theta/L)^2$ and the free energy can be expressed in terms of ϕ_1 as

$$\mathcal{F} = L \left[\phi_1^4 - 2\phi_1^3 + \phi_1^2 + \left(\frac{\Delta\theta}{L} \right)^2 \frac{\tilde{g}_1(\phi_1)}{\phi_1^\alpha} \right]. \quad (5.7)$$

The still unknown function \tilde{g}_1 has to remain at a non-zero value as $\phi_1 \rightarrow 0$ and can therefore be written in lowest order as $\tilde{g}_1(\phi_1) = 1 + \mathcal{O}(\phi_1)$.

For the free energy, it follows, also to lowest order in ϕ_1 ,

$$\mathcal{F} \approx L \left[\phi_1^2 + \left(\frac{\Delta\theta}{L} \right)^2 \phi_1^{-\alpha} \right]. \quad (5.8)$$

Searching for ϕ_1 that minimizes the free energy, $\partial\mathcal{F}/\partial\phi_1 = 0$, leads to

$$\phi_1 = \left(\frac{\alpha}{2} \right)^{\frac{1}{\alpha+2}} \left(\frac{\Delta\theta}{L} \right)^{\frac{2}{\alpha+2}}. \quad (5.9)$$

Not being interested in the proportionality constant, the prefactor is neglected and the rest is inserted back into the free energy from Eq. (5.8), which gives

$$\mathcal{F} \propto L \left[\left(\frac{\Delta\theta}{L} \right)^{\frac{4}{\alpha+2}} \right].$$

To obtain a length-independent free energy to the lowest order in ϕ_1 , one can see that $\alpha = 2$.

With this choice, it is ensured that the free energy for $L \rightarrow \infty$ approaches a finite value, independent of the form of $\tilde{g}_1(\phi)$. For smaller lengths, however, the free energy depends on L . To prevent the system from forming spontaneous grain boundaries, it is necessary that the free energy increases as L is decreased and hence that the constant value is approached from above, as shown in figure 5.3.

To investigate the behavior for smaller (but still large) L , the expansion is extended to the next order. With

$$\phi_1 \approx \left(\frac{\Delta\theta}{L}\right)^{\frac{1}{2}} + \tilde{\phi}_1, \quad (5.10)$$

one has $\tilde{g}_1(\phi_1) = 1 + b\phi_1$. Minimizing the free energy with respect to ϕ_1 gives

$$0 = 2\phi_1^4 - 6\phi_1^5 + \left(\frac{\Delta\theta}{L}\right)^2 (2 - b\phi_1), \quad (5.11)$$

taking into account the first two leading orders in ϕ_1 . Inserting Eq. (5.10) in Eq. (5.11) gives

$$(b+6) \left(\frac{\Delta\theta}{L}\right)^{5/2} = \tilde{\phi}_1 \left[8 \left(\frac{\Delta\theta}{L}\right)^{3/2} - (30+b) \left(\frac{\Delta\theta}{L}\right)^2 \right]. \quad (5.12)$$

Since $\Delta\theta/L$ is small, one can neglect the terms of order $(\Delta\theta/L)^2$ in the square brackets and solve for $\tilde{\phi}_1$, leading to $\tilde{\phi}_1 = \frac{b+6}{8} \left(\frac{\Delta\theta}{L}\right)$. Inserting

$$\phi_1 \approx \left(\frac{\Delta\theta}{L}\right)^{\frac{1}{2}} + \frac{b+6}{8} \left(\frac{\Delta\theta}{L}\right) \quad (5.13)$$

back into the free energy and neglecting terms of order $\left(\frac{\Delta\theta}{L}\right)^2$ and higher, gives

$$\mathcal{F} = 2\Delta\theta + (b-2) \left(\frac{(\Delta\theta)^{3/2}}{\sqrt{L}}\right).$$

Requiring that the energy approaches the limiting value from above gives $b > 2$. Please note that the coupling function $\tilde{g}_1(\phi_1) = 1 + b\phi_1$ is expressed in terms of $\phi_1 = 1 - \phi$.

To obtain an expression for $\tilde{g}_1(\phi)$, one should remember that $\tilde{g}_1(\phi)$ has to vanish for $\phi = 0$. In addition, one can normalize $\tilde{g}_1(\phi = 1) = 1$, leading to the form

$$\tilde{g}_1(\phi) = a\phi^{\alpha_0} - (a-1)\phi^{\alpha_0+1}, \quad (5.14)$$

with unknown constant a and exponent α_0 .

Forgetting about the singular behavior of \tilde{g} in $\phi = 1$, the results of Karma-Kessler-Levine [79] about modeling of crack propagation lead to choose $\alpha_0 > 2$. Choosing $\alpha_0 = 2$ would lead to singular behavior of θ in the middle of the grain boundary and to strong pinning of the grain boundary on grid points, so that $\alpha_0 = 3$ is taken in this work.

To obtain a , one uses Eq. (5.14) to get $\tilde{g}_1(\phi = 1 - \phi_1) = 1 + (a-4)\phi_1 + \mathcal{O}(\phi_1^2)$. One can identify $a - 4 = b > 2$ and obtain $a > 6$.

With all these considerations and choosing $a = 7$, the singular coupling function can be written as

$$\tilde{g}(\phi) = \frac{7\phi^3 - 6\phi^4}{(1-\phi)^2}. \quad (5.15)$$

The other coupling functions are given as $f(\phi) = \phi^2(\phi - 1)^2$ and $g(\phi) = 10\phi^3 - 15\phi^4 + 6\phi^5$, leading to the free energy

$$\mathcal{F} = \int \left[\frac{1}{2} W^2 (\nabla \phi)^2 + \phi^2 (\phi - 1)^2 + u \lambda (10\phi^3 - 15\phi^4 + 6\phi^5) + \nu \frac{7\phi^3 - 6\phi^4}{(1 - \phi)^2} (\nabla \theta)^2 \right] dV, \quad (5.16)$$

with gradient constant W , dimensionless temperature u and coupling constants λ and ν .

The free energy for a homogeneous system is shown in figure 5.3 as a function of the system length. One can see that it approaches a constant value for large system lengths from above and that it has a maximum at L_C . For lengths larger than L_C , the homogeneous solution is stable, while for $L < L_C$ the homogeneous solution is unstable and grain boundaries form spontaneously.

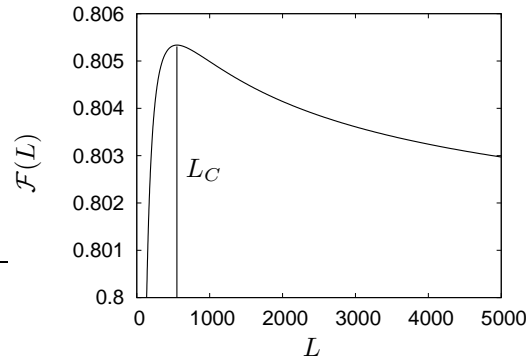


Figure 5.3: The free energy of a homogeneous system is shown in dependence of the system length L . The energy approaches a constant value for large L from above. The maximum at $L = L_C$ prevents spontaneous grain boundaries formation. For small L , however, grain boundaries are not stable anymore.

Even if the idea of having a singular coupling function appears to be unnatural, it can be motivated by physical considerations. In the liquid, the orientation is described as more or less random, so that an angle gradient does not lead to an increase in the free energy. In the solid, however, changing the orientation corresponds to a deformation of the crystal. The energy of a deformation in a solid is orders of magnitude larger than in a liquid, which is taken into account in the model by the coupling function which diverges in the solid phase.

5.1.2 Anisotropy

The surface energy of a crystalline material depends on the interface orientation with respect to the crystalline orientation θ . While in section 2.3.1 the interface normal is expressed in terms of an angle Θ , here it is more convenient to express it in terms of the interface normal \vec{n} . The interface normal can be obtained from

the gradient of the phase field ϕ as

$$\vec{n} = \frac{1}{\sqrt{(\partial_x \phi)^2 + (\partial_y \phi)^2}} \begin{pmatrix} \partial_x \phi \\ \partial_y \phi \end{pmatrix}. \quad (5.17)$$

For a single crystal with a cubic lattice, whose crystalline structure is taken to be aligned parallel to the coordinate system, a fourfold anisotropy $W(\vec{n})$ can be written as [39]

$$W(\vec{n}) = W_0 \bar{a}_s [1 + \epsilon(n_x^4 + n_y^4)]. \quad (5.18)$$

The strength of the anisotropy is characterized by a parameter ϵ_4 , which determines $\bar{a}_s = 1 - 3\epsilon_4$ and $\epsilon = \frac{4\epsilon_4}{1-3\epsilon_4}$.

For polycrystals, one cannot align the crystalline lattice parallel to the coordinate system since they consist of several single crystals with different orientations. To be able to describe polycrystals, one has to generalize the anisotropy from Eq. (5.18) to include the local orientation θ . This can be performed by allowing a rotation of the crystalline reference axes by the orientation angle θ . The unit vectors of the interface direction then become $n_x \rightarrow n_x \cos(\theta) + n_y \sin(\theta)$ and $n_y \rightarrow -n_x \sin(\theta) + n_y \cos(\theta)$. It then follows that

$$\begin{aligned} W(\vec{n}, \theta) &= W_0 \bar{a}_s \left\{ 1 + \frac{\epsilon}{[(\partial_x \phi)^2 + (\partial_y \phi)^2]^2} \left[\frac{3}{4} ((\partial_x \phi)^4 + (\partial_y \phi)^4 + 2(\partial_x \phi)^2 (\partial_y \phi)^2) \right. \right. \\ &\quad + \frac{1}{4} ((\partial_x \phi)^4 + (\partial_y \phi)^4 - 6(\partial_x \phi)^2 (\partial_y \phi)^2) \cos(4\theta) \\ &\quad \left. \left. + ((\partial_x \phi)^3 (\partial_y \phi) - (\partial_x \phi) (\partial_y \phi)^3) \sin(4\theta) \right] \right\}. \end{aligned} \quad (5.19)$$

5.1.3 Equations of motion

The equations of motion for the different fields are given by the minimization of the free energy $\tau \partial_t \phi = -\frac{\delta F}{\delta \phi}$ and $\tau_\theta \partial_t \theta = -\frac{\delta F}{\delta \theta}$, leading to

$$\begin{aligned} \partial_t \phi &= 1/\tau \{ -4\phi^3 + 6\phi^2 - 2\phi + \lambda u(-30\phi^2 + 60\phi^3 - 30\phi^4) \\ &\quad + W(\vec{n}, \theta)^2 [(\partial_{xx} \phi) + (\partial_{yy} \phi)] \\ &\quad + 2W(\vec{n}, \theta) [(\partial_x W(\vec{n}, \theta))(\partial_x \phi) + (\partial_y W(\vec{n}, \theta))(\partial_y \phi)] \\ &\quad + \partial_x \left[((\partial_x \phi)^2 + (\partial_y \phi)^2) W(\vec{n}, \theta) \frac{\partial W(\vec{n}, \theta)}{\partial (\partial_x \phi)} \right] \\ &\quad + \partial_y \left[((\partial_x \phi)^2 + (\partial_y \phi)^2) W(\vec{n}, \theta) \frac{\partial W(\vec{n}, \theta)}{\partial (\partial_y \phi)} \right] \\ &\quad - \nu \tilde{g}'(\phi) [(\partial_x \theta)^2 + (\partial_y \theta)^2] \} \end{aligned} \quad (5.20)$$

and

$$\begin{aligned} \tau_\theta \partial_t \theta &= 2\nu \{ \tilde{g}(\phi) [(\partial_{xx} \theta) + (\partial_{yy} \theta)] + \tilde{g}'(\phi) [(\partial_x \phi)(\partial_x \theta) + (\partial_y \phi)(\partial_y \theta)] \\ &\quad - W(\vec{n}, \theta) (\nabla \phi)^2 [\partial_\theta W(\vec{n}, \theta)], \end{aligned} \quad (5.21)$$

where $\tilde{g}(\phi) = \frac{7\phi^3 - 6\phi^4}{(1-\phi)^2}$ and $\tilde{g}'(\phi) = \frac{21\phi^2 - 24\phi^3}{(1-\phi)^2} + \frac{2(7\phi^3 - 6\phi^4)}{(1-\phi)^3}$.

Note that the characteristic time constant τ depends also on the interface orientation, $\tau = \tau_0 \frac{W(\vec{n}, \theta)^2}{W_0^2}$. The time constant τ_θ in the equation of motion for the angle variable turns out to be important and is discussed in section 5.2.2.

The derivatives of $W(\vec{n}, \theta)$, as given in Eq. (5.19), are needed in the equation of motion and can be calculated to

$$\begin{aligned} \frac{\partial W(\vec{n}, \theta)}{\partial(\partial_x \phi)} &= \frac{4W_0\epsilon_4}{[(\partial_x \phi)^2 + (\partial_y \phi)^2]^3} \left\{ 4 \cos(4\theta)(\partial_x \phi)(\partial_y \phi)^2 [(\partial_x \phi)^2 - (\partial_y \phi)^2] \right. \\ &\quad \left. + \sin(4\theta)(\partial_y \phi) [-(\partial_x \phi)^4 + 6(\partial_x \phi)^2(\partial_y \phi)^2 - (\partial_y \phi)^4] \right\}, \\ \frac{\partial W(\vec{n}, \theta)}{\partial(\partial_y \phi)} &= \frac{4W_0\epsilon_4}{[(\partial_x \phi)^2 + (\partial_y \phi)^2]^3} \left\{ 4 \cos(4\theta)(\partial_x \phi)^2(\partial_y \phi) [-(\partial_x \phi)^2 + (\partial_y \phi)^2] \right. \\ &\quad \left. + \sin(4\theta)(\partial_x \phi) [(\partial_x \phi)^4 - 6(\partial_x \phi)^2(\partial_y \phi)^2 + (\partial_y \phi)^4] \right\} \quad \text{and} \\ \partial_\theta W(\vec{n}, \theta) &= \frac{4W_0\epsilon_4}{[(\partial_x \phi)^2 + (\partial_y \phi)^2]^2} \left\{ - [(\partial_x \phi)^4 + (\partial_y \phi)^4 - 6(\partial_x \phi)^2(\partial_y \phi)^2] \sin(4\theta) \right. \\ &\quad \left. + 4 [(\partial_x \phi)^3(\partial_y \phi) - (\partial_x \phi)(\partial_y \phi)^3] \cos(4\theta) \right\}. \end{aligned}$$

Finally, an equation of motion for the dimensionless temperature field u is needed. Assuming that the temperature simply evolves according to the diffusion law, the equation of motion can be written as

$$\partial_t u = D\nabla^2 u + \partial_t \phi, \quad (5.22)$$

where $h(\phi) = 2\phi$ has been chosen, compare section 2.3.1.

5.1.4 Model parameters

In this subsection, a solid-liquid system with constant angle is investigated. Assuming that the crystalline orientation is constant, one can neglect the equation of motion for θ .

For the one-dimensional case with interface in y -direction ($\partial_y \phi = 0$), the anisotropic gradient constant $W(\theta) = W_0 \bar{a}_s \left\{ 1 + \epsilon \left[\frac{3}{4} + \frac{1}{4} \cos(4\theta) \right] \right\}$ and the angle-dependent time constant is chosen as $\tau = \tau_0 \frac{W(\theta)^2}{W_0^2}$. For a given anisotropy (\bar{a}_s, ϵ), crystal orientation θ and diffusion constant D , the remaining model parameters are W_0, τ_0 and λ .

As derived in section 2.3.1, the capillary length is given by $d_0 = a_1 \frac{W_0}{\lambda}$ and the kinetic coefficient as $\beta(\theta) = a_1 \left[\frac{\tau(\theta)}{\lambda W(\theta)} - a_2 \frac{W(\theta)}{D} \right]$.

The constants a_1 and a_2 depend on the functions f and g , and are given as $a_1 = I/J = \frac{1}{3\sqrt{2}}$ and $a_2 = (\mathcal{K} + JF)/I = 2.35$. The integrals $I = \frac{1}{3\sqrt{2}}$, $J = 1$, $F = \frac{\ln 2}{\sqrt{2}}$ and $\mathcal{K} = \frac{47-30\ln(4)}{60\sqrt{2}}$ can be calculated as defined in Eqs. (2.41) to (2.44), where here $\phi_0 = \frac{1}{2}[1 - \tanh(x/\sqrt{2})]$ and $g_0 = g(\phi_0)$. For $\lambda = \frac{D\tau_0}{W_0} \frac{1}{a_2}$, the kinetic coefficient vanishes. With a fixed capillarity length $d_0 = a_1 W_0/\lambda$, the relation between τ_0 and W_0 is given by

$$\tau_0 = a_2 \frac{W_0^2 \lambda}{D} = a_1 a_2 \frac{W_0^3}{D d_0}. \quad (5.23)$$

5.2 Numerical results

With the model derived in section 5.1, one has a set of equations for the phase field ϕ , the local crystalline orientation field θ and the dimensionless temperature u . In this section, the equations of motion as given in Eqs. (5.20), (5.21) and (5.22) are solved numerically and the results are interpreted.

Firstly, the grain boundaries are tested for one-dimensional systems. Starting with an isotropic system, it is shown in section 5.2.1 that localized grain boundaries can be obtained which are independent of system size and discretization. As predicted in the derivation of the free energy, there is a minimal misorientation angle between two grains below which the grain boundary becomes unstable. In other words, for a certain misorientation, undercooling and anisotropy, there is a critical coupling constant ν_c , below which this grain boundary disappears. In section 5.2.2, at the example of a tricrystal, the mobility constant in the equation of motion for the angle field is discussed.

Introducing anisotropy, an artificial interface motion is observed, for solid-liquid interfaces as well as for solid-solid interfaces. This effect is investigated in sections 5.2.3 and 5.2.4. In section 5.2.5, the importance of this effect is determined by keeping the volume of a solid surrounded by its liquid constant. The effect which causes the interface motion leads to a change in the equilibrium temperature, which gives an idea of the magnitude of the correction. For two-dimensional systems with different orientations, the equilibrium shape is determined and compared with the so-called Wulff shape, as introduced in section 2.1. Since the artificial effects are found to be small, in section 5.2.6, the growth of different grains in their liquid is simulated, showing that the model is very well capable of treating polycrystalline solidification.

5.2.1 Stability of the obtained grain boundaries

As described in section 5.1.1, the free energy has to be of a very specific form to allow for stable and localized grain boundaries. In the following, it is tested whether the obtained free energy leads to grain boundaries which are independent of system size and which converge towards the same solution when using a finer numerical grid.

This is investigated for simple quasi one-dimensional systems of two solids with different orientations which are growing towards each other. This is shown in figure 5.4 for isotropic systems with different system lengths. At the left hand side, the orientation angle is initially at $\theta_1 = \pi/20$ and the phase-field variable at $\phi_1 = 1$, placing the system in the solid phase. On the right hand side, $\theta_2 = \pi/4$ and $\phi_2 = 1$, also solid but with a different crystalline orientation. The resulting interface solutions are stable, localized and independent of the system size. In figure 5.5, ϕ and θ in the interface region are enlarged, showing that the grain boundary solution is identical in all three cases. The dependence of the interface solution on the discretization is shown in figure 5.6, demonstrating that the interfaces converge towards a well-defined continuum solution.

As already seen in the derivation of the free energy, the existence of a localized grain boundary depends on the coupling parameter ν . In figure 5.7, the same system is shown for different coupling parameters ν . As one can see, there is a critical coupling parameter ν_c , below which the stable solution disappears. For $\nu < \nu_c$, the grain boundary becomes spread out, accompanied by a decrease of ϕ in the entire system.

The critical coupling parameter depends on the anisotropy ϵ_4 , the undercooling Δ and, most importantly, on the misorientation $\Delta\theta$. For a given ν , there is a smallest possible misorientation below which all grain boundaries disappear. In the following, the dependence of ν_c on the model parameters is investigated. This allows to estimate the smallest misorientations possible in the performed

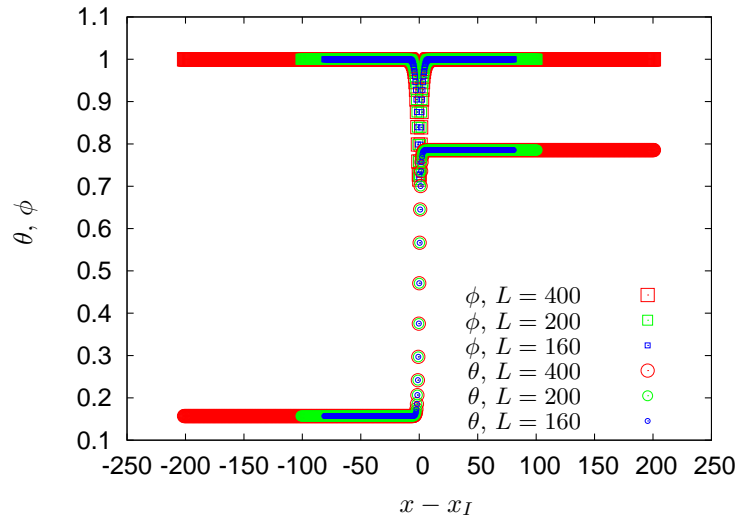


Figure 5.4: One-dimensional system of two solids growing towards each other. For three systems with different system sizes, ϕ and θ are shown at equilibrium, demonstrating the localized solid-solid interfaces being independent of the system size.

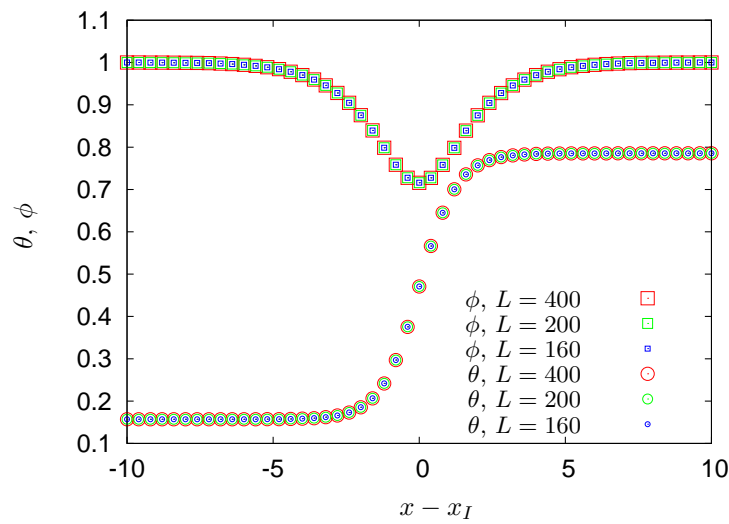


Figure 5.5: Enlargement of interface region from figure 5.4. The solutions are stable and independent of the of the system size.

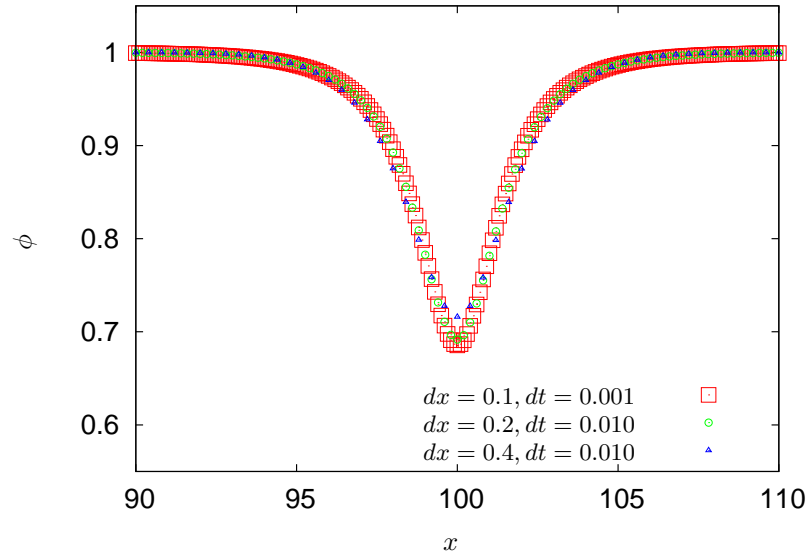


Figure 5.6: One dimensional system of two solids growing towards each other, leading to a solid-solid interface. Here, ϕ is shown in the interface region for different discretizations of the same system. One can see clearly that the different interfaces converge towards the same solution.

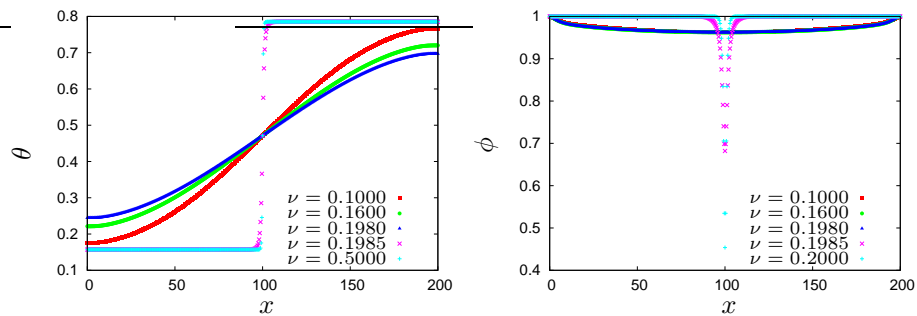


Figure 5.7: The angle variation (left) and the corresponding phase field (right) in a solid-solid interface of fixed misorientation. The orientation in the two solids is initially at $\theta_1 = \pi/20$ and $\theta_2 = \pi/4$. For different values of ν , the interface solutions are shown. Below a critical value of ν , the localized grain boundary disappears (red, green and blue curves).

simulation.

In figure 5.8, the dependencies of ν_c as obtained from numerical simulations are presented. One can see that ν_c is approximately proportional to $\frac{1}{\Delta\theta^2}$ and that it varies linearly with ϵ_4 .

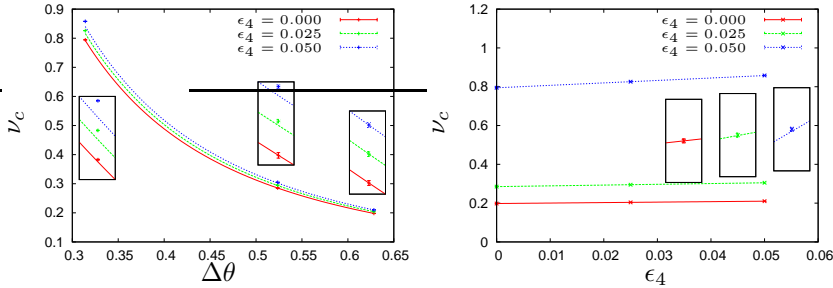


Figure 5.8: The critical value ν_c is shown as a function of the misorientation $\Delta\theta$ for different values of ϵ_4 (left) and as a function of the anisotropy ϵ_4 for different misorientations (right). One can see that ν_c is approximately proportional to $\frac{1}{\Delta\theta^2}$ and that it varies linearly with ϵ_4 .

By using a sufficiently large coupling parameter, one can in principle create grain boundaries with arbitrarily small angle differences. There is, however, a numerical problem. The larger ν , the more localized the interface region becomes, and therefore the smaller is the required discretization. Another way to obtain small angle differences is to decrease the undercooling, which leads to slower growth and longer simulation times.

In figure 5.9, the grain boundary energy for symmetric tilt grain boundaries is shown with open circles in arbitrary units. For comparison, a Read-Shockley like grain boundary energy is fitted to the data. One can see that the obtained grain boundary energy agrees qualitatively well with the Read-Shockley law. However, in this work, no effort is made to relate the grain boundary energy quantitatively to the model parameters and to obtain the correct elastic properties. Still, this qualitative agreement appears automatically from the free energy without manipulating the coupling functions explicitly.

5.2.2 Rotational mobility

Another important question in the models with orientation variable is the time constant τ_θ in the equation of motion for the angle field — the rotational mobility. In the equation of motion for the angle field, τ_θ can be chosen differently according to the physical system which is to be described. In conceptually similar models, it is shown how orientational defects like new grains with different orientation can be frozen into the solid [54] or how grain rotation can be included into the model [80].

While it has been observed that a grain of one orientation surrounded by a grain of another orientation can rotate entirely and change its orientation [81–87], the underlying mechanism is presumably different to the one occurring in this model. A circular shaped grain surrounded by a differently orientated grain most likely reorientates by a rigid-body-like rotation.

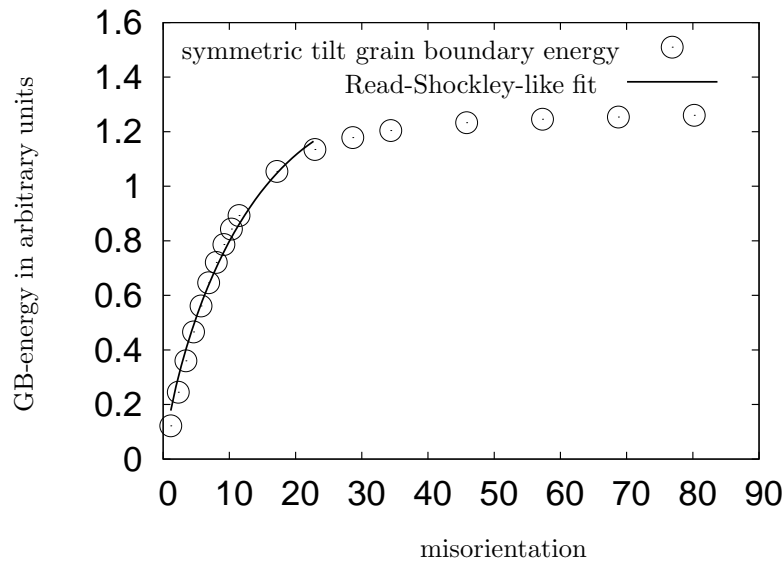


Figure 5.9: Interface energy of a symmetric tilt grain boundary in arbitrary units. As comparison, a Read-Shockley-like grain boundary energy is shown. The simulation results and the theory agree qualitatively well.

For a tricrystal, as shown in figure 5.10, this kind of rotation is not possible. Here, a solid of one orientation is sandwiched between two solids of different orientations. The interfaces are planar and supposed to be infinitely extended. In figure 5.11, it is shown how a crystal (left) changes its shape when undergoing a rigid body rotation (middle). This prevents the rotation of the tricrystal.

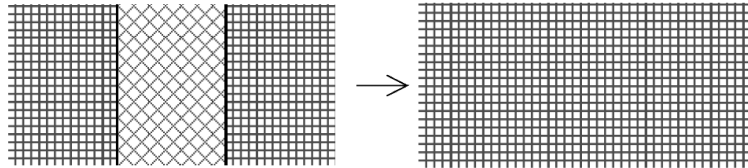


Figure 5.10: Schematic view of a tricrystal with planar interfaces. With final rotational mobility in the solid phase, the crystal will rotate until the grain boundary is disappeared.

In the phase-field model as presented here, such a rotation is possible. The grain boundary energy depends on the misorientation as shown in figure 5.9. If the sandwiched crystal changes its orientation at the interface by a small amount, the grain boundary energy will be reduced. To avoid the deformation energy, the rest of the crystal will follow and a rotation as shown in figure 5.11 (right) will occur. This kind of rotation is prohibited in a proper crystal by the connectivity in the crystal.

Another possible way of expressing the rotation of the sandwiched crystal

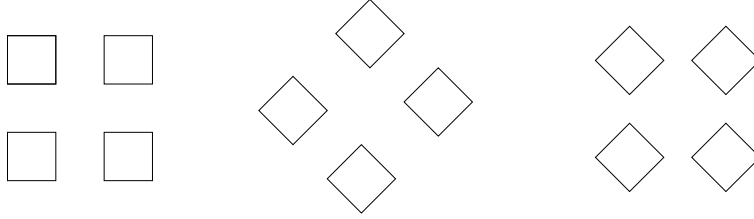


Figure 5.11: The schematic crystal (left) can only rotate by a rigid body motion (middle). In the case of the tricrystal, this is prevented by the shape of the crystal. In the model, the rotation proceeds by local rotations of the unit cells in the crystal (right). In real systems, this behavior is prevented by the connectivity of the crystal.

is by describing the grain boundaries in terms of dislocations, as introduced in chapters 2 and 4. The two grain boundaries are made up of dislocations of different sign which could annihilate when brought together. This would decrease the dislocation density in both grain boundaries and therefore decrease the misorientation angle, hence decrease the grain boundary energy. However, the arrangement of the dislocations in the grain boundary corresponds to a local minimum in the dislocation energy. To annihilate two dislocations in the bulk, a dislocation from each of the grain boundaries would have to be moved out of the grain boundary and into the bulk, which would be associated with a large energy penalty. For a large enough distance between the grain boundaries, this energy barrier cannot be overcome and therefore this kind of rotation does not occur.

To account for this energy barrier and hence to avoid the artificial grain rotation in this model, the rotational mobility τ_θ is chosen to be zero in the solid. In the liquid, τ_θ is assumed to be very high. The molecules or atoms are expected to be orientated in some arbitrary way far in the liquid, but align easily according to the crystalline structure in the proximity of the solid. This avoids that defects are frozen in as the interface advances. In this work, τ_θ is chosen to depend on the phase field ϕ as $\tau_\theta = \tilde{g}(\phi)$, which yields the desired behavior.

5.2.3 Anisotropic solid-liquid interface in 1d

In this subsection, different systems are investigated in which a solid is surrounded by its liquid at melting temperature. Independently of the crystalline orientation in the solid, one expects a stationary interface since both phases have equal free energies and therefore a motion of the interface should not lead to a decrease in the energy.

Nevertheless, a different behavior is observed in the simulations. Depending on the crystalline orientation in the bulk, the interface starts to grow with a very small speed.

This artificial interface motion is due to the formulation of the equation of motion for the angle variable. When introducing anisotropy, the free energy depends explicitly on the orientation variable. When minimizing the free energy, this leads to a torque term in the equation of motion for the orientation field

$$\theta: W(\vec{n}, \theta)(\nabla\phi)^2[\partial_\theta W(\vec{n}, \theta)].$$

In the case of an interface parallel to the y -axis, and for an orientation of $\theta = \pi/4$, the torque term $\partial_\theta W \propto \sin(4\theta) = 0$ and no artificial interface motion is expected. This is shown in figure 5.12.

In figure 5.13, the orientation in the solid is $\theta = \pi/6$, therefore $\partial_\theta W \propto \sin(4\theta) \neq 0$, causing the angle to vary in the interface. This creates a force that drives the interface and causes the crystal to grow artificially.

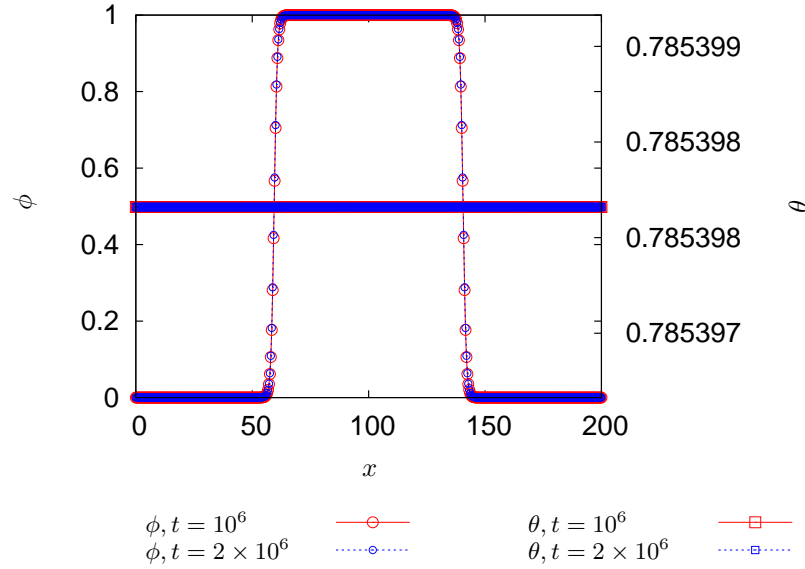


Figure 5.12: Two one-dimensional liquid-solid-liquid system at melting temperature, where the solid has a crystalline orientation $\theta = \pi/4$ and the anisotropy is given by $\epsilon_4 = 0.05$. The phase field ϕ (circles) and the orientation θ (squares) are shown at different times t . Here, $\partial_\theta W = 0$, the angle is constant in the entire system and the interface does not move.

This behavior can be explained as follows. Due to this torque term, the system can minimize its energy by changing the orientation at the interface. In the interface, since ϕ is smaller than one, the energy costs of an angle gradient become finite and the energy is minimized due to this interplay between surface energy and bulk deformation, similar to what is shown for the liquid crystals in chapter 3. By freezing-in this very small angle gradient, the system can minimize its energy and starts to grow, thus approaching an interface orientation which is more favorable.

In figure 5.14, an enlargement of the newly grown area of figure 5.13 is shown. As the crystal grows, it changes its orientation slowly in the solid to decrease its interface energy. Therefore, it is possible to decrease the systems energy by crystal growth, even if the temperature does not favor the solid state. Note that the change in orientation inside the solid is of the order 10^{-14} .

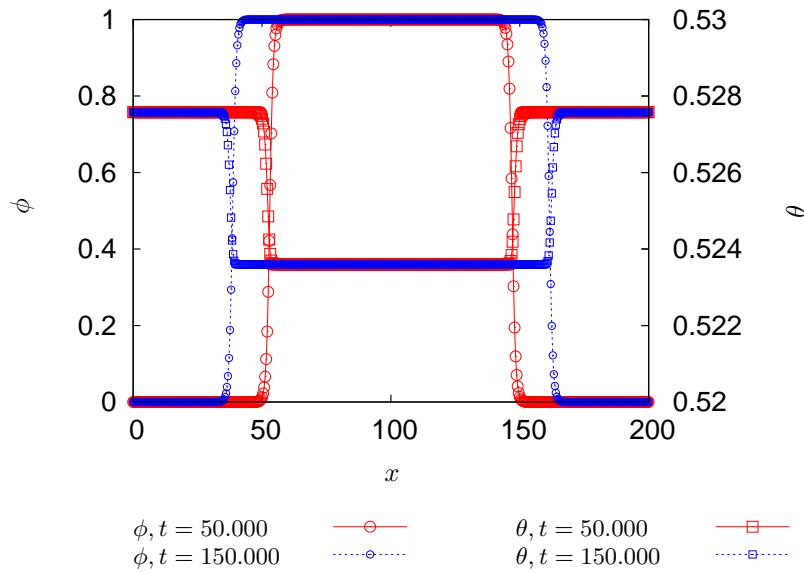


Figure 5.13: Two one-dimensional liquid-solid-liquid system at melting temperature with a solid orientation $\theta = \pi/6$ and an anisotropy of $\epsilon_4 = 0.05$. The phase field ϕ (circles) and the orientation θ (squares) are shown at different times t . Contrary to the system shown in figure 5.12, $\partial_\theta W \neq 0$, the angle varies in the interface and the interface moves with time.

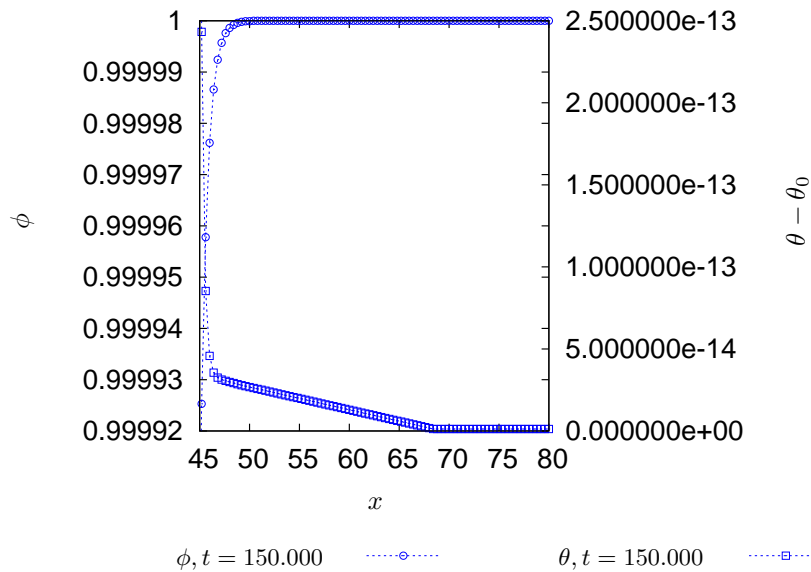


Figure 5.14: Enlargement of the right interface region from figure 5.13. As the solid artificially grows, it changes its orientation and decreases its free energy. To point out the magnitude of the variation, the difference of the angle to the initial angle θ_0 is plotted.

5.2.4 Anisotropic solid-solid interface in 1d

In this subsection, systems are investigated where two solids with different orientation grow towards each other and impinge. A grain boundary is formed which then starts to move with a velocity depending on the orientation of the two solids. In figures 5.15 and 5.16, the results of two systems with different misorientations are shown for three different times. In both systems, the orientation at the left hand side is fixed at $\theta_1 = \pi/4$, while the one at the right hand side varies. In figure 5.15, $\theta_2 = \pi/10$ leading to a misorientation of $\Delta\theta = \pi/5$. In figure 5.16, $\theta_2 = \pi/20$ and the misorientation is given by $\Delta\theta = 3\pi/20$. In figure 5.17, the interface positions are summarized for these two grain boundaries as a function of time. The interface velocity is given by the slope of the curves. One can see that the system with the larger misorientation (red) is moving faster than the system with the smaller misorientation (blue).

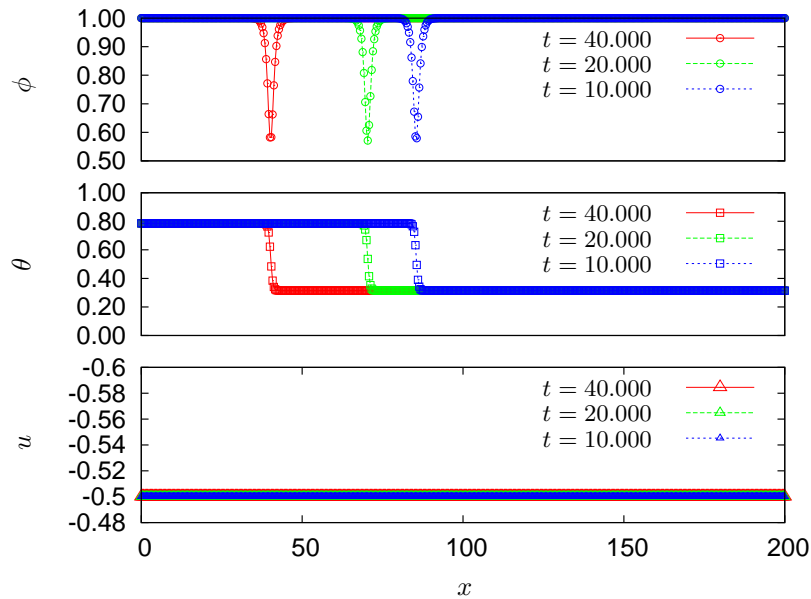


Figure 5.15: Grain boundary with a misorientation of $\Delta\theta = \pi/5$, where the angle at the left hand side is fixed to $\theta_1 = \pi/4$ and on the right hand side to $\theta_2 = \pi/10$. The anisotropy in the system is given by $\epsilon_4 = 0.05$. The interface starts to move artificially, as summarized in figure 5.17.

The effect of the artificial grain boundary motion is similar to the one for the solid-liquid interface motion and comes from the torque term at the interface. While in the solid-liquid interface the orientation can adjust freely in the liquid phase, for solid-solid grain boundaries, the orientation is fixed in both bulk phases. Still, the orientation varies in the interface and the misorientation can be reduced if one of the solids changes its orientation to approach the other orientation. The solid with the less preferred orientation grows by freezing in a small angle gradient, decreasing the misorientation and approaching a more favorable interface orientation.

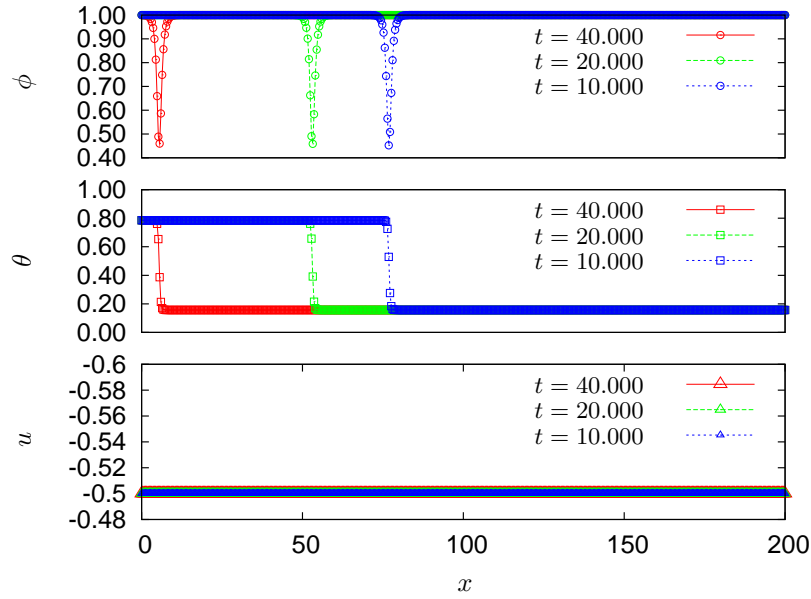


Figure 5.16: Grain boundary with a misorientation of $\Delta\theta = 3\pi/20$, where the angle at the left hand side is fixed to $\theta_1 = \pi/4$ and on the right hand side to $\theta_2 = \pi/20$. The anisotropy in the system is given by $\epsilon_4 = 0.05$. The interface starts to move artificially, as summarized in figure 5.17.

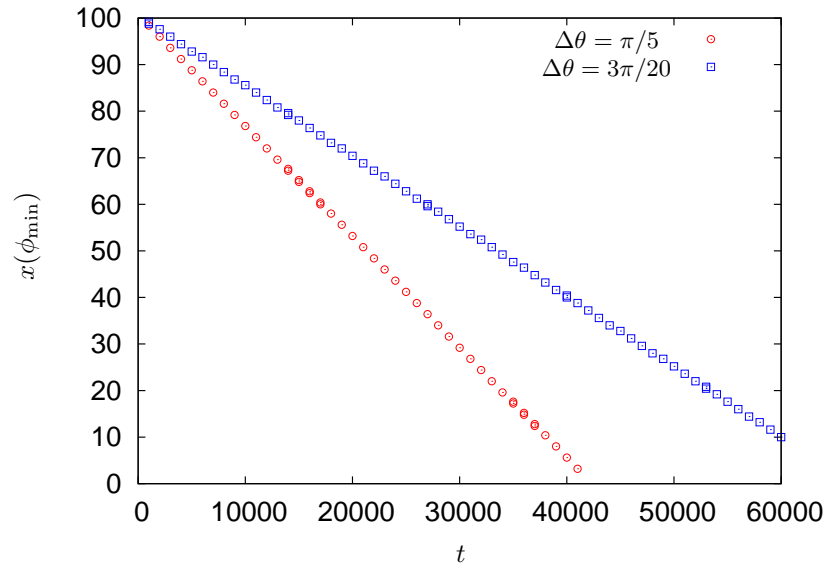


Figure 5.17: Interface position $x(\phi_{\min})$ versus time for the systems shown in figures 5.15 and 5.16. The interface velocity is given by the slope of the curves. One can see that the system with the larger misorientation moves faster.

5.2.5 Importance of the artificial growth

As has been shown in the previous subsections, the model is able to treat localized solid-solid grain boundaries. However, when one introduces anisotropy in the surface energy, there is a very small force which drives the interfaces, even if the two adjacent phases have the same thermodynamic energy. The growth rate is very low, such that its effect is much smaller than the growth usually introduced by the imposed undercooling.

In this subsection, this artificial driving force is compared with the undercooling, as is explained in the following. It is possible to adjust the temperature numerically such that the volume does not change while the system approaches its equilibrium state. For a planar interface, there are no surface corrections and the equilibrium temperature is known to be $u_{\text{Eq}} = 0$. Since the anisotropy in the model leads to an artificial force onto the interface, this force has to be canceled out by a change in the equilibrium temperature. Therefore, the change in the equilibrium temperature is a measure of the importance of the artificial effect.

To fix the volume numerically, one can proceed as described in the following. In the liquid, $\phi = 0$ while in the solid $\phi = 1$. Hence, the integral over the phase field $\phi(x, y)$ over the entire volumes gives a measure of the volume of the solid

$$\text{Vol} = \int \phi(x, y) dV. \quad (5.24)$$

The requirement that the volume remains constant is equivalent to saying that the time-derivative of the volume is zero,

$$0 = \partial_t \text{Vol} = (\partial_\phi \text{Vol})(\partial_t \phi) = \sum_{ij} (\partial_t \phi_{ij}), \quad (5.25)$$

where the integral over the continuous function $\phi(x, y)$ has been replaced by a sum over all discrete lattice points i, j of the discrete function ϕ_{ij} . The expression for $\partial_t \phi$ is given in Eq. (5.20) and depends on the normalized temperature u . It can be brought to the form $\partial_t \phi_{ij} = A_{ij} + B_{ij}u$, where A and B are known functions of the phase field and of the orientation field. Solving $\sum_{ij} (\partial_t \phi_{ij}) = 0$ for u gives

$$u = \frac{-\sum_{ij} A_{ij}}{\sum_{ij} B_{ij}}, \quad (5.26)$$

so that u can be adjusted in each time step according to the fields ϕ and θ until the equilibrium shape and temperature is found.

Doing so, one can suppress the artificial growth of a solid slab in its liquid. By construction, the volume remains constant but the equilibrium temperature u_{Eq} now depends on the orientation, which is not physical and caused again by the torque term.

A system with an orientation in the solid of $\theta = \frac{\pi}{6}$ is shown in figure 5.18. The temperature obtained by forcing constant volume is given by $u_{\text{Eq}} = 3.34 \times 10^{-5}$ instead of $u_{\text{Eq}} = 0$, as would be expected for a planar interface. The undercooling used for the simulations of solidification processes later on in this work is of the order of 0.1. The artificial force is hence very small as compared to the driving force which leads to solidification.

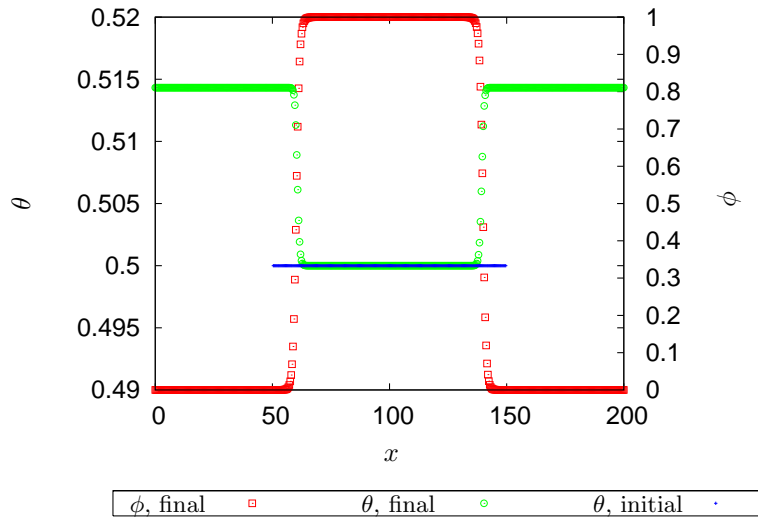


Figure 5.18: A one-dimensional system of a solid slab is surrounded by its liquid. For a stationary system with constant volume, $u = 3.34 \times 10^{-5}$ and an anisotropy of $\epsilon_4 = 0.05$. In squares ϕ and in circles θ are shown.

A two-dimensional solid disc surrounded by its liquid adjusts its equilibrium shape according to the surface tension. As explained in section 2.1.2, this so-called Wulff shape can be obtained from the Wulff construction.

In figure 5.19 (left), the numerically obtained equilibrium shape is shown in green points, together with the Wulff construction (red lines). The inner envelope of the red lines gives the Wulff shape, which agrees very well with the numerical result.

To show that the model is capable of treating crystals with arbitrary crystalline orientations, the equilibrium shape of a solid with an orientation angle of $\theta = \frac{\pi}{6}$ is shown in figure 5.19 (right) with red circles. Since the anisotropy in the surface tension depends on the interface direction with respect to the local crystalline orientation, the resulting equilibrium shape is expected to be identical to the one for a system with $\theta = 0$, but rotated by an angle of $\pi/6$. This is shown in the same figure with blue crosses. The agreement is very good, showing that the model reflects the correct anisotropy for arbitrary crystalline orientations.

To investigate finite size effects, in figure 5.20 (left), a solid with crystalline orientation $\theta = \frac{\pi}{6}$ is shown together with an identical system, but where system size and grain radius are chosen twice as large. Again, the equilibrium shapes agree very well, whereas the equilibrium temperature in the larger system is half the one in the smaller system, as expected from the Gibbs-Thomson condition.

Finally, a modification of the phase-field model as introduced so far is tested. As shown in sections 5.2.4 and 5.2.3, there is a torque term in the equations of motion for the angle field which causes the artificial interface motion. In principle, it is interesting to omit this term and hence cure the problem with the artificial interface motion. In this approach, the equations of motion are not

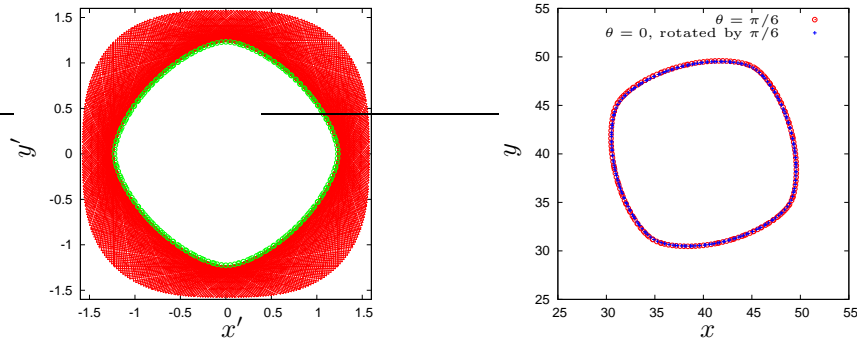


Figure 5.19: Left: The equilibrium shape obtained numerically (green circles, rescaled and shifted) agrees well with the Wulff shape (white area inside the red lines). Right: The equilibrium shape of a solid with local crystalline orientation of $\theta = \frac{\pi}{6}$ is shown with red circles. It corresponds very well to the equilibrium shape of a crystal with orientation $\theta = 0$, which has been rotated by an angle of $\pi/6$, as shown with blue crosses. This proves that the model can simulate grains with different local crystalline orientations and still represent the correct surface energy, which depends on the interface orientation with respect to this crystalline orientation. In all systems, the anisotropy is given by $\epsilon_4 = 0.05$.

obtained from a free energy functional anymore but have to be seen as purely phenomenological. Then, however, the time evolution does not lead to an exact minimization of the free energy of the system. To investigate the effects of such an approach to the equilibrium shape, in figure 5.20 (right) the full model is compared with the model where the torque term is omitted. The difference in the equilibrium shapes is hardly visible, but the equilibrium temperatures differ by a value of the order 10^{-6} , showing once more that the artificial effect is very small.

To summarize, the effect caused by the anisotropy which leads to artificial grain growth or, at constant volume, to a change in the equilibrium temperature is very small. The grain growth is much slower than the usual grain growth caused by an undercooling in the liquid. The effect corresponds to an artificial undercooling of the order of 10^{-5} , while the undercoolings used in this work are usually of the order of 0.1 or larger. Also, the equilibrium shape remains qualitatively the same and corresponds very well to the theoretical Wulff shape. It is therefore possible to use the model to simulate the growth of polycrystalline materials, as long as one keeps in mind that there are small effects which can influence the results very close to equilibrium.

5.2.6 Formation of polycrystals

Having investigated some simple systems and shown that the model is capable of creating proper grain boundaries, it is possible to turn to the initial purpose of simulating the solidification of grains with different crystalline orientations.

Firstly, two grains with different orientations, $\theta = \pm\pi/10$, are placed next

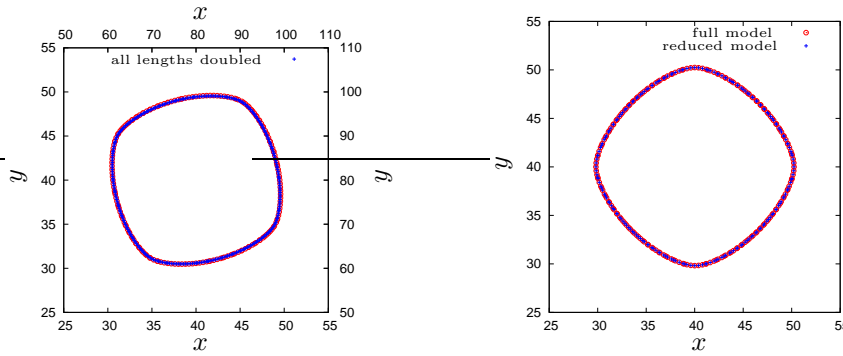


Figure 5.20: Left: Two-dimensional solid ($\theta = \frac{\pi}{6}$) surrounded by its liquid. The equilibrium shape is shown with red circles and as a comparison with blue crosses the equilibrium shape of the same system with all geometrical lengths doubled. Right: Two-dimensional solid ($\theta = 0$) surrounded by its liquid. The equilibrium shape is shown with red circles for the full model and as a comparison with blue crosses for the model artificially suppressing the torque term, as explained in the text. In all systems, the anisotropy is given by $\epsilon_4 = 0.05$.

to each other and are allowed to grow into the same undercooled liquid. In figure 5.21, the interfaces are shown for different times. One can see that the dendritic form is rotated according to the crystal orientation, caused by the anisotropy in the interface energy. As the two grains grow bigger, they start to approach each other and finally they interact. They form a grain boundary between them while they keep growing in the other directions. In the simulation, reflecting boundary conditions are applied, which explains the behavior of the light-blue interface-contour at the boundary.

As next example, a situation is studied where four grains start to grow from the corners with different local crystalline orientation. To speed up the simulations, reflecting boundary conditions are used. To ensure complete solidification, in the entire system, the temperature u is lowered globally by $q(\Delta + u)$, where Δ is the undercooling and q is a small parameter. Initially, the system is undercooled at $u = -\Delta$. As the solid grows, the produced latent heat has to be transported into the liquid and the solid, heating up the system. Finally, most of the heat is extracted homogeneously in the entire system. This explains why the shapes are rather round and only slightly deformed. Still, the small difference in the shapes as the system is entirely solidified leads to grain boundary motion, in the end only two grains remain, building a planar and hence stable interface. The orientations are : 0° (yellow), 14.3° (blue), 28.6° (red) and 43.0° (green), the solid-liquid and the solid-solid interface is shown in black. A time series of the solidification is shown in figure 5.22. The model parameters are $\Delta x = 0.4$, $\Delta t = 0.01$, $w_0 = \tau_0 = \lambda = D = 1$, $\nu = 0.7$ and $\epsilon_4 = 0.05$.

Finally, in figure 5.23, four solids with local crystalline orientation 0° (yellow), 8.6° (blue), 25.8° (green) and 34.3° (red) start growing side by side into the undercooled liquid. One can see that the growth speed depends on the anisotropy and therefore on the local crystalline orientation. Again, two of the grains are

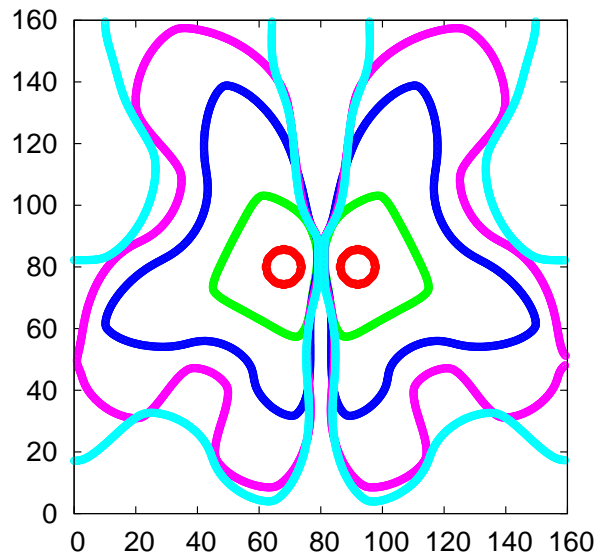


Figure 5.21: Two-dimensional system of two solids of different orientation ($\theta = \pm\pi/10$) growing towards each other. In the system, the anisotropy is given by $\epsilon_4 = 0.05$. The interface is shown at different times.

outgrown and start to disappear.

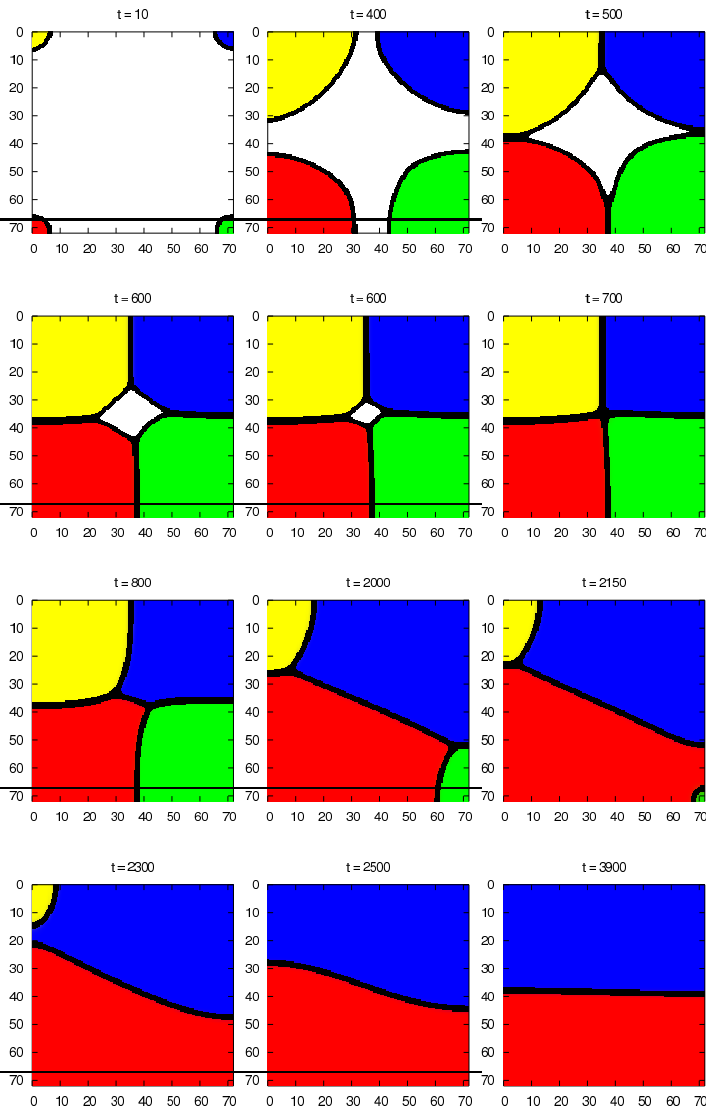


Figure 5.22: Four solids with different crystalline orientation, namely 0° (yellow), 14.3° (blue), 28.6° (red) and 43.0° (green) are growing towards each other from the corners. The interface is shown black. To ensure that the system solidifies entirely, heat is extracted from the initially undercooled system equally everywhere. As the system is totally solidified, the grain boundaries continue to move according to the curvature. The anisotropy in the system is given by $\epsilon_4 = 0.05$.

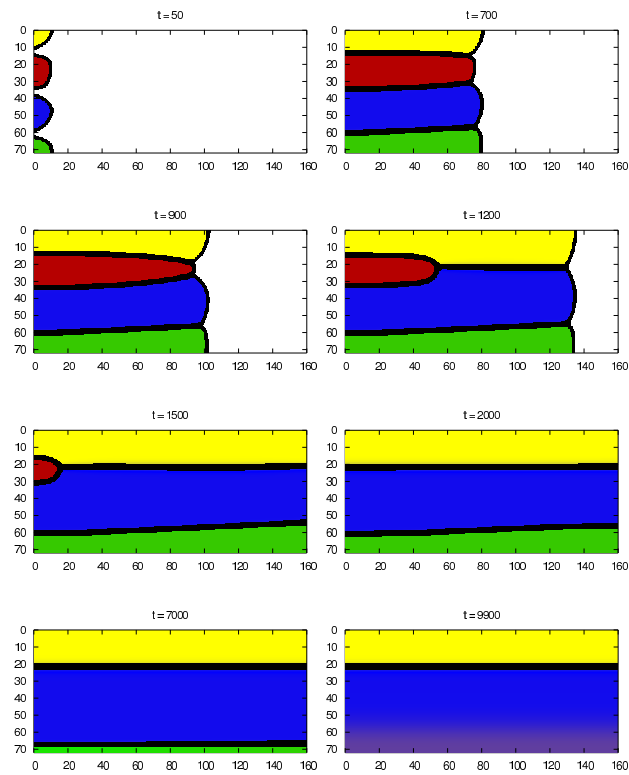


Figure 5.23: Four solids with different local crystalline orientation, namely 0° (yellow), 8.6° (blue), 25.8° (green) and 34.4° (red) are growing side by side. The interface is shown in black. One can nicely see how the growth velocity depends on the orientation and how two grains disappear during the simulation. The anisotropy in the system is given by $\epsilon_4 = 0.05$.

5.3 Conclusion and outlook

In this chapter, a new model for the simulation of polycrystals has been developed. It contains a phase-field variable, representing the local order, which is equal to one in the solid and equal to zero in the liquid, as often used in the standard phase-field models. In this model, it is additionally used to represent the reduced order in grain boundaries. As one goes from one grain to another, the phase-field variable is decreased to a certain non-zero value, having its minimal value exactly at the grain boundary. As one enters the other grain, it increases again.

The local crystalline orientation is given by a second field. Its value represent the crystalline orientation with respect to the coordinate system and is constant inside the grains. It varies drastically in a localized region between the grains, in the grain boundary, where the order indicated by the phase field is reduced.

An important part of the model is the free energy, from which the equations of motion are obtained. The free energy has been discussed in great detail and the form of the coupling function between phase field and orientation field was motivated by physical considerations.

The model has been tested, based on the question whether it is capable to reproduce localized grain boundaries and was found to work well for isotropic grain boundaries. It was discovered, however, that for a certain set of model parameters, there is a critical misorientation of two neighboring grains. Grain boundaries with a lower misorientation disappear. The critical angle can be varied by changing the model parameters, so that theoretically arbitrarily small angle differences can be resolved.

The grain boundary energy has been calculated for different misorientations and compared with the theoretical description from Read-Shockley as derived in section 2.1. Good qualitative agreement was found, without attempting to relate the model parameters to the parameters of the Read-Shockley grain boundary energy.

Introducing anisotropy, a spurious interface motion was observed, for solid-liquid interfaces as well as for solid-solid interfaces. The importance of this effect has been tested and it was found to be important only for simulations close to equilibrium. Applying a typical undercooling, the artificial interface motion is small against the motion caused by the undercooling or the motion by curvature.

It is therefore possible to use the model to simulate polycrystalline materials of one chemical component but with grains of different crystalline orientations. In the future, it would be interesting to simulate larger systems with this model, which is not a problem conceptually, but from the computational point of view not reasonable for this work. The problems observed with this model are discussed in greater detail in the next chapter. It is found that some of them are generic for this type of model and that it is therefore interesting to search for a completely different approach.

Comparing this model with the one by Kobayashi and coworkers, as presented in section 2.3.3, one finds that they are rather similar. They possess similar advantages and disadvantages, and also the problems found in this work are suspected to appear in both models. The form of the free energy introduced in this work is mathematically more convenient and allows for simple integration schemes, even though the numerical implementation contains some difficulties due to the singularities, too. Due to the similarity to the standard phase-field

models, analytical calculations are easier to perform in this model. By investigating the grain boundaries at equilibrium and the Wulff shape, this model has been tested for its physical behavior, benchmarks which have, to the knowledge of the author, not been performed in the model by Kobayashi and coworkers. Nevertheless, there is not reason to believe that similar results cannot be obtained with their model, too. The model developed in this work has therefore to be seen as an alternative model, with similar strengths and weaknesses.

Chapter 6

Summary, Conclusion and Discussion

This work addresses the question of how to model polycrystalline solidification with a phase-field model. The model is supposed to be based on the microscopical description of the crystal, while remaining capable of simulating length scales of the order of microns. This motivates the development of an alternative model next to the two already existing models. The first one of these models describes each grain with a different phase-field variable, which is found to be not the most elegant and intuitive way. The second kind of existing models for polycrystalline solidification is based on a description in terms of two parameters, one for the order and one for the orientation of the crystal. This way of describing the polycrystal is the one aimed at in this work, but there are still two shortcomings in the models. Firstly, the description of the orientation does not respect the symmetry of the crystal by itself. When calculating angle differences, special numerical tricks have to be applied to take into account all the configurations which are identical due to the crystalline symmetries. The second deficit is of more formal nature. To obtain localized grain boundaries, it is necessary to include the modulus of the orientation gradient in addition or instead of the usual squared gradient term in the free energy.

In this work, these two fundamental problems have been addressed and possible ways to circumvent them were proposed.

6.1 Tensor description for orientation field

Concerning an alternative way of describing the orientation in the crystal, an idea from the physics of liquid crystals has been taken up. Liquid crystals are rotationally invariant under rotations of 180° and can be described by tensors of rank two. This tensorial description corresponds to the underlying symmetry. In this work, this has been used for addressing a so far unsolved question on the stability in nematic-isotropic liquid crystals.

In chapter 3, a phase-field model for the directional solidification of a nematic liquid crystal alloy has been developed, using a tensorial order parameter. For analytical considerations, a transformation back to more intuitive variables has been presented. In these variables and for isotropic systems without orientation variations in the nematic phase, the equations of motion reduce to the well known scalar phase-field equations for the solidification of pure materials. This permits the use of the already derived relations between model parameters and physical quantities.

With anisotropic coupling between the nematic orientation and the interface, however, deformations in the nematic phase appear when the planar interface becomes unstable, affecting the stability of the interface.

The stability of the planar interface has been investigated numerically and was compared with a generalized linear stability analysis, which takes into account the nematic orientation at the interface. Instead of assuming the perfect alignment of the director normal to the interface, a new anchoring condition has been derived, considering the interplay between the deformation energy in the bulk and the surface energy due to unfavorable alignment. The model has been validated by comparing the theoretical analysis with the simulation results, which has shown a very good agreement for several different anisotropy strengths. Having validated the model, the influence of the nematic orientation in the bulk on the formation of cells has been investigated. It has been shown

that varying the nematic orientation in the bulk can break the symmetry of the system, destabilize the cells and lead to cells which are changing their shapes with time.

A problem still to address is how the interface width can be scaled without changing the underlying physics. In this formulation, with the elastic length an additional length scale exists next to the capillary length. Both lengths scale differently with the interface width, which prevents the upscaling of the interface width so far. More thoughts on this subject are necessary, a possible way of avoiding this problem might be to introduce an extra field to obtain an additional degree of freedom in the free energy which might allow to uncouple the two length scales.

From the numerical point of view, the study in this work has shown that a tensor can be used very elegantly and efficiently as order parameter to describe an orientation field. Once the equations of motion are established, the numerical implementation is straightforward. The gradients can be calculated in the simplest way and all the symmetry considerations are automatically included. The equations of motion, however, become rather complicated and unintuitive. A tensor of rank two has nine components, but in two dimensions there are only two degrees of freedom in the system, the absolute value and the orientation. Therefore, there are constraints on the tensor components which have to be considered and introduced into the equations of motion. This has been done by using Lagrange multipliers. The resulting equations of motion then respect all the symmetries of the system even though they are not easy to identify. Rewriting them in a simpler form, coming back to more intuitive variables, is possible and advisable when performing analytical analyses.

In principle, the extension from two to three dimensions using tensor order parameters for the orientation is straightforward. It is conceptually easier than it is in the description based on a scalar angle field in two dimensions. Still, in this work, only two-dimensional systems have been investigated, concentrating on tensors of rank two. Working with tensors of rank four increases the number and the complexity of the constraints on the tensor components, which would render the equations of motion even more complicated.

6.2 Grain boundaries on a smaller length scale

One of the main difference between the liquid crystals and the polycrystals envisaged in this work is the existence of grain boundaries. In liquid crystals, topological defects or disclinations in two dimensions are point-like and grain boundaries do not exist. In between two regions of differently aligned nematics, the orientation varies continuously and linearly, instead of forming grain boundaries. Generally, this problem cannot be solved by simply adapting the rank of the tensor to the symmetry of the crystal.

Grain boundaries are, in the limit of low misorientations, made up of dislocations. Also, long range elastic effects are important for crystals, since they account for the connectivity between the different atoms. Both effects are not included in the regular phase-field models of solidification, but recently a model has been developed which includes these effects on smaller length scales automatically. This so-called phase field crystal model is numerically similar to the phase-field model and has been investigated in chapter 4 to obtain further

insights into grain boundaries and their description.

The first topic which has been studied with the phase field crystal model is the variation of the order parameter inside solid-liquid interfaces and grain boundaries. Examining solid-liquid interfaces in greater detail, it was found that the average density over a unit volume is a suitable measure of the state of the system. The average density is high in the solid phase and decays over the distance of a few atomic layers into the liquid, again in agreement with the concept of diffuse interfaces. Similarly, solid-solid interfaces can be explored, showing that the local crystalline order is reduced in the interface region, a fact that has been used in the phase-field models with orientation fields.

In a second step, the grain boundaries have been examined further and it was found that they possess realistic properties. The grain boundary energy has been obtained numerically and compared with the Read-Shockley theory for low-angle grain boundaries, where very good agreement was found.

This makes it interesting to use the phase field crystal model to investigate grain boundary wetting in dependence on the misorientation. A phenomenological model for the stability of a liquid film between two solids has been presented. It describes the contact potential between two solid grains and predicts monotonous attractive or repulsive behavior of the grain boundaries, in dependency on the grain boundary energies. While for high-angle grain boundaries the simulations agree well with the model, a different behavior was found for low-angle grain boundaries. Here, the interaction is not monotonous, the grains are attractive at larger distances and repulsive for smaller ones.

The main difference between these two regimes seems to be the distance between the dislocations. For high-angle grain boundaries, the dislocations overlap and the liquid between two solids can be seen as a rather homogeneous film. For low-angle grain boundaries, the dislocations are well separated. As long as there still is a considerable amount of liquid in the grain boundary, the dislocations in the low-angle grain boundaries seem to pair up and share a liquid pool between them rather than forming a homogeneous film. This behavior contradicts the phenomenological model and might explain its failure. As the amount of liquid decreases further, the distance between the dislocations becomes relatively equal again, corresponding to the Read-Shockley description of grain boundaries.

To gain further insight in the interaction between the grain boundaries, the contact potential as it appears in the phase field crystal model has been obtained numerically. While for the high-angle grain boundaries the agreement with the phenomenological model is satisfactory, for low-angle grain boundaries the non-monotonous behavior is reflected in the contact potential.

A practical interest in the wetting properties of grain boundaries is its relation with the so-called hot tearing. During the solidification process of metal alloys, a possible source of cracks is the mushy zone. Here, the amount of liquid is already very limited, grains of different orientation grow very close to each other, separated only by liquid films. These films induce a decrease in the stress resistance of the material. The stability of these films, as investigated in a simple setup in this work, is therefore crucial for the better understanding of this phenomenon.

6.3 New phase-field model for polycrystals

Coming back to the initial interest of finding a convenient model for polycrystalline solidification on a larger length scales, a new phase-field model has been developed in chapter 5. It avoids the modulus term in the free energy by introducing a singular coupling function instead, which couples the angle gradient with the phase field. In the liquid, the coupling function goes to zero, corresponding to the fact that here an angle-gradient does not lead to an increase in the free energy. The energy costs of a deformation in the solid, however, is orders of magnitude larger than the ones in the liquid. In the model, this is represented by a coupling function which tends to infinity in the solid phase.

The specific form of the singular coupling function is very important to the model. After careful considerations, a suitable coupling function has been derived and the resulting grain boundary properties have been investigated. It was found that the grain boundaries are localized and stable, with a lower critical misorientation depending on the model parameters. The existence of the minimal misorientation has already been predicted in the derivation of the coupling function.

The grain boundary energy has been obtained from numerical simulations of the model and has been compared to the Read-Shockley theory. Qualitative agreement was found for small misorientations, while no attempt has yet been made to relate the model parameters to the elastic constants. The agreement with the Read-Shockley like grain boundary energy appears naturally in the model, but the reason for this is not yet well understood.

Unfortunately, there are also some problems with the model. The first deficit is related to the rotational degrees of freedom of the orientation. The phase-field equation for the angle field is written similarly to the one for liquid crystals in terms of an nonconserved order parameter. This allows in principle a local rotation of each point in the crystal, which is certainly possible for liquid crystals but not for polycrystals. On the example of a tricrystal, it has been shown how a grain rotation can occur in the proposed model. This problem can be cured by choosing the mobility constant in the angle-field equation in a smart way. In this work, the rotation in the solid has been prevented by using a rotational mobility which vanishes in the solid. To ensure that the liquid can adjust its orientation in the proximity of the solid, the rotational mobility is chosen to be very large in the liquid phase.

A second problem occurs when introducing anisotropy to the model. The anisotropy term in the free energy depends explicitly on the orientation field, which leads to an extra term in the equation of motion of the angle field. This extra term has been identified as a torque term, which tries to align the crystal at the interface according to the anisotropy. The effect is similar to the interplay between bulk deformation and interface energy in the liquid crystal case treated in chapter 3. For the polycrystal model, the energy costs of a deformation in the solid diverges, therefore the orientation in the bulk does not change. In the interface, however, a change in angle has been observed, which then leads to a driving force onto the interface. This effect happens in both, solid-liquid and solid-solid interfaces for most orientations. Its importance has been investigated and was found to be orders of magnitude smaller than the usual driving forces due to undercooling.

To investigate the effect of the anisotropy, the equilibrium shape has been

obtained for crystals with different crystalline orientations. It has been compared with the theoretical Wulff shape and very good agreement was found. It has been shown that by varying the crystalline orientation the preferred growth directions adapt as expected, which allows the simulation of differently orientated solids in the same system.

With these successful verifications, the model has been used to simulate the evolution of polycrystals with grains of different orientations.

6.4 Outlook

To proceed in developing a better model for the polycrystal solidification, three different approaches have been pursued in this work. Each of them is worth being investigated further.

The first one addresses in the representation of the angle field. From the conceptual point of view, it is very interesting to extend the tensor-description to simple cubic symmetries, which implies to formulate the equations of motion in terms of rank four tensors. This is expected to be quite complicated and might lead to lengthy equations of motion. Nevertheless, as has been shown for liquid crystals, the numerical problems when treating angle differences simplify significantly in the tensorial description. The formulation in terms of rank four tensors can then be generalized to three dimensions.

The other approach towards phase-field models for polycrystals described in this work is based on the phase field crystal model. Since the phase field crystal model has turned out to be very capable of describing grain boundaries and also cracks, further research on this model is suggested. The main disadvantage of the phase field crystal model is its limitation to rather small system sizes. The periodic structure has to be resolved numerically, which is of the order of the interatomic distance ($\mathcal{O}(10^{-10}\text{m})$). Simulating physical systems with a characteristic length scale of one micron is therefore very difficult and time consuming in two dimensions and nearly impossible in 3D, even with advanced parallelization techniques. There are some approaches [88,89] to rewrite the phase field crystal equations in terms of variables with slower spatial variations. This can lead to an enormous speed up when using adaptive mesh techniques. The computational effectiveness depends, however, largely on the systems investigated: only inside of defect-free crystals or in the liquid phase can the mesh be redefined, whereas in grain boundaries the fine grid spacing has to be used. Therefore, for the systems investigated in this work, these approaches were not useful, especially since they include approximations which are not yet well tested for systems where stresses play a role.

Another possible approach to larger length scales is to coarse-grain the phase field crystal model. This could result in a phase-field-like model, including terms which lead to grain boundaries more naturally than the approaches investigated in this work. Nevertheless, this procedure appears rather cumbersome.

In general, the phase field crystal model could be extended to be able to treat interactions with particles, investigating how the grain growth can be influenced by them. Addressing elasticity, the phase field crystal model has automatically included static elastic effects as has been shown, but since lattice vibrations have been averaged out. To obtain wave propagations in the model phonons have to be introduced back into the model [75]. Further research in this direction could

be interesting, as well as treating different lattices and extending the model consequently to three dimensions.

To address the problem of simulating polycrystals with phase-field methods from a different point of view, it is proposed to develop a new approach in the grain boundary description. In this work, some of the problems appearing in the existing models have been shown. Especially the nature of the equation of motion for the orientation field was found to be conceptionally wrong, even if it is successfully applied to different problems.

It is suggested to concentrate further research onto the incorporation of dislocations into phase-field models to describe grain boundaries. The dynamics of dislocations is of interest for simulations of polycrystals since the grain boundaries can be described very conveniently by an array of dislocations [90, 91]. While the equation of motion used in this work to describe the angle variable as a nonconserved quantity does not respect the physics of the grain boundaries, a description rooted on dislocations could do so. The evolution of the local dislocation density over time can be related directly to a change in orientation. For a grain boundary with a given misorientation, the corresponding dislocations can be constructed and the grain boundary energy can be calculated.

As it turns out, however, the dynamics of grain boundaries is very difficult to describe by the dynamics of the dislocations. Models which treat single discrete dislocations are generally formulated on atomic length scales, such as the phase field crystal model [72–74], even if successful attempts have been made to combine phase-field models with dislocations [92–98]. For the length scales envisaged in this model, one has to consider rather dislocation densities than single dislocations. While continuum models for dislocation densities have been developed [99–101], only few attempts have been made to describe dislocation dynamics which leads to grain boundary formation [102]. To extend this theory to describe grain boundary motion in the sense of polycrystals has so far not been successful.

Another possible approach is to develop a phase-field model which combines solidification with elasticity. Even if there are already phase-field models which include elasticity [103–105] and fractures [79, 106, 107], it seems to be very difficult to develop a fully consistent model for the evolution of the local crystalline structure on larger than atomic length scales.

The quest to develop a simple, elegant, efficient and consistent model for polycrystalline solidification is still open and seems to contain a lot of interesting research areas.

Résumé en français (summary in french)

Lors de la croissance d'une phase solide cristalline, le matériau final n'est en général pas composé d'un seul cristal, mais de grains d'orientations de maille différentes, et éventuellement de domaines de phases thermodynamiques distinctes. Cette structure, dont l'échelle caractéristique est le plus souvent le micron, est décisive pour les propriétés mécaniques et la résistance à la corrosion et à la rupture du matériau final.

Cette structure du matériau se forme en deux étapes. D'abord, pendant la solidification, des formes d'une grande complexité géométrique sont créées, telles que des dendrites, des cellules ou des composites lamellaires ou fibreux. La raison en est une interaction subtile entre des instabilités engendrées par le flux de matière nécessaire pour la croissance et des effets stabilisants dus aux propriétés de l'interface. Ensuite, après la formation du matériau brut, de nombreux processus peuvent modifier cette structure primaire, comme par exemple le mûrissement, le frittage, des transformations de phase secondaires, et des déformations mécaniques.

Alors que de nombreux travaux existent sur la croissance de monocristaux, et sur l'évolution de la structure en grains dans le matériau solide, l'influence de la structure polycristalline sur le processus de morphogénèse lui-même est encore mal connue. Sur le plan théorique, ce manque de connaissances tient en grande partie aux difficultés de la modélisation mathématique et numérique des phénomènes de croissance. En effet, traiter une interface de géométrie complexe en mouvement est une tâche très ardue d'un point de vue numérique. La méthode de champ de phase, développée depuis une vingtaine d'années, permet de s'affranchir de ce problème par l'introduction de champs scalaires auxiliaires qui indiquent l'état local de la matière (les champs de phase), et qui exhibent des interfaces diffuses. La dynamique de l'interface est traduite en équations de mouvement pour ces variables auxiliaires, qui peuvent souvent se déduire du formalisme phénoménologique de la thermodynamique hors d'équilibre. Puisque ces équations sont de simples équations aux dérivées partielles, elles peuvent être traitées par des algorithmes numériques standard.

Deux formulations ont été proposées pour tenir compte de l'orientation cristalline dans le cadre de modèles de champ de phase. La première consiste à considérer chaque grain comme une phase distincte et d'y associer un champ de phase. Ceci constitue une généralisation immédiate des modèles de solidification à plusieurs phases, mais le formalisme résultant est lourd, notamment du fait du grand nombre de champs, et il ne permet pas de représenter un con-

tinuum d'orientations. La deuxième approche, plus récente, travaille en deux dimensions avec deux champs, un champ de phase et un "champ d'angle" qui donne l'orientation locale du cristal. Ce modèle montre de bons résultats, mais il contient des termes peu conventionnels (non analytiques) dans la formulation de sa fonctionnelle d'énergie. Finalement, depuis quelques années, une méthode nouvelle, appelée "cristal de champ de phase" ("phase field crystal" en anglais) s'est développée pour décrire la structure des polycristaux sur l'échelle atomique. En effet, un champ de densité est utilisé qui exhibe une périodicité de symétrie hexagonale en deux dimensions, ce qui fait que ce modèle inclut naturellement des défauts (dislocations) et des effets élastiques.

Le but de cette thèse est d'élucider quelques aspects de la modélisation des polycristaux par la méthode du champ de phase. Trois points sont abordés en détail. Dans la première partie, la possibilité de représenter l'ordre cristallin local par un paramètre d'ordre tensoriel (au lieu de deux champs scalaires) est examinée. Pour simplifier le traitement, cette étude est faite pour des cristaux liquides nématiques, pour lesquels le tenseur nécessaire est de rang 2 (au lieu de rang 4 pour un matériau de symétrie cubique). Dans la deuxième partie, la structure des joints de grains est examinée dans le modèle de cristal de champ de phase. En particulier, la présence d'un film liquide entre deux grains en-dessous de la température de fusion est mise en évidence, et son épaisseur est déterminée en fonction de la température et de la désorientation entre les grains. Dans la troisième partie un nouveau modèle de champ de phase pour la solidification polycristalline est proposé, qui travaille avec un champ d'orientation, mais utilise une fonction de couplage singulière au lieu du terme en module du gradient dans la fonctionnelle d'énergie libre. Ce modèle est analysé en détail, et ses avantages par rapport aux modèles publiés dans la littérature sont discutés. Finalement, les résultats de tous les chapitres sont mis en perspective dans la conclusion, et des possibilités pour de futurs développements sont évoquées.

Modèle de champ de phase pour les cristaux liquides

Dans le chapitre 3, un modèle pour la solidification des cristaux liquides nématiques est développé. Les cristaux liquides présentent une symétrie de rotation de 180° et leur description ne nécessite donc que des tenseurs d'ordre deux. Généralement, les cristaux liquides sont décrits par l'énergie libre de Landau-de Gennes dépendant des gradients introduits par Frank: le "twist", le "bend" et le "splay", qui représentent des modes de déformation.

En partant de cette formulation, un modèle tensoriel est développé pour la "solidification" d'un alliage de cristaux liquides, c'est-à-dire pour la dynamique de la transition isotrope-nématique en présence d'impuretés. Ce système est connu pour être un analogue de la solidification d'alliages métalliques. Cependant, tous les modèles disponibles dans la littérature négligent l'effet de l'ordre nématique sur la dynamique de l'interface isotrope-nématique. Pour un système quasi 2D, la croissance d'un échantillon qui est déplacé à vitesse constante dans un gradient de température est simulée et la stabilité d'une interface plane est analysée pour différentes valeurs des paramètres. En introduisant une anisotropie variable, on peut contrôler l'orientation de la phase nématique à

l'interface.

Pour comparer les résultats de la simulation avec la théorie, une description approchée, mais plus précise que les développements généralement utilisés, pour la stabilité de l'interface est développée. Pour la condition de bord, on tient compte du couplage entre le directeur et l'interface résultant de l'équilibre de la relation entre l'énergie d'ancrage à la surface et l'énergie de la déformation dans le volume, ce qui est plus exact que de supposer que le directeur est toujours perpendiculaire à l'interface. L'analyse de Mullins et Sekerka est généralisée en tenant compte de cette nouvelle condition au bord. Les résultats obtenus par cette méthode sont en très bon accord avec ceux des simulations.

Avec cette étude, il a été montré qu'un champ d'orientation peut être représenté de manière très satisfaisante à l'aide de tenseurs. Du point de vue numérique, les problèmes rencontrés pour traiter explicitement les symétries du système sont évités. Cependant, les équations de mouvement deviennent rapidement très complexes. Pour étudier les équations analytiquement, il est donc possible de les réécrire en fonction de variables plus intuitives, comme par exemple l'orientation et la valeur absolue.

Modèle de “Phase Field Crystal” pour l'étude des joints de grain

Le chapitre 4 approfondit l'étude des joints de grains à l'aide du modèle de “cristal de champ de phase”. Dans ce modèle, l'énergie libre contient des termes de gradients en puissance quatre et les équations de mouvement ont une solution périodique, où les maxima du champ de densité représentent la position des atomes de la structure cristalline. L'état d'équilibre peut être déformé, son orientation peut être modifiée, des défauts peuvent être inclus et des joints de grain peuvent être créés. Mais l'échelle d'espace est de l'ordre de quelques angstroms et est donc plus petite que celle qui peut être atteinte dans les modèles du champ de phase habituels.

Avec ce modèle, des joints de grain sont créés et étudiés sous deux aspects. Premièrement, l'idée du “champ d'ordre cristallin” est quantifiée : on peut définir un paramètre d'ordre qui prend une valeur constante dans les deux cristaux avec des orientations différentes, et dont l'amplitude se réduit dans le joint de grain. Cette idée est utilisée dans le développement du modèle de champ de phase du dernier chapitre.

Deuxièmement, la structure des joints de grain est étudiée. Deux cristaux avec des orientations différentes sont séparés par une couche de liquide. Quand la température baisse, les deux cristaux s'approchent de plus en plus. La stabilité de la couche de liquide est étudiée, et les résultats des simulations sont comparés à un modèle phénoménologique basé sur l'interaction de deux surfaces solide-liquide planes. Il est montré que la validité du modèle dépend de l'angle entre les deux cristaux. Pour les grands angles, le modèle correspond bien aux simulations, tandis que pour les petits angles, le modèle n'est plus valide. La différence entre les deux cas a son origine en la distance entre les dislocations. Le joint de grain peut être décrit par un ensemble de dislocations, et la distance entre deux dislocations dépend de l'angle entre les deux cristaux. Pour les petits angles, les dislocations sont bien séparées, tandis que pour les grands

angles, elles se chevauchent. Le modèle phénoménologique est seulement valide pour les joints de grains où les dislocations sont proches et forment un "film" de liquide d'épaisseur quasi-constante.

Modèle de champ de phase pour les polycristaux

Dans cette partie (chapitre 5), un nouveau modèle de champ de phase est développé. Le problème principal est d'obtenir une énergie libre qui donne des joints de grain bien localisés et stables sans utiliser un terme de gradient non-analytique comme dans les modèles existants. Ce problème est résolu en introduisant une fonction singulière couplant de champ de phase et le champ d'orientation. La forme analytique de cette fonction, cruciale pour les propriétés du modèle, est déterminée par une étude des solutions de joints de grain en une dimension.

Ce modèle est ensuite testé dans diverses situations pour montrer qu'il est bien capable de traiter les polycristaux, avec de bons résultats. Cependant, notre étude met également en évidence que des problèmes liés à l'anisotropie subsistent. En effet, l'inclusion d'un terme d'anisotropie dans l'énergie libre contenant l'orientation locale du cristal et l'orientation de l'interface crée un terme supplémentaire dans l'équation de mouvement pour le champ d'orientation. L'effet de ce terme est étudié et il est montré qu'il engendre une migration artificielle d'une interface plane solide-liquide à la température de fusion. On peut bien comprendre l'origine de cet effet: il résulte de la possibilité pour le système de minimiser son énergie libre, même si cela ne correspond pas à un chemin cinétique compatible avec la cohésion de la matière cristalline. Un système où deux phases solides avec différentes orientations sont en contact exhibe un effet similaire.

Ces effets de mouvements artificiels des interfaces sont étudiés, et il est montré qu'ils demeurent petits. Ils causent donc des problèmes uniquement si la dynamique du système est lente, par exemple si l'on étudie la physique à l'équilibre. C'est pourquoi ils restent négligeables dans les études de la solidification polycristalline si la surfusion est assez grande.

Bibliography

- [1] M. Marder. *Condensed Matter Physics*. John Wiley & Sons, Inc., 2000.
- [2] C. Kittel. *Introduction to Solid State Physics*. John Wiley & Sons, Inc., 7th edition edition, 1996.
- [3] J. D. Bernal. Bakerian lecture 1962, structure of liquids. *Proceedings of the Royal Society of London, Series A-Mathematical and Physical Sciences*, 280(138):299–322, 1964.
- [4] J. M. Howe. *Interfaces in Materials*. John Wiley & Sons, Inc., 1997.
- [5] K. A. Wu, A. Karma, J. J. Hoyt, and M. Asta. Ginzburg-landau theory of crystalline anisotropy for bcc-liquid interfaces. *Physical Review B*, 73(9):094101, 2006.
- [6] W. H. Shih, Z. Q. Wang, X. C. Zeng, and D. Stroud. Ginzburg-landau theory for the solid-liquid interface of bcc elements. *Physical Review A*, 35(6):2611–2618, 1987.
- [7] D. Turnbull and R. E. Cech. Microscopic observation of the solidification of small metal droplets. *Journal of Applied Physics*, 21(8):804–810, 1950.
- [8] D. Turnbull. Formation of crystal nuclei in liquid metals. *Journal of Applied Physics*, 21(10):1022–1028, 1950.
- [9] J. H. Perepezko. Nucleation in undercooled liquids. *Materials Science and Engineering*, 65(1):125–135, 1984.
- [10] H. Jones. The solid-liquid interfacial energy of metals: calculations versus measurements. *Materials Letters*, 53(4-5):364–366, 2002.
- [11] L. Granasy and M. Tegze. Crystal-melt interfacial free energy of elements and alloys. *Materials Science Forum*, 77:243–256, 1991.
- [12] C. Herring. Some theorems on the free energies of crystal surfaces. *Physical Review*, 82(1):87–93, 1951.
- [13] S. Liu, R. E. Napolitano, and R. Trivedi. Measurement of anisotropy of crystal-melt interfacial energy for a binary al-cu alloy. *Acta Materialia*, 49(20):4271–4276, December 2001.
- [14] R. E. Napolitano, S. Liu, and R. Trivedi. Experimental measurement of anisotropy in crystal-melt interfacial energy. *Interface Science*, 10(2-3):217–232, 2002.

- [15] R. E. Napolitano and S. Liu. Three-dimensional crystal-melt wulff-shape and interfacial stiffness in the al-sn binary system. *Physical Review B*, 70(21):214103, 2004.
- [16] G. H. Gilmer. *Handbook of Crystal Growth*, volume 1a, chapter 8, pages 585–637. Elsevier Science, 1993.
- [17] K. I. Moore, D. L. Zhang, and B. Cantor. Solidification of PB particles embedded in AL. *Acta Metallurgica et Materialia*, 38(7):1327–1342, 1990.
- [18] J. J. Hoyt, M. Asta, and A. Karma. Atomistic and continuum modeling of dendritic solidification. *Materials Science & Engineering R-Reports*, 41(6):121–163, 2003.
- [19] D. Hull. *Introduction to Dislocations*. Pergamon Press, 1981.
- [20] W. T. Read. *Les Dislocations Dans Les Cristaux*. Dunod, Paris, 1957.
- [21] W. T. Read and W. Shockley. Dislocation models of crystal grain boundaries. *Physical Review*, 78(3):275–289, 1950.
- [22] W. Kurz and D. J. Fisher. *Fundamentals of Solidification*. Trans Tech, Aedermansdorf, Switzerland, 1992.
- [23] J. S. Langer. Instabilities and pattern formation in crystal growth. *Reviews of Modern Physics*, 52(1):1–28, 1980.
- [24] W. W. Mullins and R. F. Sekerka. Stability of planar interface during solidification of dilute binary alloy. *Journal of Applied Physics*, 35(2):444–451, 1964.
- [25] W. J. Boettinger, J. A. Warren, C. Beckermann, and A. Karma. Phase-field simulation of solidification. *Annual Review of Materials Research*, 32:163–194, 2002.
- [26] J. S. Rowlinson. Translation of j. d. van der waals' "the thermodynamic theory of capillarity under the hypothesis of a continuous variation of density". *Journal of Statistical Physics*, 20(2):197–244, 1979.
- [27] J. W. Cahn and J. E. Hilliard. Free energy of a nonuniform system .1. interfacial free energy. *Journal of Chemical Physics*, 28(2):258–267, 1958.
- [28] B. I. Halperin, P. C. Hohenber, and S. Ma. Renormalization-group methods for critical dynamics .1. recursion relations and effects of energy conservation. *Physical Review B*, 10(1):139–153, 1974.
- [29] J. S. Langer. *Directions in Condensed Matter*. World Scientific, Singapore, 1986.
- [30] J. B. Collins and H. Levine. Diffuse interface model of diffusion-limited crystal growth. *Physical Review B*, 31(9):6119–6122, 1985.
- [31] O. Penrose and P. C. Fife. Thermodynamically consistent models of phase-field type for the kinetics of phase-transitions. *Physica D*, 43(1):44–62, 1990.

- [32] S. L. Wang, R. F. Sekerka, A. A. Wheeler, B. T. Murray, S. R. Coriell, R. J. Braun, and G. B. McFadden. Thermodynamically-consistent phase-field models for solidification. *Physica D*, 69(1-2):189–200, 1993.
- [33] A. A. Wheeler, W. J. Boettinger, and G. B. McFadden. Phase-field model of solute trapping during solidification. *Physical Review E*, 47(3):1893–1909, 1993.
- [34] G. Caginalp and W. Xie. Phase-field and sharp-interface alloy models. *Physical Review E*, 48(3):1897–1909, 1993.
- [35] J. A. Warren and W. J. Boettinger. Prediction of dendritic growth and microsegregation patterns in a binary alloy using the phase-field method. *Acta Metallurgica et Materialia*, 43(2):689–703, 1995.
- [36] A. Karma. Phase-field model of eutectic growth. *Physical Review E*, 49(3):2245–2250, 1994.
- [37] K. R. Elder, F. Drolet, J. M. Kosterlitz, and M. Grant. Stochastic eutectic growth. *Physical Review Letters*, 72(5):677–680, 1994.
- [38] A. A. Wheeler, G. B. McFadden, and W. J. Boettinger. Phase-field model for solidification of a eutectic alloy. *Proceedings of the Royal Society of London Series A-Mathematical Physical and Engineering Sciences*, 452(1946):495–525, 1996.
- [39] A. Karma and W.-J. Rappel. Quantitative phase-field modeling of dendritic growth in two and three dimensions. *Physical Review E*, 57(4):4323–4349, 1998.
- [40] G. B. McFadden, A. A. Wheeler, R. J. Braun, S. R. Coriell, and R. F. Sekerka. Phase-field models for anisotropic interfaces. *Physical Review E*, 48(3):2016–2024, 1993.
- [41] M. Plapp and A. Karma. Multiscale random-walk algorithm for simulating interfacial pattern formation. *Physical Review Letters*, 84(8):1740–1743, 2000.
- [42] A. Karma, Y. H. Lee, and M. Plapp. Three-dimensional dendrite-tip morphology at low undercooling. *Physical Review E*, 61(4):3996–4006, 2000.
- [43] J. Bragard, A. Karma, Y. H. Lee, and M. Plapp. Linking phase-field and atomistic simulations to model dendritic solidification in highly undercooled melts. *Interface Science*, 10(2-3):121–136, 2002.
- [44] L. Q. Chen. A novel computer-simulation technique for modeling grain-growth. *Scripta Metallurgica et Materialia*, 32(1):115–120, 1995.
- [45] I. Steinbach, F. Pezzolla, B. Nestler, M. Seesselberg, R. Prieler, G. J. Schmitz, and J. L. L. Rezende. A phase field concept for multiphase systems. *Physica D*, 94(3):135–147, 1996.
- [46] B. Nestler and A. A. Wheeler. Phase-field modeling of multi-phase solidification. *Computer Physics Communications*, 147(1-2):230–233, 2002.

- [47] B. Nestler, H. Garcke, and B. Stinner. Multicomponent alloy solidification: Phase-field modeling and simulations. *Physical Review E*, 71(4):041609, 2005.
- [48] J. Eiken, B. Bottger, and I. Steinbach. Multiphase-field approach for multicomponent alloys with extrapolation scheme for numerical application. *Physical Review E*, 73(6):066122, 2006.
- [49] N. Moelans. *Phase-field simulations of grain growth in materials containing second-phase particles*. PhD thesis, Katholieke Universiteit Leuven, 2006.
- [50] J. A. Warren, R. Kobayashi, A. E. Lobkovsky, and W. C. Carter. Extending phase field models of solidification to polycrystalline materials. *Acta Materialia*, 51(20):6035–6058, 2003.
- [51] R. Kobayashi, J. A. Warren, and W. C. Carter. Vector-valued phase field model for crystallization and grain boundary formation. *Physica D*, 119(3-4):415–423, 1998.
- [52] R. Kobayashi, J. A. Warren, and W. C. Carter. A continuum model of grain boundaries. *Physica D*, 140(1-2):141–150, 2000.
- [53] A. E. Lobkovsky and J. A. Warren. Sharp interface limit of a phase-field model of crystal grains. *Physical Review E*, 63(5):051605, 2001.
- [54] L. Granasy, T. Pusztai, and J. A. Warren. Modelling polycrystalline solidification using phase field theory. *Journal of Physics-Condensed Matter*, 16(41):R1205–R1235, 2004.
- [55] L. Granasy, T. Pusztai, G. Tegze, J. A. Warren, and Douglas J. F. Growth and form of spherulites. *Physical Review E*, 72(1):011605, 2005.
- [56] T. Pusztai, G. Bortel, and L. Granasy. Phase field modeling of polycrystalline freezing. *Materials Science And Enineering*, A(413):412–417, 2005.
- [57] R. Kobayashi and J. A. Warren. Modeling the formation and dynamics of polycrystals in 3D. *Physica A-Statistical Mechanics and Its Applications*, 356(1):127–132, 2005.
- [58] T. Pusztai, G. Bortel, and L. Granasy. Phase field theory of polycrystalline solidification in three dimensions. *Europhysics Letters*, 71(1):131–137, 2005.
- [59] T. Pusztai. unpublished.
- [60] J. Bechhoefer, A. J. Simon, A. Libchaber, and P. Oswald. Destabilization of a flat nematic-isotrop interface. *Physical Review A*, 40(4):2042–2056, 1989.
- [61] J. Bechhoefer and S. A. Langer. Stabilizing effect of elasticity is not enough to resolve discrepancies in observations concerning a moving nematic-isotropic interface. *Physical Review E*, 51(3):2356–2362, 1995.

- [62] O. A. Gomes, R. C. Falcao, and O. N. Mesquita. Anomalous capillary length in cellular nematic-isotropic interfaces. *Physical Review Letters*, 86(12):2577–2580, 2001.
- [63] W. Losert, D. A. Stillman, H. Z. Cummins, P. Kopczynski, W. J. Rappel, and A. Karma. Selection of doublet cellular patterns in directional solidification through spatially periodic perturbations. *Physical Review E*, 58(6):7492–7506, 1998.
- [64] M. Plapp and M. Dejmek. Stability of hexagonal solidification patterns. *Europhysics Letters*, 65(2):276–282, 2004.
- [65] P. G. de Gennes and J. Prost. *The Physics of Liquid Crystals*. Clarendon Press Oxford, 1993.
- [66] M. Reichenstein. *Dynamik von Disklinationen in anisotropen Fluiden*. PhD thesis, Universität Stuttgart, 2002.
- [67] F. C. Frank. On the theory of liquid crystals. *Discussions of the Faraday Society*, 25:19–28, 1958.
- [68] V. Popa-Nita and P. Oswald. Waves at the nematic-isotropic interface: The role of surface tension anisotropy, curvature elasticity, and backflow effects. *Physical Review E*, 68(6):061707, 2003.
- [69] K. Kassner. *Pattern Formation in Diffusion-Limited Crystal Growth*. World Scientific Publishing Co. Pte. Ltd., Singapore, 1996.
- [70] W. H. Press, S. A. Teukolsky, W. T. Vetterling, and B. P. Flannery. *Numerical Recipes in C: The Art of Scientific Computing*. Cambridge University Press, 1992.
- [71] J. M. A. Figueiredo, M. B. L. Santos, L. O. Ladeira, and O. N. Mesquita. Transient dynamics of a cellular front instability during directional solidification. *Physical Review Letters*, 71(26):4397–4400, 1993.
- [72] K. R. Elder, M. Katakowski, M. Haataja, and M. Grant. Modeling elasticity in crystal growth. *Physical Review Letters*, 88(24):245701, 2002.
- [73] K. R. Elder and M. Grant. Modeling elastic and plastic deformations in nonequilibrium processing using phase field crystals. *Physical Review E*, 70(5):051605, 2004.
- [74] J. Berry, M. Grant, and K. R. Elder. Diffusive atomistic dynamics of edge dislocations in two dimensions. *Physical Review E*, 73(3):031609, 2006.
- [75] P. Stefanovic, M. Haataja, and N. Provatas. Phase-field crystals with elastic interactions. *Physical Review Letters*, 96(22):225504, 2006.
- [76] K. R. Elder, N. Provatas, J. Berry, P. Stefanovic, and M. Grant. Phase-field crystal modeling and classical density functional theory of freezing. *Physical Review B*, 75(6):064107, 2007.
- [77] H. M. Singer and I. Singer. Analysis and visualization of multiply oriented lattice structures by a two-dimensional continuous wavelet transform. *Physical Review E*, 74(3):031103, 2006.

- [78] M. Rappaz, A. Jacot, and W. J. Boettinger. Last-stage solidification of alloys: Theoretical model of dendrite-arm and grain coalescence. *Metallurgical and Materials Transactions A-Physical Metallurgy and Materials Science*, 34(3):467–479, 2003.
- [79] A. Karma, D. A. Kessler, and H. Levine. Phase-field model of mode III dynamic fracture. *Physical Review Letters*, 87(4):045501, 2001.
- [80] M. Upmanyu, D. J. Srolovitz, A. E. Lobkovsky, J. A. Warren, and W. C. Carter. Simultaneous grain boundary migration and grain rotation. *Acta Materialia*, 54(7):1707–1719, 2006.
- [81] H. Fujita. Direct observation of subgrain-growth of cold-worked aluminium by means of electron microscopy. *Journal of the Physical Society of Japan*, 16(3):397–406, 1961.
- [82] H. Hu. Direct observations on annealing of a si-fe crystal in electron microscope. *Transactions of the Metallurgical Society of Aime*, 224(1):75, 1962.
- [83] G. Herrmann, H. Gleiter, and G. Baro. Investigation of low-energy grain-boundaries in metals by a sintering technique. *Acta Metallurgica*, 24(4):353–359, 1976.
- [84] U. Erb and H. Gleiter. Effect of temperature on the energy and structure of grain-boundaries. *Scripta Metallurgica*, 13(1):61–64, 1979.
- [85] S. W. Chan and R. W. Balluffi. Study of energy vs misorientation for grain-boundaries in gold by crystallite rotation method .1. [001] twist boundaries. *Acta Metallurgica*, 33(6):1113–1119, 1985.
- [86] S. W. Chan and R. W. Balluffi. Study of energy vs misorientation for grain-boundaries in gold by crystallite rotation method .2. tilt boundaries and mixed boundaries. *Acta Metallurgica*, 34(11):2191–2199, 1986.
- [87] R. W. Balluffi and R. Maurer. On rotating sphere-on-a-plate experiments and the question of whether high angle grain-boundaries melt below bulk melting temperatures. *Scripta Metallurgica*, 22(5):709–713, 1988.
- [88] N. Goldenfeld, B. P. Athreya, and J. A. Dantzig. Renormalization group approach to multiscale simulation of polycrystalline materials using the phase field crystal model. *Physical Review E*, 72(2):020601, 2005.
- [89] B. P. Athreya, N. Goldenfeld, and J. A. Dantzig. Renormalization-group theory for the phase-field crystal equation. *Physical Review E*, 74(1):011601, 2006.
- [90] E. Kröner. *Kontinuumstheorie der Versetzungen und Eigenspannungen*. Springer, Heidelberg, 1958.
- [91] Kröner. *Physics of Defects, Chapter 3: Continuum Theory of Defects*. North-Holland Publishing Company Amsterdam, New York, Oxford, 1980.

- [92] D. Rodney, Y. Le Bouar, and A. Finel. Phase field methods and dislocations. *Acta Materialia*, 51(1):17–30, 2003.
- [93] S. Y. Hu and L. Q. Chen. Solute segregation and coherent nucleation and growth near a dislocation phase-field model integrating defect and phase microstructures. *Acta Materialia*, 49(3):463–472, 2001.
- [94] Y. U. Wang, Y. M. Jin, A. M. Cuitino, and A. G. Khachaturyan. Phase field microelasticity theory and modeling of multiple dislocation dynamics. *Applied Physics Letters*, 78(16):2324–2326, 2001.
- [95] Y. U. Wang, Y. M. Jin, A. M. Cuitino, and A. G. Khachaturyan. Nanoscale phase field microelasticity theory of dislocations: Model and 3d simulations. *Acta Materialia*, 49(10):1847–1857, 2001.
- [96] Y. U. Wang, Y. M. Jin, A. M. Cuitino, and A. G. Khachaturyan. Application of phase field microelasticity theory of phase transformations to dislocation dynamics: model and three-dimensional simulations in a single crystal. *Philosophical Magazine Letters*, 81(6):385–393, 2001.
- [97] Y. M. Jin and A. G. Khachaturyan. Phase field microelasticity theory of dislocation dynamics in a polycrystal: model and three-dimensional simulations. *Philosophical Magazine Letters*, 81(9):607–616, 2001.
- [98] F. Leonard and R. C. Desai. Spinodal decomposition and dislocation lines in thin films and bulk materials. *Physical Review B*, 58(13):8277–8288, 1998.
- [99] M. Haataja and F. Leonard. Influence of mobile dislocations on phase separation in binary alloys. *Physical Review B*, 69(8):081201, 2004.
- [100] M. Haataja, J. Muller, A. D. Rutenberg, and M. Grant. Dislocations and morphological instabilities: Continuum modeling of misfitting heteroepitaxial films. *Physical Review B*, 65(16):165414, 2002.
- [101] M. Haataja, J. Muller, A. D. Rutenberg, and M. Grant. Dynamics of dislocations and surface instabilities in misfitting heteroepitaxial films. *Physical Review B*, 65(3):035401, 2002.
- [102] S. Limkumnerd and J. P. Sethna. Mesoscale theory of grains and cells: Crystal plasticity and coarsening. *Physical Review Letters*, 96(9):095503, 2006.
- [103] S. Y. Hu and L. Q. Chen. A phase-field model for evolving microstructures with strong elastic inhomogeneity. *Acta Materialia*, 49(11):1879–1890, 2001.
- [104] H. Nishimori and A. Onuki. Pattern-formation in phase-separating alloys with cubic symmetry. *Physical Review B*, 42(1):980–983, 1990.
- [105] A. Onuki. Ginzburg-landau approach to elastic effects in the phase-separation of solids. *Journal of the Physical Society of Japan*, 58(9):3065–3068, 1989.

- [106] L. O. Eastgate, J. P. Sethna, M. Rauscher, T. Cretegny, C.-S. Chen, and C. R. Myers. Fracture in mode I using a conserved phase-field model. *Physical Review E*, 65(3):036117, 2002.
- [107] I. S. Aranson, V. A. Kalatsky, and V. M. Vinokur. Continuum field description of crack propagation. *Physical Review Letters*, 85(1):118–121, 2000.